# SEARCHING FOR DARK MATTER WITH DEAP-3600

by

Alistair Butcher

Department of Physics

Royal Holloway, University of London


A thesis submitted to the University of London for the degree of

Doctor of Philosophy

September 2015

# Declaration

I confirm that the work presented in this thesis is my own. Where information has been derived from other sources, I confirm that this has been indicated in the document.

Signed:

Date:

# Abstract

The DEAP-3600 detector is a single phase direct detection search for particle dark matter. It comprises 3600 kgs of liquid argon, with a 1000 kg fiducialised target volume, surrounded by 255 photomultiplier tubes (PMTs). The detector components are described along with the dark matter interaction mechanism. A method for identifying and removing after-pulses in the PMT waveforms is described and its impact on discrimination variables is investigated. It is shown that the detector energy threshold can be lowered from 120 photoelectrons to 94 photoelectrons while keeping the $^{39}$Ar, the detector's most prominent background, leakage rate below 0.2 events in three years of running. A preliminary analysis of the after-pulsing PDF and rate from in situ calibration data is presented. Finally, the latest projected dark matter sensitivity is derived with a cross-section of $5.6 \times 10^{-47}\,\mathrm{cm}^2$ at a WIMP mass of $100\,\mathrm{GeV/cm}^2$. This sensitivity is derived in relation to the most prominent background, it assumes there is no increase in background rate due to the change in energy threshold. Finally, a likelihood approach to setting a WIMP-nucleus cross section limit, including known backgrounds, is outlined.

*For my parents Linda and John, and my partner Helena.*

# Acknowledgements

First I would like to thank Malcolm Fairbairn, my MSci project supervisor, for giving me the skills necessary to do research and for fuelling my love of physics and my interest in its dark side. Also for the eventful train journey with Jocelyn.

I would also like to thank Richard Eggleston for helping me through those first months, and for being the other founding PhD student of the Dark Matter group. Thank you for your encouragement and willingness to help at the drop of a hat, and all those lifts to Egham station.

I next have to thank Joseph Walding. Joe you have been both a great mentor and a great friend throughout my time here. Sorry about the snoring.

My thanks to James Nikkel, for always having your door open, for your pragmatic advice, and for your invention of drinks.

I would like to thank all my friends at Royal Holloway and the Dark Matter group in particular. My thanks go to Gabriela and James for your warmth, your dinner parties, and an amazing trip to Romania. To Emily for being a friend in Canada and shoulder to cry on. To Navin for his humour and companionship in Canada.

To all my friends in Canada and at SNOLAB, you all make trips over there a joyous experience. In particular thank you to Marcin for all your help, and to Ben. Sorry for the incident outside of the bar. Thank you to Corina for showing me the way of SNOLAB, and the way of Sudbury. DEAP-3600 is not the same without you.

A special thank you goes out to Kim Palladino for taking me in during my time in Canada. Your relentless optimism and astounding ability as a physicist is to be admired. Your tolerance of messy and disorganised flat mates is also to be admired.

My thanks also go to Tom Caldwell, your ability to elucidate the technicalities of all aspects of dark matter detection has helped me inestimably.

I would also like to thank Alison Mainwood, my undergraduate tutor, without you I would not be where I am today. I should also thank Simon Peacock for giving me a push in the right direction.

Thanks go to my brother, Matthew, and Leo for your love and support.

Thank you to Helena, for your absolute faith in me, for your love and support of all my endeavours, you are always there for me. Truly, I could not have done this without you.

Thank you to my parents, words cannot express my gratitude for everything you have done for me. I love you both very much.

Finally, thank you to Jocelyn Monroe, my supervisor. Thank you for your support and your determination to get the best from me. I have learnt an incredible amount from you and for this I am eternally grateful.

# Contents

# List of Figures

# List of Tables

# Chapter 1

# Introduction

*No one knows the reason for all this,*
*but it is probably quantum.*

Terry Pratchett

The concept of dark matter, an unseen form of mass in the universe, was first introduced to explain anomalies in the gravitational dynamics of galaxies and clusters of galaxies. Today it has been found to make up 25.8 % of the matter-energy content of the universe with baryonic matter making up only 4.8 %, the rest being attributed to dark energy [1]. Discovery of the characteristics of dark matter, its source, its particulate or non-particulate nature, its interaction mechanisms with ordinary matter, will be one of the crowning achievements of this scientific epoch. This thesis concerns one such effort to elucidate the nature of dark matter; direct detection with the DEAP-3600 experiment.

In chapter 1, a summary of our current understanding of dark matter is presented along with an overview of experimental efforts in detection. Chapter 2 describes direct detection of dark matter using liquid noble gases with an emphasis on argon. The design of the DEAP-3600 experiment, which makes use of liquid argon as a target medium, is then described. The DEAP-3600 experiment is an international collaboration with institutions

from the United Kingdom, Canada, and Mexico. It is currently being commissioned at SNOLAB. Finally, in chapter 2 the primary backgrounds to the dark matter search are outlined. Work modelling the background rates and distributions from all sources is on going. In chapter 3, simulation of the detector is discussed along with event reconstruction algorithms developed using Monte-Carlo. The simulation software was developed in collaboration with Canadian institutions: Queen's University, the University of Alberta, Carleton University and TRIUMF. The author implemented the optical calibration systems into the software as well as simulations of the DEAP-3600 electronics chain. The author also contributed to the simulation of the photomultiplier tube response. In the reconstruction section of chapter 3 the single photoelectron counting algorithm and pulse shape discrimination variables were originally developed for the MiniCLEAN experiment. The author ported these over to DEAP-3600 and developed a method to identify and remove after-pulses in the photomultiplier tube waveforms. The position reconstruction algorithms are currently being developed at Queen's University and Royal Holloway, University of London. Chapter 4 concerns calibration systems built for DEAP-3600 along with preliminary analyses of commissioning data. The external radioactive sources were developed at the Rutherford Appleton Lab and Royal Holloway. The optical calibration sources were delivered by Sussex University, the author performed preliminary analyses on these and the timing electronics. Finally in chapter 5 a new projected mass-cross-section sensitivity is derived in reference to the main $^{39}$Ar background.

## 1.1 Observational Evidence for Dark Matter

Fritz Zwicky, in 1933, first postulated the existence of something like dark matter when he noticed abnormal motions of the members of the Coma cluster, compared to those predicted using the known, luminous, mass at the time [2]. Unexpected galactic rotation curves measured by Louise Volders in the fifties [3] and further by Vera Rubin and collaborators in the late sixties provided evidence for missing mass on the galactic scale [4, 5].

As an illustration, the evidence for galactic dark matter is as follows. The Newtonian circular orbital velocity, $v$, of a body at a distance $r$ outside of a region with enclosed mass $M$ is given by

$$v = \sqrt{\frac{GM}{r}}, \tag{1.1}$$

where $G$ is the gravitational constant. Therefore, the velocities of stars in a galaxy in a region outside of the bulk of its mass should fall off as $\frac{1}{\sqrt{r}}$. However, observations of spiral galaxies, such as that shown in Figure 1.1, paint a very different picture, with luminous matter maintaining an approximately constant velocity out to high radii. As shown in the figure, this difference between theory and observation can be attributed to a large non-luminous halo of mass, or dark matter.

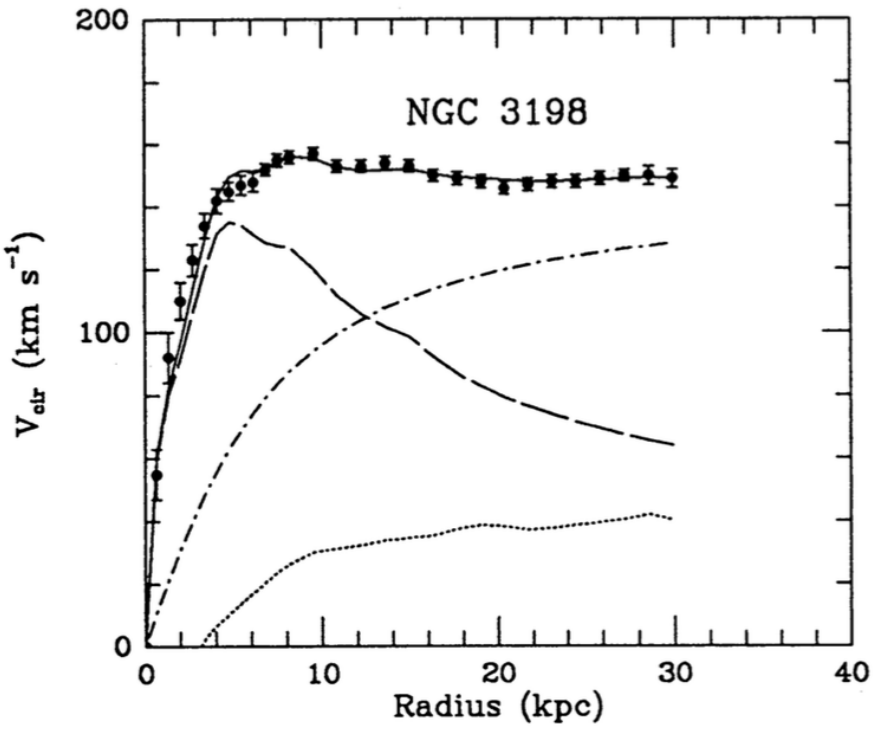


**Figure 1.1:** Rotation curve for galaxy NGC 3198 with a three component fit: the dashed curve is the visible component, the dotted curve is the gaseous component, and the dot-dash curve is the dark matter halo contribution. From [6].

The bullet cluster, shown in Figure 1.2, offers more evidence of non-luminous mass on a galactic cluster scale. It is comprised of two clusters of galaxies which have previously collided with each other. Imaging of the cluster by the Chandra X-ray Observatory re-

vealed the location of hot gas, displayed in pink, which makes up most of the baryonic mass of the cluster [7]. The hot gas was slowed down by interactions (producing X-rays) during the collision between the two clusters, leaving it in the central region. Further observations by the Hubble telescope revealed, using gravitational lensing, the location of the majority of the mass. This, displayed in blue, was found to be outside of the hot gas region. This shows the majority of the mass of each cluster, now attributed to dark matter, passed through unencumbered during the collision. The lack of evidence for dark matter slowing down is used to set an upper limit on dark matter's self-interaction cross section per dark matter mass, which has been found to be approximately $1.25\,\mathrm{cm}^2\mathrm{g}^{-1}$ (68% confidence limit) [8]. Measurements of other collisions have further constrained this number to $0.47\,\mathrm{cm}^2\mathrm{g}^{-1}$ (95% confidence limit) [8].

**Figure 1.2:** Image of the bullet cluster collision. Baryonic hot gas observed by the Chandra X-ray Observatory is in pink while the mass distribution inferred from gravitational lensing by the Hubble Space telescope is in blue. The hot gas was slowed down during the collision while the majority of the mass from each cluster, attributed to dark matter, passed through unencumbered. Credit: X-ray: NASA/CXC/CfA/M.Markevitch et al.; Optical: NASA/STScI; Magellan/U.Arizona/D.Clowe et al.; Lensing Map: NASA/STScI; ESO WFI; Magellan/U.Arizona/D.Clowe et al.

Observations of the cosmic microwave background (CMB) provide compelling evidence for dark matter on cosmological scales. From the cosmological principle the distribution of matter in the universe is expected to be homogeneous and isotropic for scales greater than

$\sim 50\,\mathrm{Mpc}$. This is reflected in the CMB where the temperature of photons from the last scattering surface is uniform to one part in $10^5$. However, it is the small scale anisotropies which reveal information about the matter-energy content of the universe. Fluctuations in the gravitational potential at the time of photon decoupling are reflected in fluctuations of the photon temperature. Figure 1.3 shows a map of the temperature fluctuations of the CMB measured by Planck [9]. The dipole term and the galactic plane have been subtracted leaving $\mu$K scale differences in temperature across the sky. A spherical harmonic expansion of the these temperature fluctuations provides a way of characterising the amount of anisotropy per angular scale in terms of multipole moments. Figure 1.4 shows the power spectrum of the temperature fluctuations derived from the spherical harmonic coefficients. Here larger multipole moments, $l$, correspond to smaller angular scales. Information about the age, geometry, and matter content of the universe is determined from the positions and amplitudes of the acoustic peaks past $l = 30$ [10]. The power spectrum is plotted with what is expected from the standard model of cosmology, the $\Lambda$CDM model; a spatially flat universe which includes cold dark matter and dark energy. The Planck result places the baryonic matter contribution at $\Omega_\mathrm{b}h^2 = 0.02226 \pm 0.00023$ and the dark matter contribution at $\Omega_c h^2 = 0.1186 \pm 0.002$. Here $\Omega$ is the density parameter defined as $\Omega_\mathrm{x} = \rho_\mathrm{x}/\rho_\mathrm{c}$; the mass density, $\rho_\mathrm{x}$, compared the critical density, $\rho_\mathrm{c}$, required for a spatially flat universe. $h^2$ is the reduced Hubble constant defined as $h \equiv H_0/(100\,\mathrm{kms}^{-1}\mathrm{Mpc}^{-1})$ [11].

Big Bang nucleosynthesis (BBN) offers another constraint on the value of $\Omega_\mathrm{b}$. Shortly after the Big Bang the temperature of the universe was too high for heavy atomic nuclei to exist. As the universe subsequently expanded and cooled the temperature dropped sufficiently below nuclear binding energies such that the lighter elements could form. Once the reaction rate dropped below the expansion rate of the universe light element formation ceased and a "freeze-out" of the elemental abundances occurred. Elemental abundances depend on the ratio of baryons to photons [12]. Estimates of these abundances, thus, determine the allowed range of the baryon to photon ratio which in turn predicts the value of $\Omega_\mathrm{b}$. Figure 1.5 shows predictions of the primordial abundances of $^4$He (top) and deuterium (bottom)

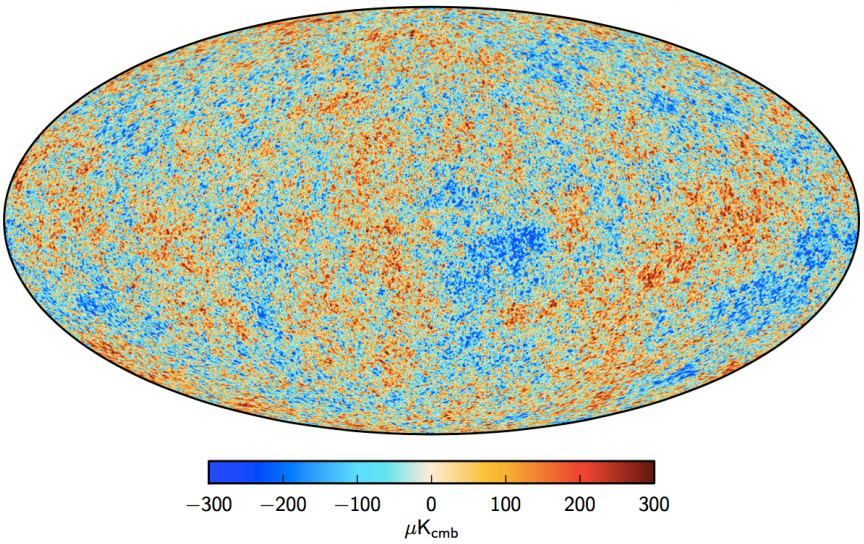


**Figure 1.3:** Map of the temperature fluctuations of the CMB measured by Planck. The dipole term and the galactic plane have been subtracted. From [1].

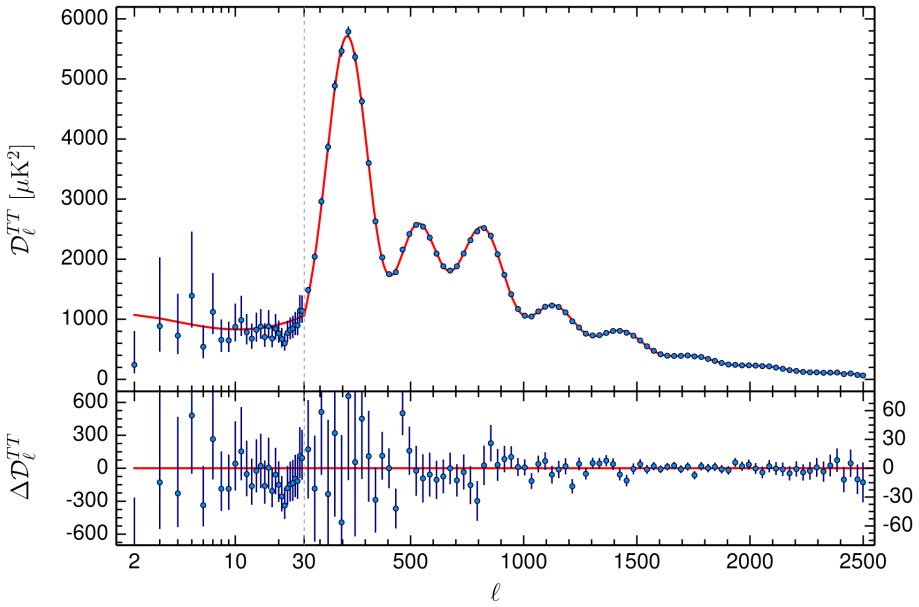


**Figure 1.4:** The CMB power spectrum as measured by Planck plotted with the best-fit ΛCDM model. From [1].

as a function of $\Omega_\mathrm{b}h^2$. These abundances are consistent with the CMB measurement of $\Omega_\mathrm{b}h^2$ using the Planck 2015 data set.

The evidence presented above points to a non-baryonic type of matter pervading the universe. An alternative explanation may be that our current theory of gravity is incorrect, and needs to be modified to fit with observation. Modified Newtonian Dynamics (MOND)

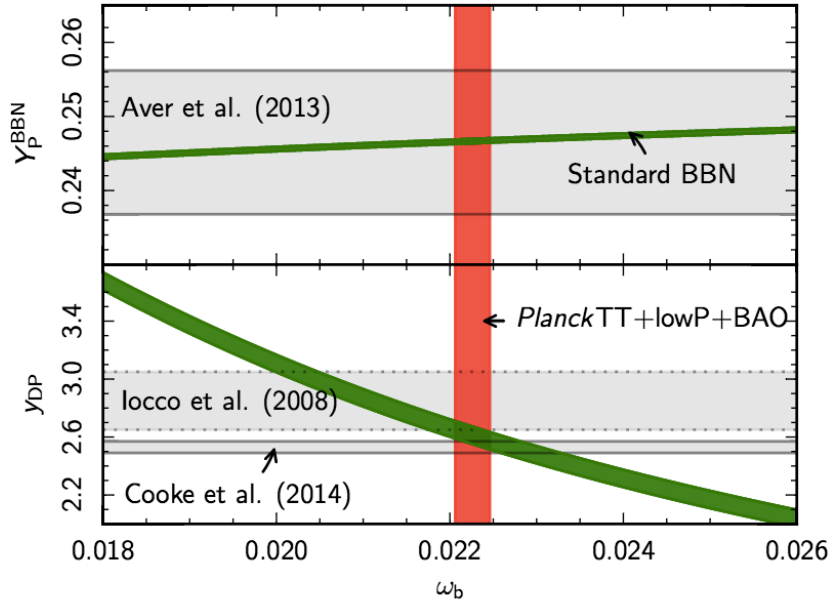


**Figure 1.5:** Predictions for the primordial abundances of $^4$He (top) and deuterium (bottom) from standard BBN, as a function of baryon density $\omega_b \equiv \Omega_b h^2$. The vertical red line represents the Planck (2015) TT+lowP+BAO bounds on $\omega_b$ with 68% errors. The green lines represent nuclear reaction rates and the lifetime of the neutron with the width corresponding to 68% uncertainty. The horizontal bands represent observational bounds on the primordial element abundances also with 68% errors. From [13].

is the most well known form of this type of explanation, first developed by Milgrom in 1983 [14]. MOND models propose that Newtonian dynamics breaks down at small accelerations. Simple MOND models, while successfully accounting for many galactic rotation curves [6], fail to reconcile with observations of galaxy clusters and cosmological evidence without considerable adjustments [15][16].

## 1.2 Dark Matter Candidates

Assuming non-baryonic dark matter is a particle, observations place many constraints on its characteristics. Evidently it must be "dark", in the sense that it does not interact with photons via electromagnetism. It must interact gravitationally and be stable or long lived on cosmological time scales. A dark matter candidate must also be non-relativistic at the time of structure formation in the universe to become trapped in galactic gravitational potentials. To explain observations such as the Bullet cluster, it should also be virtually

collisionless. Two prominent candidates which match these criteria are discussed below: axions, and WIMPs.

### 1.2.1 Axions

Axions were originally postulated to solve the "strong CP problem" of quantum chromodynamics (QCD). In QCD the gauge invariant vacuum state is a super position of Non-Abelian vacuum gauge potentials, labelled $n$, given by

$$|\theta\rangle = \sum_n e^{-in\theta} |n\rangle \,. \tag{1.2}$$

Here, the angle $\theta$, describing the vacuum state, appears in the invariant and observable quantity

$$\bar{\theta} \equiv \theta - \arg(m_1 m_2 \dots m_N), \tag{1.3}$$

where $m_N$ are the quark masses [17]. The angle $\theta$ violates P and CP symmetries. However, CP violation has not been observed in QCD. Hence, the "strong CP problem". The electric dipole moment of the neutron $d_\mathrm{n}$ is one prediction of QCD where

$$|d_\mathrm{n}| \sim 10^{-16} \bar{\theta}\, e\,\mathrm{cm}, \tag{1.4}$$

with $e$ being the electric charge [18]. A recent experimental limit is

$$|d_\mathrm{n}| < 2.9 \times 10^{-26} e\,\mathrm{cm}, \tag{1.5}$$

which gives $\bar{\theta} < 10^{-9}$ [19]. The strong CP problem is the fact that this value is so small when, because of CP violation, the natural value is of order one. One solution to the problem changes $\bar{\theta}$ from a parameter in the theory to a dynamical variable which can relax to a potential minimum; the Peccei-Quinn (PQ) solution [20]. This solution introduces a new particle, the axion, which is a Nambu-Goldstone boson of the $U(1)_\mathrm{PQ}$ symmetry of the PQ mechanism. These particles have been proposed as a candidate for dark matter,

since they couple to standard model particles weakly, are effectively stable, and potentially have a large cold component [21][22].

Most searches look for the axion via its coupling to photons, an example of which is the Axion Dark Matter eXperiment (ADMX). ADMX consists of a high-Q microwave cavity in which axions can turn into photons via resonant conversion. Figure 1.6 shows the current and projected sensitivity of the ADMX experiment. It will be able to exclude some of the axion cold dark matter region over the next several years [23].

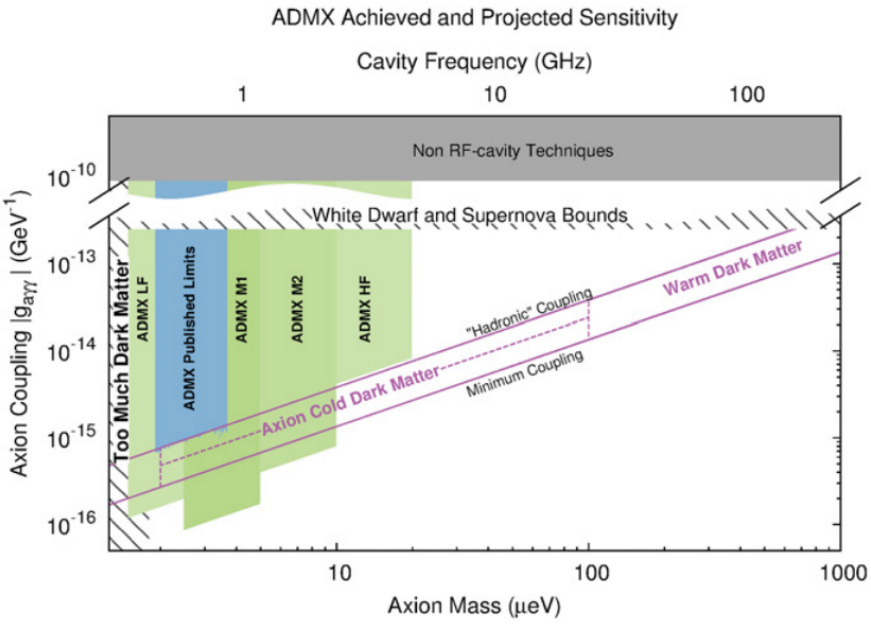


**Figure 1.6:** Current and projected sensitivity of the ADMX experiment. Some of the axion cold dark matter region will be excluded by the experiment. From [23].

### 1.2.2 WIMPS

The category of Weakly Interacting Massive Particles, WIMPs, covers a range of particles which exhibit a thermal relic abundance. The WIMP model is attractive as thermal production mechanisms in the early universe can be shown to produce the correct dark matter abundance today, provided the interaction cross section is approximately at the weak scale and the WIMP mass is of order 100 GeV [24]. Standard model particle annihilation in the high temperature early universe produced WIMPs, and vice versa, placing WIMPs in

thermal equilibrium with the standard model particles. The co-moving number density, $n$, of WIMPs over time is governed by the Boltzmann rate equation

$$\frac{dn}{dt} = -3Hn - \langle\sigma_{\text{ann}}v\rangle(n^2 - n_{\text{eq}}^2), \tag{1.6}$$

where H is the Hubble constant, $n_{\text{eq}}$ is the thermal equilibrium number density, and $\langle\sigma_{\text{ann}}v\rangle$ is the thermally-averaged annihilation cross section. At early times, when the temperature of the universe, T, was high, dark matter particles were relativistic (i.e. when $T \gg m_\chi$, where $m_\chi$ is the WIMP mass). At this point the equilibrium number density $n_{\text{eq}} \propto T^3$ [25]. The WIMP production (and annihilation) rate is given by $\Gamma_{\text{ann}} = \langle\sigma_{\text{ann}}v\rangle n_{\text{eq}}$ [26].

As the universe expanded and cooled the dark matter particles became non-relativistic (when $T \lesssim m_\chi$) and the equilibrium number density $n_{\text{eq}} \simeq g(m_\chi T/2\pi)^{3/2}\exp(-m_\chi/T)$, where $g$ is the number of internal degrees of freedom. Production of WIMP particles thus became Boltzmann suppressed by a factor $e^{-m_\chi/T}$. The number density of the WIMP particles simultaneously decreased as the universe expanded reducing the annihilation rate. Once the annihilation rate dropped below the expansion rate of the universe, i.e., when $\Gamma_{\text{ann}} \lesssim H$, annihilation effectively ceased and the WIMP density remained approximately constant. This is known as freeze out. The relic density $\Omega_\chi h^2$ of a WIMP model thus depends on its proposed annihilation cross section. An energy independent approximation of the relic density is given in [25]:

$$\Omega_\chi h^2 \simeq \frac{3\times10^{-27}\,\text{cm}^3\text{s}^{-1}}{\langle\sigma_{\text{ann}}v\rangle}. \tag{1.7}$$

Here the relic density is inversely proportional to the WIMP annihilation cross section. A larger annihilation cross section means the WIMPs stay in thermal equilibrium longer, leaving us with a smaller relic abundance today. If the interaction is taken to be weak-scale the annihilation cross section can estimated to be $\langle\sigma_{\text{ann}}v\rangle \sim \alpha^2(100\,\text{GeV})^{-2} \sim 10^{-25}\,\text{cm}^3\text{s}^{-1}$. Putting this value in to Equation 1.7 returns a relic density at the same order of magnitude as that found from cosmological observations. This coincidence gives the WIMP model appeal as it suggests that if there is a new electroweak scale particle

it is, most likely, dark matter [25]. The full relic density calculation can be found in, for example, [27] or Section 7.2 of [26].

A favoured WIMP candidate comes from supersymmetry (SUSY), which predicts the existence of a stable "lightest supersymmetric particle" (LSP) in models which conserve R-parity. In many such models the LSP is the Neutralino, a linear combination of the SUSY partners of the photon (photino), $Z^0$ (zino), and Higgs boson (higgsino) [25]. R-parity symmetry, $P_{\mathrm{R}}$, is given by

$$P_{\mathrm{R}} \equiv (-1)^{3B+L+2S}, \tag{1.8}$$

where B is the baryon number, L is lepton number, and S is the spin. All SUSY particles have $P_{\mathrm{R}} = -1$ and all standard model particles have $P_{\mathrm{R}} = 1$. Under this symmetry all SUSY particles must be produced in pairs and must decay to an odd number of particles [28]. Thus, R-parity conservation ensures the LSP must be stable.

## 1.3 Dark Matter Direct Detection

Direct detection experiments look for signals of WIMP-nucleus scattering. Following [29], the differential scattering rate per unit recoil energy, mass, and time is given by

$$\frac{dR}{dE_{\mathrm{R}}} = \frac{R_0}{m_\chi r}\frac{\sqrt{\pi}}{k}\int_{v_{\mathrm{min}}}^{v_{\mathrm{esc}}}\frac{1}{v}f(\vec{v},\vec{v}_{\mathrm{E}})d^3v. \tag{1.9}$$

Here $f(\vec{v},\vec{v}_{\mathrm{E}})$ is the dark matter velocity distribution, at this point assumed to be a truncated Maxwellian distribution given by

$$f(\vec{v},\vec{v}_{\mathrm{E}}) = \exp\left[-\frac{(\vec{v}+\vec{v}_{\mathrm{E}})^2}{2v_0^2}\right]. \tag{1.10}$$

Here $\vec{v}$ is the velocity onto the target, and $\vec{v}_{\mathrm{E}}$ is the Earth's velocity relative to the dark matter distribution. $v_0 = \sqrt{3/2}v_{\mathrm{c}}$ is the speed dispersion which is related to the local

circular speed $v_c = 220 \pm 20\,\mathrm{km\,s^{-1}}$ [30]. $v_{\min} = \sqrt{\frac{2E_R}{m_\chi r}}$ is the minimum velocity which can cause a nuclear recoil of energy $E_R$, and $v_{esc} = 560\,\mathrm{km\,s^{-1}}$ is the local escape velocity of the galaxy [31]. $k$ acts as a normalisation factor such that

$$k = 4\pi \int_0^{v_{esc}} f(\vec{v}, \vec{v}_E) v^2 dv. \tag{1.11}$$

The Maxwellian velocity distribution corresponds to that of an isothermal sphere of dark matter surrounding the galaxy with a density profile $\rho(r) \propto r^{-2}$ [26].

The Earth's motion relative to the dark matter halo, $\vec{v}_E$, is made up of three components [29]:

$$\vec{v}_E = \vec{u}_r + \vec{u}_s + \vec{u}_E. \tag{1.12}$$

Here $\vec{u}_r = (0, v_c, 0)$ is the galactic rotation given by the local circular velocity, $\vec{u}_s = (10.0 \pm 0.4, 5.2 \pm 0.6, 7.2 \pm 0.4)$ [32] is the Sun's motion relative to nearby stars, and $\vec{u}_E$ is the motion of the Earth around the Sun. Parametrised models which calculate $\vec{u}_E$ given a certain date can be found in, for example, [29] and [33]. This relative motion to the dark matter halo means that the rate of potential WIMP signals has a time dependence; an annual modulation. A yearly, cyclical, change in detection rate can be one of the indicators of a positive dark matter signal, this is discussed further below.

$r = 4m_\chi m_T/(m_\chi + m_T)^2$ is the reduced mass kinematic factor with $m_T$ being the mass of the target nucleus. The factor $R_0$ is where the dark matter scattering cross section appears and is given by

$$R_0 = \frac{2}{\sqrt{\pi}} \frac{N_0}{A} \frac{\rho_\chi}{m_\chi} \sigma_0, \tag{1.13}$$

where $N_0$ is Avagadro's number, $A$ is the atomic mass of the target, $\rho_\chi = 0.3\,\mathrm{GeVcm^{-3}}$ is the local dark matter density, and $\sigma_0$ is the WIMP-nucleus cross section at zero momentum transfer. Through the use of Fermi's Golden Rule [34] the momentum dependence of the cross section is taken up by a separate nuclear form factor, $F^2(E_R)$, discussed below. This accounts for scattering off a non-point target particle with increasing momentum transfer $q$, given by $q = \sqrt{2m_T E_R}$.

The choice of $\rho_\chi = 0.3\,\mathrm{GeVcm}^{-3}$ is traditionally used in the calculation of exclusion limits [26]. However, this value has a large, order factor 2, variation in the literature depending on the calculation method [35][36]. Calculation methods involve either using measurements of dynamical tracers, such as the rotation curve, to constrain mass models of the Milky Way, making results model dependent, or using measurements of the motion of stars nearby the sun, which result in larger uncertainties due to small sample sizes [37]. For example, a recent study [38] found $\rho_\chi = 0.420^{+0.021}_{-0.018}\,\mathrm{GeVcm}^{-3}$ using a Navarro-Frenk-White (NFW) density profile [39] and $\rho_\chi = 0.420^{+0.019}_{-0.021}\,\mathrm{GeVcm}^{-3}$ using an Einasto profile [40]. Another study, [41], found $\rho_\chi = 0.3 \pm 0.1\,\mathrm{GeVcm}^{-3}$. The dark matter density directly affects the rate, appearing in the numerator of Equation 1.9, and therefore any calculation of the cross section limit, for example. The choice of $\rho_\chi = 0.3\,\mathrm{GeVcm}^{-3}$ in this text is to allow comparison with other direct detection experiments.

The basic rate is also modified by an interaction factor ($I$) which accounts for the fact that scattering is occurring on the whole nucleus. This factor has a net nuclear spin dependent and independent form. Since argon, the target in use in DEAP-3600, has negligible numbers of isotopes with net nuclear spin, the spin independent case will be discussed here. For more information on the spin dependent case see [34][29][26]. The spin independent interaction factor is given by

$$I = A^2 \frac{\mu_\mathrm{T}^2}{\mu_\mathrm{p}^2}, \tag{1.14}$$

where $\mu_\mathrm{T}$ is the WIMP-target reduced mass, $\mu_\mathrm{p}$ is the WIMP-proton reduced mass, and it is assumed for low momentum transfer there will be $A$ scattering amplitudes adding in phase, i.e. coherent scattering across the nucleus. It has also been assumed in this case that the coupling to protons and neutrons is the same [25].

Finally, a detector response function, $H(E_\mathrm{R}, E_\mathrm{du})$, is included. This accounts for the finite resolution of the detector, the counting efficiency given cuts, and converts the recoil spectrum into energy units measurable in the detector, $E_\mathrm{du}$, i.e. charge, photoelectrons etc. It can be built from Monte Carlo simulations of the detector in question, and may take

the form of a Gaussian resolution function combined with an $E_{\rm du}$ dependant efficiency. The full rate in terms of detector energy units is then

$$\frac{dR}{dE_{\rm du}} = \int dE_{\rm R} \frac{dR}{dE_{\rm R}} F^2(E_{\rm R}) I H(E_{\rm R}, E_{\rm du}). \tag{1.15}$$

In the Born approximation the spin independent form factor is the normalised Fourier transform of the ground state mass density of the target. The density is generally assumed to be a uniform sphere of radius $R_0 = \sqrt{R^2 - 5s^2}$, where $R = 1.2A^{1/3}\,\text{fm}$. This is convolved with a Gaussian to account for the soft nuclear edge with thickness $s \simeq 1\,\text{fm}$ [42]. The mass density $\rho(\vec{r})$ is then given by

$$\rho(\vec{r}) = \int \mathrm{d}^3\vec{r}\prime \rho_0(\vec{r}\prime)\rho_1(\vec{r} - \vec{r}\prime). \tag{1.16}$$

Here $\rho_0$ is constant inside the sphere of radius $R_0$, and $\rho_1(\vec{r}) = \exp[-\frac{1}{2}(r/s)^2]$. The Fourier transform is then

$$F(E_{\rm R}) = \frac{3j_1(qR_0)}{qR_0} \exp\left[-\frac{1}{2}(qs)^2\right], \tag{1.17}$$

where $j_1(qR)$ is a spherical Bessel function, and $q$ is the momentum transfer. Equation 1.17 is the Helm form factor [43] which closely matches Woods-Saxon Two-Parameter Fermi model. Since the mass distribution of the nucleus is difficult to measure the charge distribution is used instead, assuming the mass and charge densities are proportional [44]. Charge densities can then be determined via elastic electron or muon scattering. Examples of the functional form are shown in Figure 1.7 for Argon-40, Germanium-72, and Xenon-131 target nuclei.

The recoil rate, $\frac{dR}{dE_{\rm R}} F^2(E_{\rm R}) I$, in $\text{keV}^{-1}\text{kg}^{-1}\text{day}^{-1}$ for Argon-40, Germanium-72, and Xenon-131 is shown in Figure 1.8, for a zero momentum transfer cross section of $10^{-8}\,\text{pb}$ and a WIMP mass of 100 GeV. At higher energies loss of coherence reduces the overall rate, which is especially apparent for high mass targets. For all targets a low energy search region is the most preferable due to the near exponential fall off of the differential rate distribution. The lowest possible detection threshold energy is thus a motivation for

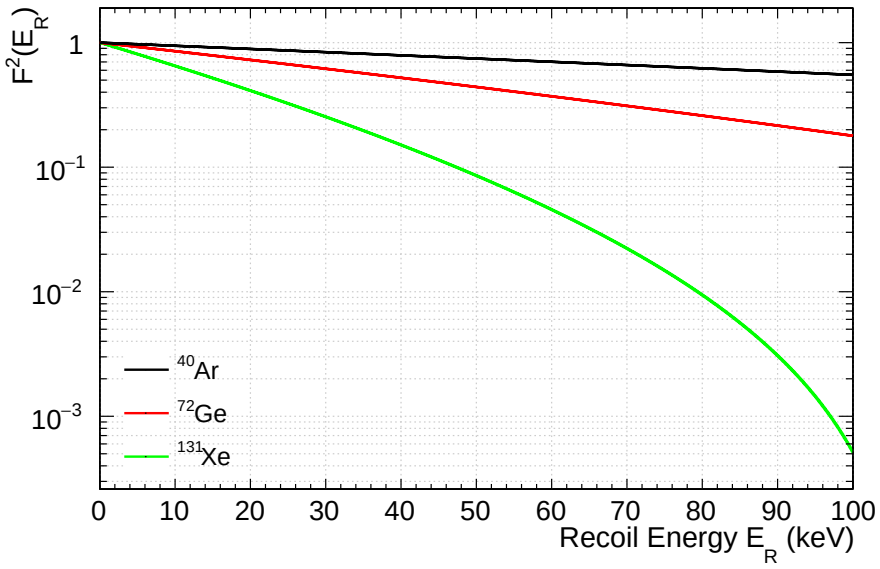


**Figure 1.7:** The energy dependent form factor for Argon-40, Germanium-72, and Xenon-131.

detector design. In the DEAP-3600 experiment, with an energy window of 60 to 120 keV and a fiducial mass of 1000 kg, 73 dark matter events per year are expected for a WIMP with a cross section of $10^{-8}$ pb and mass of 100 GeV.

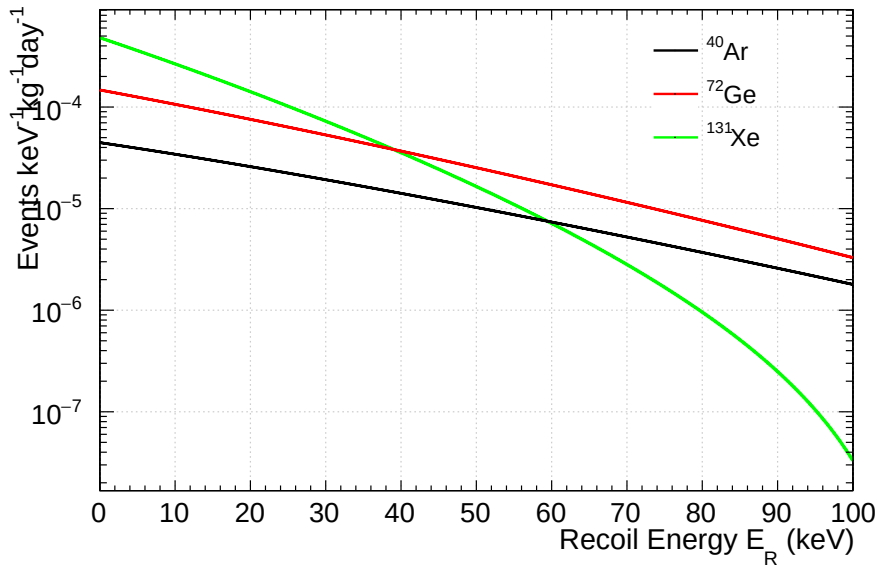


**Figure 1.8:** Differential recoil rate for Argon-40, Germanium-72, and Xenon-131 for a zero momentum transfer cross section of $10^{-8}$ pb and a WIMP mass of 100 GeV. In the DEAP-3600 experiment, with an energy window of 60 to 120 keV and a fiducial mass of 1000 kg, 73 dark matter events per year are expected for a WIMP with these parameters.

## 1.4 Direct Detection Experimental Overview

There are many experiments, using a multitude of approaches, trying to detect WIMP-nucleus recoil events. Figure 1.9 shows some of the current and future experimental efforts, showing the 90% confidence level mass versus cross section exclusion limits for each. Dark matter experiments typically use one or a combination of three detection methods: charge, light, or heat (phonons). The factors which drive dark matter sensitivity are threshold energy, exposure, and background discrimination. The three detection methods typically give a trade off between these three factors. A selection of these methods along with experiments which use them are described below. A detailed review of dark matter direct detection efforts can be found in [45].

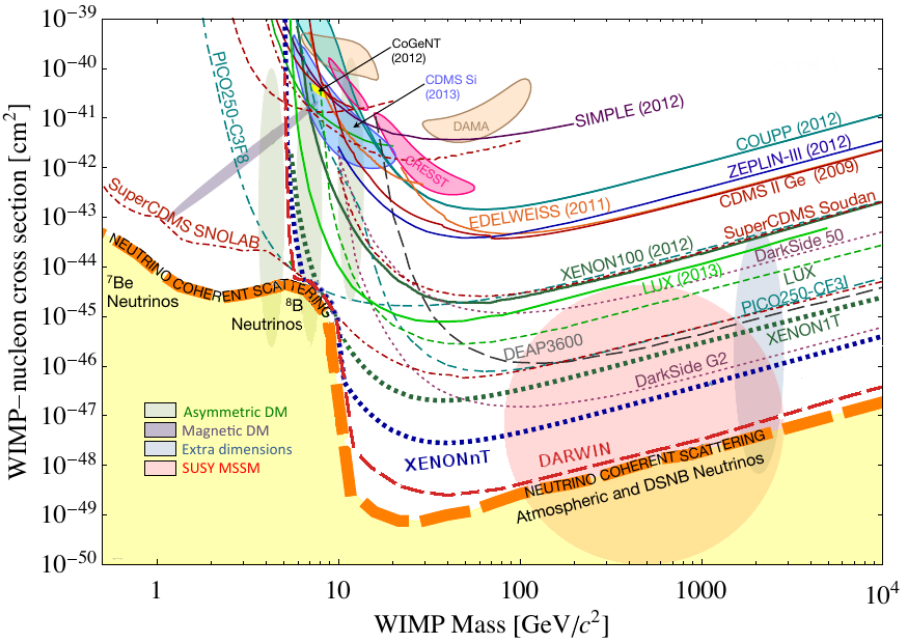


**Figure 1.9:** A selection of WIMP-nucleus scattering cross section limits from multiple direct detection experiments. The plot shows the full sensitivity of DEAP-3600 after 3000 kg.years of exposure. The experiment requires two months of data to surpass LUX's current sensitivity at a mass of 1TeV, and 8 months to surpass their full sensitivity. In contrast the next generation XENON detector, XENON1T, needs only 2 months of data to surpass LUX's full sensitivity and will ultimately gain the leading limit. From [46].

### 1.4.1 Room Temperature Scintillator Crystals

Incoming radiation causes excitation of the material in scintillator crystals. Subsequent de-excitation then gives off light which is measured by a photosensor. Scintillator crystals boast a low energy threshold and large light output, typically 8% of deposited energy [45]. These detectors rely solely on scintillation light and, as such, have no way to distinguish between particle types. They, instead, look for an annual modulation signal, described above, to identify dark matter.

DAMA [47] is one such experiment, based at Laboratori Nazionali del Gran Sasso (LNGS), it uses an array of NaI crystals as a detection medium. Combining data sets with its successor DAMA/LIBRA a 1.33 ton year exposure was reached over 14 years. In this time frame an annual modulation, varying between 2 and 6 $\mathrm{keV_{ee}}$, was observed with a dark matter signal significance of $9.3\,\sigma$. If this signal is assumed to be a spin independent WIMP-nucleus interaction two confidence regions appear, seen in Figure 1.9, between 10 - 15 $\mathrm{GeV/c^2}$ for scattering off sodium and 60 - 100 $\mathrm{GeV/c^2}$ for scattering off iodine [48]. As can be seen from Figure 1.9, these results are in tension with other experiments. Discussions of various possible resolutions can be found in [49].

### 1.4.2 Germanium Detectors

Germanium detectors used in ionisation mode cannot discriminate between particle types. They can, however, discriminate between events on the surface of the medium and those which occur in the centre by measuring the rise time of the charge readout of the ionisation signal. They generally have a very low threshold, $\sim 0.5\,\mathrm{keV_{ee}}$, such that they can detect light mass, order 1 GeV, WIMPs.

CoGeNT [50] is one such detector, based at Soudan Underground Laboratory. It has 1.5 kg.years of exposure data at a threshold of 500 eV. Like DAMA, CoGeNT also detected an annual modulation signal varying between 0.5 to 2 $\mathrm{keV_{ee}}$. This is 4 to 7 times larger than the expected WIMP signal but is in phase with such a signal at a 2 $\sigma$ significance.

If this is, indeed, interpreted as a WIMP signal it gives a cross section of $2.5 \times 10^{-41}\,\mathrm{cm}^2$ for a mass of 8 GeV (shown in Figure 1.9). CoGeNT's only discrimination is between so called surface and bulk events. Re-interpretation of the classification of the bulk events found no significance to the dark matter signal [51].

### 1.4.3 Cryogenic Bolometers

Cryogenic bolometers measure a phonon signal as a particle scatters off the target medium. Phonon interactions raise the temperature of the medium, and if scintillation or charge are simultaneously recorded discrimination between electronic and nuclear recoils can be achieved via measurement of the energy dependence of signal quenching. These detectors typically have very low thresholds and high energy resolution.

CRESST-II, based at LNGS exploits both scintillation and phonon collection. With an energy range between 10.2 $\mathrm{keV_r}$ and 19.0 $\mathrm{keV_r}$, and an exposure of 730 kg.days, they saw an excess of signal like events. This produced two potential WIMP confidence regions of $3.7 \times 10^{-41}\,\mathrm{cm}^2$ at 11.6 GeV (4.2 $\sigma$) and $1.6 \times 10^{-42}\,\mathrm{cm}^2$ at 25.3 GeV (4.7 $\sigma$) [52]. Studies suggest these events could be from ion sputtering caused by $^{206}$Pb recoils and alpha particles from $^{210}$Po decay when combined with realistic modelling of the surface roughness of detector clamps [53].

CDMS [54] and CDMS-II [55] based at Soudan Underground Laboratory are composed of 11 Si and 19 Ge detectors of 100g to 230g each. The experiments exploit both phonon and charge collection, allowing for discrimination against electronic recoils. A combined analysis of the CDMS-II data set gave a spin-independent upper limit of $3.8 \times 10^{-44}\,\mathrm{cm}^2$ at a WIMP mass of $70\,\mathrm{GeV/c^2}$ [55]. The silicon only data set had an exposure of 23.4 kg.days with an energy window of 7-100keVnr and saw excess corresponding to a possible WIMP signal. This gave a WIMP mass of 8.6 GeV and spin independent cross section of $1.9 \times 10^{-41}\mathrm{cm}^2$. However, no annual modulation was seen, putting it in tension with CoGeNT which also uses germanium. The successor to CDMS-II, SuperCDMS, uses 15 Ge crystals of 0.6 kg each. With an energy window between 1.6 and 10 keVnr and an

exposure of 577 kg.days they have achieved a limit of $1.2 \times 10^{-42}\,\mathrm{cm}^2$ at 8 GeV [56].

### 1.4.4 Superheated Fluids

Superheated fluid based detectors use mediums comprised of refrigerants operated at a super heated state just the below the boiling point of the liquid. Incoming particles cause bubble nucleation in the liquid. A phase transition is required for this effect to be seen so bubbles above a certain critical size have to form. This gives the advantage that only particles such as alphas, neutrons, or WIMPs can cause a signal. Once a bubble is produced the event is photographed with a CCD. This results in a position resolution of $\sim 1\,\mathrm{mm}$, allowing for fiducialisation of the central volume.

Once a bubble has formed the medium has to be reset, first by re-compression and then decompression to a value below the vapour pressure. This creates some dead time after an interaction. They are threshold devices, not giving a specific energy readout, just the minimum energy the interaction could be. The energy threshold is typically scanned during a run by varying temperature and pressure. Acoustic signals caused during nucleation can be used to discriminate against alphas. It was found that alpha particles produce a higher amplitude acoustic emission than nuclear recoils [57]. PICO currently shows the strongest limit of these types of detector with a spin dependent WIMP-proton cross section of $\sim 9 \times 10^{-40}\,\mathrm{cm}^2$ at 20 GeV [58].

### 1.4.5 Directional Detectors

Directional detectors measure the track of incoming dark matter particle. Given the Earth's velocity in the galactic reference frame WIMPs are expected to come from a preferred direction. This is the opposite direction to our tangential velocity as we orbit the galaxy, approximately in line with the constellation Cygnus.

The medium is in a gaseous phase so that nuclear recoil track lengths are long enough to be resolved. Current projects use time projection chambers (TPCs) with a typical gas

medium of $CS_2$, $CF_4$, or $^3$He. The last two have the advantage of containing unpaired nucleons, allowing for a measure of the spin dependent cross section. Typically ionisation caused by a recoil is drifted to a readout plane, the ionisation patten is then used to reconstruct the planar projection of track. A non uniform energy loss along the length of the track allows for head to tail reconstruction. The third directional component is read out in a detector specific fashion, more information can be found here [59]. A major advantage to directional detection can be understood by referring to Figure 1.9. Here the region labelled neutrino coherent scattering, also called the solar neutrino floor, marks the exposure when solar neutrino coherent scattering becomes an irreducible (at least by shielding) background to the dark matter search. Scatters coming from the direction of the Sun can, however, be rejected by introducing a directional component to the search. This enables directional detectors to search below the neutrino floor [60].

### 1.4.6 Liquid Noble Gas Detectors

Liquid noble gas detectors either measure only scintillation light from an interaction (single phase), or both ionisation and scintillation light by extracting free electrons released during an interaction (dual phase). Liquid argon and xenon are currently in use with single phase detectors. Natural xenon consists of multiple isotopes nearly half of which have non-zero angular momentum ($^{129}$Xe and $^{131}$Xe), this makes it appealing for spin dependent searches.

Discrimination between electronic and nuclear recoils can be achieved using either pulse shape discrimination, described in the next chapter, or the charge-to-light signal ratio. Recoils in noble liquids cause both excitation and ionisation. Experiments making use of both the charge and light signal, dual phase detectors, apply an electric field across the medium to drift ionised electrons away from their parent ions in the liquid phase. These electrons drift towards a separate gas phase in the detector (hence, dual phase) where the signal is amplified via proportional scintillation [61]. The initial interaction light signal from excitation is known as S1, with the second proportional scintillation signal known as S2. The ratio of these two signals depends on the particle type and allows

for discrimination against electronic recoils [62][63].

The current leading exclusion limit comes from the two-phase Xenon experiments, LUX [64] and Xenon-100 [65]. Both detectors use a two-phase Xenon time projection chamber (TPC). The 178 nm scintillation light S1 signal is detected by two arrays of photomultiplier tubes (PMTs), located above and below the target region in both experiments. The electrons drift and cause the S2 signal where the time between the two signals indicates the depth of the interaction, with the distribution of light detected in the PMT arrays giving additional horizontal position information. This allows full 3D imaging of the event location. The current upper limit cross section for LUX's first 85.3 days of live data is $7.6 \times 10^{-46}\,\mathrm{cm}^2$ for a WIMP mass of 33 GeV/c$^2$ [66]. Xenon-100's upper limit after 225 live days is $2 \times 10^{-45}\,\mathrm{cm}^2$ at a WIMP mass of 55 GeV/c$^2$ [67].

In contrast to the two-phase detection approach, single-phase detection looks for a signal using only the scintillation light produced by a nuclear recoil. The XMASS detector is a single phase experiment using xenon. It is a multi-purpose experiment which aims to detect low energy solar neutrinos, neutrinoless double beta decay, as well as direct detection of dark matter. The 835 kg target region is surrounded by PMTs in an approximately spherical configuration. XMASS makes use of the different scintillation timing profiles of electronic and nuclear recoils to discriminate against electronic recoil backgrounds; this technique is discussed further below [68]. The DEAP-3600 experiment is a single phase detector making use of liquid argon scintillation as a detection medium. Details of this experiment and detection via liquid noble gases in general is the subject of the next chapter.

Figure 1.9 shows the full sensitivity of DEAP-3600 after 3000 kg.years of exposure. The experiment requires two months of data to surpass LUX's current sensitivity at a mass of 1 TeV, and 8 months to surpass their full sensitivity. In contrast, the next generation Xenon detector, Xenon-1T, needs only 2 months of data to surpass LUX's full sensitivity and will ultimately gain the leading limit. Xenon-1T, currently under construction at LNGS contains 3500 kg of liquid xenon and is expected to gain a sensitivity of $2 \times 10^{-47}\,\mathrm{cm}^2$

within 2 years of operation [69]. Not displayed in the figure is LZ, a multi-ton scale detector which is the joint effort of the LUX and ZEPLIN collaborations. It will hold 7000 kg of liquid xenon in the target volume and is currently in the planning stages. The expected sensitivity is $2 \times 10^{-48}\,\mathrm{cm}^2$ at a dark matter mass of approximately 50 GeV [70].

# Chapter 2

# Detection with DEAP-3600

*Measure what is measurable, make measurable what is not so.*

Galileo Galilei

In this chapter the properties of a selection of the noble liquids and their use in dark matter detection will be outlined. The scintillation mechanism will be discussed with a focus on liquid argon. The time constants of the singlet and triplet excited dimer states will be stated. The use of these time constants in particle identification will be discussed. The DEAP-3600 detector, with which the following work is concerned, will be described in Section 2.2. Finally, the most prominent backgrounds to the dark matter search will be described. Determining the background level is crucial in determining an exclusion limit or signal detection significance.

## 2.1 WIMP Detecting using Noble Liquids

Liquid noble gases, liquid argon (LAr), liquid xenon (LXe) and liquid neon (LNe) in particular, have properties useful for dark matter detection. The passage of radiation

| Property | He | Ne | Ar | Xe |
|---|---|---|---|---|
| Atomic number | 2 | 10 | 18 | 54 |
| Atomic mass | 4.0 | 20.12 | 39.95 | 131.29 |
| Boiling point $T_{\mathrm{b}}$ at 1 atm [K] | 4.22 | 27.1 | 87.3 | 131.29 |
| Melting point $T_{\mathrm{m}}$ at 1 atm [K] | - | 24.6 | 83.8 | 161.4 |
| Gas density at 1 atm and 298 K [$\mathrm{gl}^{-1}$] | 0.16 | 0.82 | 1.63 | 5.40 |
| Gas density at 1 atm and $T_{\mathrm{b}}$ [$\mathrm{gl}^{-1}$] | 16.6 | 9.56 | 5.77 | 9.99 |
| Liquid density at 1 atm and $T_{\mathrm{b}}$ [$\mathrm{gcm}^{-3}$] | 0.12 | 1.21 | 1.40 | 2.94 |

**Table 2.1:** Table of properties for a selection of noble gases. [71]

through these materials causes both scintillation and ionisation giving two handles with which to detect rare physics events. In the following, scintillation in liquid argon as the primary detection method will be described in detail.

Liquid noble detectors seek to observe dark matter elastic scattering on a target atom, which recoils through the detector medium. To detect this signal some important target properties are:

- The atomic mass ($A$): the spin-independent WIMP-nucleus cross-section scales with $A^2$.
- Ease of purification: impurities dissolved in the liquid nobles can cause a decrease in light yield.
- The ability to discriminate between electronic and nuclear recoils: the majority of background events, with the exception of neutrons, are expected to cause electronic recoils; a detector must be able to distinguish between these and the nuclear recoils of WIMPs

Neon, argon, and xenon gases all exhibit properties useful for dark matter detection. A list of properties can be found in Table 2.1.

Xenon's large atomic number and high light yield make it an excellent dark matter target material. Its overlap of decay time constants mean it is better suited for dual phase

detectors. Xenon is the most expensive noble gas, a factor which becomes important for tonne scale detectors.

Neon has no long lived radioactive isotopes and good separation between decay time constants. This allows for discrimination between electronic and nuclear recoils using pulse shape discrimination [72] (see below).

Argon is the most inexpensive of the liquid nobles under consideration. Like liquid neon, its decay time constants make it excellent for particle identification using pulse shape discrimination (PSD, Section 2.1.1). Argon, however, contains trace amounts of cosmogenically occurring $^{39}$Ar which is a $\beta^-$ emitter with a half-life of 269 years and an end point energy of 565 keV [73]. The isotope is expected to cause electronic recoils with a rate of 1 Bq/kg [74]. For DEAP-3600, this causes approximately $10^{10}$ electronic recoil events which have to be discriminated against over the lifetime of the experiment. With increasing size pile-up with possible signal events will also become a problem. Use of depleted argon, with reduced $^{39}$Ar contamination, from underground sources [75] is expected to improve sensitivity of liquid argon experiments. Work is under way to procure depleted argon for DEAP-3600.

### 2.1.1 Physics of Scintillation

In noble liquids a fraction of the energy transferred by a particle to the medium causes two processes to occur which result in scintillation: one through excited atoms, $R^*$, and the other through ions, $R^+$. Both processes result in the formation of excited dimer (or excimer) states which decay releasing a scintillation photon. The rest of the energy transferred goes to elastic collisions with the atom which increases the temperature of the noble liquid. For more information on noble gas physics see [76].

Scintillation photon emission occurs in a transition between either the singlet ($^1\Sigma_u^+$) or triplet ($^3\Sigma_u^+$) first excited electronic state of the excimer to the ground state ($^1\Sigma_g^+$) [77]. The ground state potential is repulsive causing the molecule to disassociate. These two

excited states each have different decay lifetimes corresponding to whether the transition to the ground state is forbidden or not. In liquid argon the singlet state lifetime ($\tau_s$), corresponding to an allowed transition, is $7 \pm 0.1$ ns. The triplet state decay, however, is a forbidden transition requiring a spin flip. The transition is made possible due to spin orbit coupling [78]. This results in a much longer lifetime ($\tau_t$) of $1.6 \pm 0.1$ $\mu$s [79]. Noble gases with a higher atomic number than argon have stronger spin orbit coupling and therefore have shorter triplet decay lifetimes. This is reflected in the decay times of liquid krypton, 111 ns [80], and liquid xenon, 27 ns [81]. The converse is also true with liquid neon having a triplet lifetime of 15 $\mu$s [72], and liquid helium's being 13 s [82].

In the first scintillation process excited atoms form excimer states ($R_2^*$) directly with nearby ground state atoms. These excimers then decay releasing a scintillation photon via:

$$\begin{aligned} R^* + R &\rightarrow R_2^* \\ R_2^* &\rightarrow 2R + h\nu \end{aligned} \tag{2.1}$$

where $h\nu$ is the scintillation photon, typically emitted in the vacuum-ultraviolet (VUV) range [83]. Liquid argon has an emission spectrum around 128 nm wavelength, below the first excited state of argon atoms [84]. In noble liquids, the fact that scintillation occurs via excimer states ensures they are all transparent to their own scintillation light.

In the second process the ions created by the interaction bond with nearby ground state particles creating molecular ions. These molecules then recombine with free electrons to

form highly excited states:

$$
\begin{aligned}
R^+ + R &\rightarrow R_2^+ \\
R_2^+ + e^- &\rightarrow R^{**} + R \qquad \text{(Recombination)} \\
R^{**} &\rightarrow R^* + \text{heat} \\
R^* + R &\rightarrow R_2^* \\
R_2^* &\rightarrow 2R + h\nu.
\end{aligned}
\tag{2.2}
$$

The reaction then proceeds via 2.1 with the excited atom forming an excimer state which then decays releasing a scintillation photon. Liquid argon produces 40 photons/keV$_{ee}$ [85] [86]. The wavelength and decay times are the same as for the direct excitation process however the relative populations of singlet and triplet states will be different. The recombination process itself may also introduce a time delay. In liquid argon, however, this time is short ($\sim$ 1 ns) such that it has little effect on the overall time profile of the event [87]. Recombination plays an important role in both the relative populations of singlet and triplet states and the scintillation light yield for various interaction types, it will be discussed further in the next section.

### Recombination

The introduction of an electric field across the medium reduces the scintillation light yield. Under a field of order $\sim$ 10 kV/cm the light yield is reduced up to a factor $\sim$ 3. This suggests that approximately 1/3 of the scintillation light is due to direct excitation with the rest being from recombination [87]. [88] found the light yield for nuclear recoils to be reduced up to 32% for a field of 1 keV/cm.

For fast (0.5 to 1 MeV) electrons passing through liquid argon recombination enhances the singlet state process. From [87] the fraction of luminescence due to recombination was found to be 64%, with the remaining 36% from direct excitation. In [78] the ratio to of singlet to triplet states was measured with an applied 6 keV/cm field, resulting in

luminescence purely from direct excitation, and without, resulting in a combination of excitation and recombination. A singlet to triplet ratio of 0.045 was found with the field applied compared to 0.083 without showing an enhancement of the singlet state with the addition of recombination.

To first order, interactions can be characterised by linear energy transfer (LET), or $dE/dx$. Nuclear recoils and alpha interactions have a higher LET and thus produce more ionisation. This in turn enhances the singlet state channel through recombination. The species dependent distribution of singlet and triplet states allows particle identification through the use of pulse shape discrimination, described below.

The recombination process depends heavily on the event track structure i.e. the distribution and density of ionisation along the track, as well as the free electron thermalisation speed and distance. For low energy ($< 100\,\mathrm{keV}$) nuclear recoils the track structure is not well defined. The detection medium is composed of atoms of the same species as the projectile, the incoming particle can therefore transfer a large fraction of its kinetic energy at collision. This results in an atomic cascade where a large number of secondary collisions are produced, each with energies comparable to that of the initial projectile. For a detailed discussion of recombination and scintillation physics in general for both liquid argon and xenon see [81].

### Pulse Shape Discrimination

Since the decay times are so vastly different in liquid argon it is possible to estimate the fraction of singlet to triplet states by looking at the arrival times of scintillation photons, so called pulse shape discrimination (PSD). Following [89], the time dependence, $f(t)$, of scintillation photons is expected to be a linear combination of two exponentials:

$$f(t) = q\frac{1}{\tau_\mathrm{s}}\exp\left(\frac{t}{\tau_\mathrm{s}}\right) + (1-q)\frac{1}{\tau_\mathrm{t}}\exp\left(\frac{t}{\tau_\mathrm{t}}\right). \tag{2.3}$$

Here, $\tau_s$ and $\tau_t$ represent the singlet and triplet time constants as above, and $q$ represents the fraction of photons produced by excimers in the singlet state. Figure 2.1 shows this equation in relation to nuclear and electronic recoil data. In [89] $q$ was found to sit around 0.3 for electronic recoils and 0.7 for nuclear recoils.

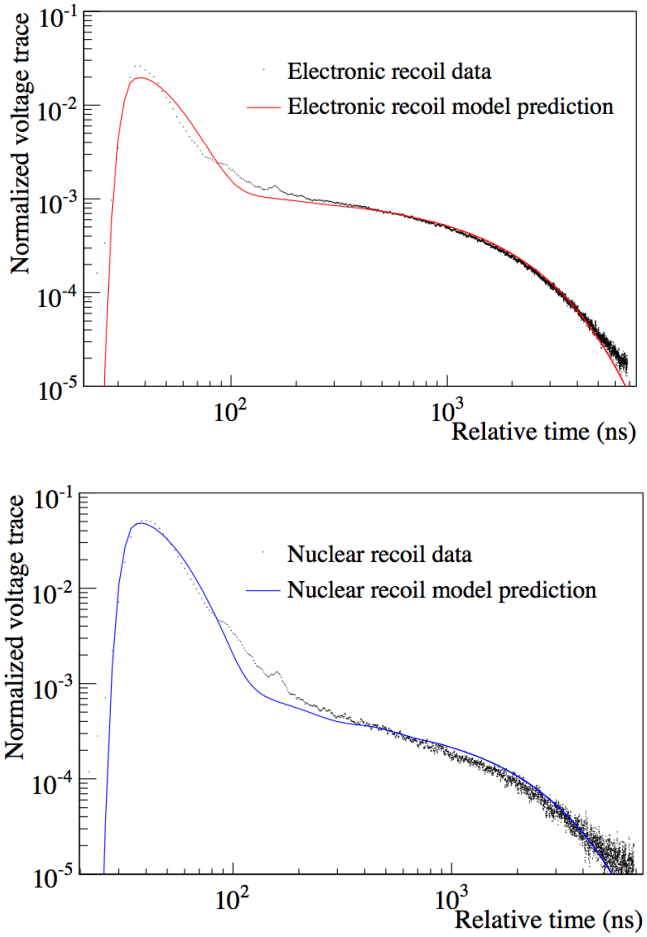


**Figure 2.1:** From [89], mean voltage traces for electronic and nuclear recoil events of 80 to 99 photoelectrons. Model predictions follow Equation 2.3. Here $q_{\text{nuclear}}$ was found to be $0.702 \pm 0.01$ and $q_{\text{electronic}}$ was found to be $0.279 \pm 0.015$.

A common [89, 90, 88] measure of the "promptness", q, of an event is the fraction, $F_{\text{prompt}}$, of light in some early time window over the total light in the event:

$$F_{\text{prompt}} = \frac{\int_{t_0}^{t_p} Q(t)\ \mathrm{dt}}{\int_{t_0}^{t_{\text{end}}} Q(t)\ \mathrm{dt}}. \tag{2.4}$$

Here $Q(t)$ is some measure of the amount of light produced over time (e.g. PMT charge), $t_0$

is the beginning of the event, $t_{\text{end}}$ is the end of the event, and $t_{\text{p}}$ is the prompt timing window where $t_{\text{p}} - t_0$ is usually around 90 to 150 ns. Figure 2.2 shows the $F_{\text{prompt}}$ distribution in the DEAP-1 detector for electronic and nuclear recoil events from calibration sources. The discrimination power strongly depends on the number of photoelectrons (PE) seen, making explicit the importance of light yield in argon scintillation experiments. A higher light yield will ensure better discrimination between electronic and nuclear recoils at lower energies. In the chosen energy window of 43 to 86 $\text{keV}_{\text{ee}}$ good separation between the two types of event can be seen. $t_{\text{p}}$ was chosen to be 150 ns in this experiment. Maximising the separation between electronic and nuclear recoil events drives the choice of prompt window size. Estimators of $q$ for use in PSD, including $F_{\text{prompt}}$, will be discussed further in chapter 3.

DEAP-3600 requires a level of PSD discrimination to better than $10^{-10}$. This level is possible at an energy threshold of 15 keV with a light yield of 8 PE/keV. This has been demonstrated with analytic modelling of the DEAP-1 data, see Figure 2.2. Simulation of the DEAP-3600 detector suggests that this light level will be achieved. Stringent purity requirements on the liquid argon which will minimise light loss from contamination, and the choice of optical materials, described below, ensure a maximal potential light yield.

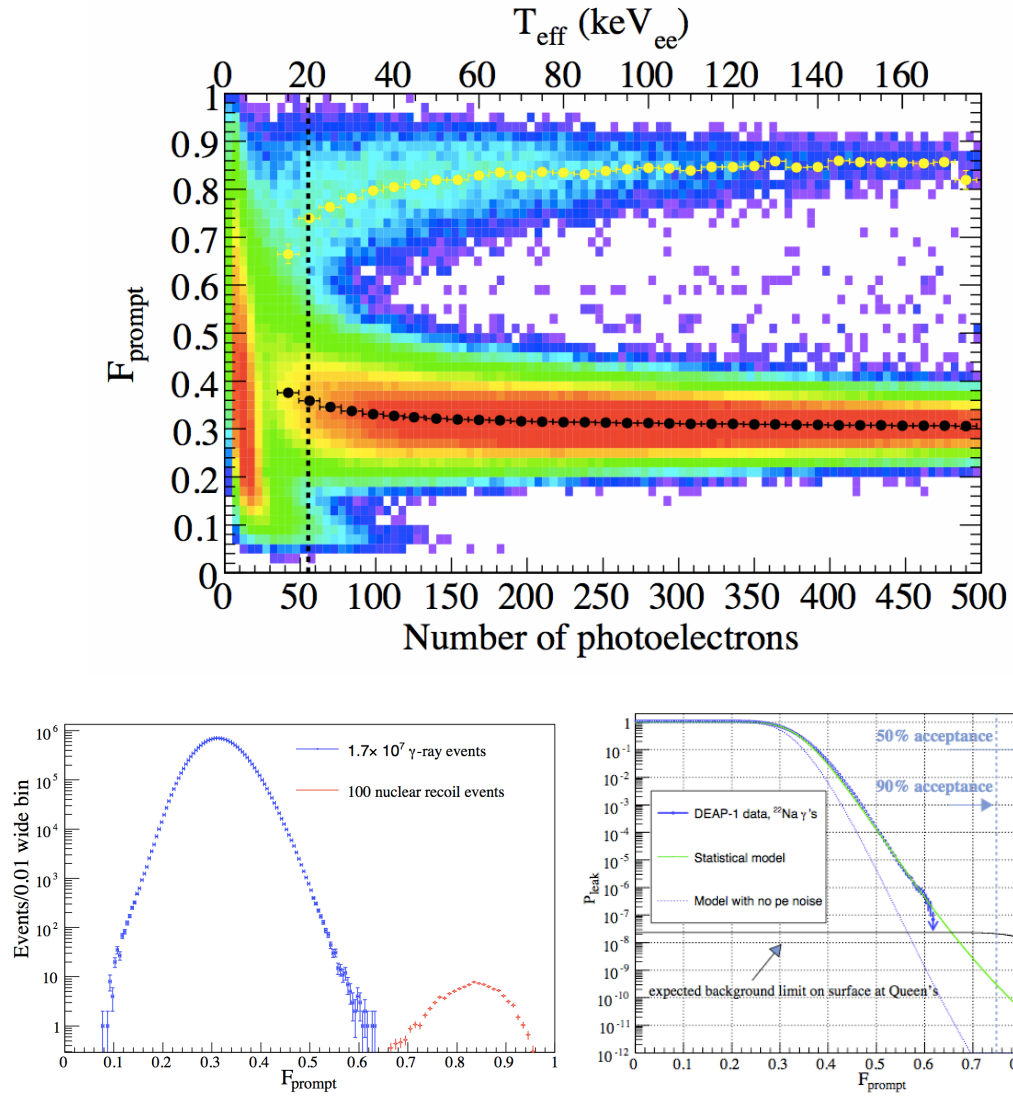


**Figure 2.2:** Top: The $F_{\text{prompt}}$ distribution of 16.7 million $\gamma$ events from an $^{22}$Na calibration source (lower band), and 100 nuclear recoil events from an AmBe calibration source in the DEAP-1 detector (upper band) versus the total number of PE detected in the event. Discrimination power depends strongly on the number of PE detected. Bottom: Left: $F_{\text{prompt}}$ events from between approximately 43 and 86 keV$_{\text{ee}}$. Good separation can be seen between the electronic recoil, $\gamma$, events around $F_{\text{prompt}} = 0.3$ and nuclear recoil events around $F_{\text{prompt}} = 0.82$. Right: Leakage probability distribution of $^{22}$Na data between 120 to 240 PE as a function of $F_{\text{prompt}}$ along with an analytic model. The analytic model predicts a discrimination power of better than $10^{-10}$ at 50% acceptance. From [91].

### Nuclear Recoil Photon Yield

Along with different decay times a difference in light yield has also been shown to occur between nuclear and electronic recoils of the same energy [86]. Interactions with a higher LET, such as nuclear recoils, produce fewer photons than those with lower LET for the

same total energy transfer. The nuclear recoil scintillation efficiency, $\mathcal{L}_{\rm eff}(E)$, is generally quoted in reference to the scintillation yield for 122 keV $\gamma$ rays from a $^{57}$Co source. That is $\mathcal{L}_{\rm eff}(E) = W_{\rm scint,e}(122\ {\rm keV})/{\rm W_{scint,nr}(E)}$, where $W_{\rm scint,e/nr}$ is the energy required to produce one electronic, $e$, or nuclear, $nr$, recoil scintillation photon. In liquid argon $\mathcal{L}_{\rm eff}$, was found to be constant at $0.25 \pm 0.02$ above 20 keV [92]. This discrepancy between electronic and nuclear recoil light yields leads to the use of the electron equivalent unit of energy, ${\rm keV_{ee}}$. This is to be compared with the nuclear recoil energy ${\rm keV_r}$ which, in liquid argon using the constant scintillation efficiency $\mathcal{L}_{\rm eff}(E) \rightarrow \mathcal{L}_{\rm eff}^{\rm Ar} = 0.25$, gives

$$[{\rm keV_{ee}}] = \mathcal{L}_{\rm eff}^{\rm Ar} \times [{\rm keV_r}]. \tag{2.5}$$

For a light yield of 8 PE/${\rm keV_{ee}}$, for example, 100 PE would be equivalent to 12.5 ${\rm keV_{ee}}$ and 50 ${\rm keV_r}$. Figure 2.3 shows the scintillation efficiency as a function of energy, which can be seen to be flat within error above 20 ${\rm keV_r}$. As stated above, the weighted mean above 20 ${\rm keV_r}$ was found to be $0.25 \pm 0.02$. Uncertainty on this number is one of the main systematics to the dark matter search. For a WIMP mass of 100 GeV and an energy window of 15 to 30 ${\rm keV_{ee}}$ a difference of 0.02 in the light yield would affect change the expected rate by 23%.

This difference between nuclear and electronic recoils is known as quenching. Quenching generally depends on ionisation and excitation density and the overall structure of the particle track. There are several mechanisms through which it occurs:

- Heat: for nuclear recoils, as mentioned above, a significant fraction of energy is spent in collisions where the entire atom recoils, creating no ionisation or excitation and merely increasing the kinetic energy of the surrounding particles.
- Electron escape: In the low LET regime if an ionised electron is not thermalised before leaving a critical radius from the parent ion it will not recombine for an extended period of time [86]. Thus, photons may not be seen in the time window of observation.

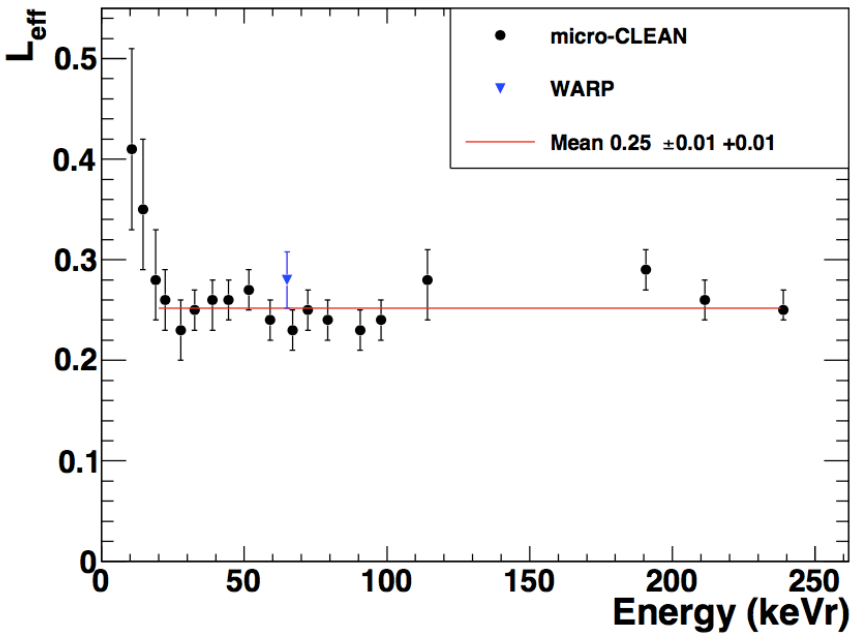


**Figure 2.3:** Scintillation efficiency as a function of energy from 10 to 250 $keV_r$ as measured by the micro-CLEAN experiment. The red line is the weighted mean for data above 20 $keV_r$ found to be $0.25 \pm 0.02$. From [92].

- Biexcitonic quenching: In the high LET regime excimers may undergo a process of biexcitonic quenching via

$$R^* + R^* \rightarrow R + R^+ + e^-. \tag{2.6}$$

  Here the emitted electron carries off the excess energy. After initially having two excimers each emitting a photon we are left with one photon after recombination [86].

- Impurities: Liquid argon's scintillation light yield is greatly diminished by dissolved impurities. This can occur through energy transfer from the excimers to the contaminant [93]. Electronegative impurities can also trap electrons liberated through ionisation. This reduces the number of electrons available for recombination and diminishes the light yield. For example, an introduction of $O_2$ at 1 ppm can reduce the light yield by 20% [94]. Argon purification is, therefore, paramount to a dark

matter search.

## 2.2 DEAP-3600

DEAP-3600 is a single phase, liquid argon, dark matter direct detection experiment. The detector is composed of 3600 kg of liquid argon held inside an acrylic vessel (AV) surrounded by 255 R5912-HQE Hamamatsu photomultiplier tubes (PMTs) (discussed in Section 2.2.2). Each of the 255 PMTs are attached to 456 mm long acrylic light guides (LG) which are bonded directly onto the AV. The light guides thermally insulate the PMTs from the argon volume and, together with the AV, shield the argon from neutrons produced both in the PMT glass and externally (Section 2.2.3). The inside of the AV is coated with a wavelength shifter which converts the 128 nm argon scintillation light to the visible spectrum which is detectable by the PMTs (Section 2.2.4). Between the light guides sit "filler blocks", composed of alternating layers of high density polyethylene and styrofoam, which provide both thermal insulation and neutron shielding in addition to the AV and light guides (Section 2.2.5). This assembly is surrounded by a steel shell (Section 2.2.6) which sits inside a water veto (Section 2.2.7). A cutaway rendering of the DEAP-3600 steel shell and inner components can be seen in Figure 2.4.

The purification and cryogenic systems will be outlined in Section 2.2.8. The various calibration systems used by DEAP-3600 will be outlined in Section 2.2.9, with a more detailed discussion taking place in chapter 4. Finally, the electronic readout and trigger systems of the detector will be discussed in Section 2.2.10. The following is detailed in [95]. In the next section the design specification region of interest (ROI), hereafter referred to as the "nominal" ROI, will be discussed which will inform the rest of this text.

### 2.2.1 "Nominal" Region of Interest

DEAP-3600 is designed to be a single phase direct detection experiment, competitive at the 1000 kg scale. This fiducial mass drove the design of the full radius, with the aim of keeping

surface background leakage to $< 0.2$ events over 3 years of running. As mentioned above, the level of pulse shape discrimination was calculated by extrapolation of the DEAP-1 model using an expected light yield of 8 PE/keV$_{ee}$ (Figure 2.2). A window of 120 PE (15 keV$_{ee}$) to 240 (30 keV$_{ee}$) PE was chosen to give an expected $^{39}$Ar background rate of $< 0.2$ events over 3 years which leak into the 50% WIMP acceptance region. The overall neutron rate specification is also $< 0.2$ events in the region of interest over 3 years of running with 50% WIMP acceptance. The acrylic vessel is the primary means of mitigation of neutron events. The upper PE limit is constrained by this neutron rate. Increasing the size of the upper PE limit introduces the possibility of more background events at a rate which is not compensated for by an increase in signal. Fission fragments associated with $^{210}$Po decays, for example, sit just above this energy window. The overall background rate specified is $< 0.6$ events over 3 years of running in the region of interest. DEAP-3600 is in the commissioning stage and true background values are in the process of being measured. Further to this, parameters of the detector model will be constrained with calibration data. With an accurate detector model the region of interest will be optimised. The 50% WIMP acceptance rate, for example, may be modified to maximise signal/$\sqrt{\text{signal} + \text{background}}$. The first dark matter analysis will use the nominal region of interest, as such, it will be referred to and used as a basis of comparison throughout the rest of this text.

### 2.2.2 Photomultiplier Tubes

DEAP-3600 uses 8" Hamamatsu R5912-HQE PMTs, the high quantum efficiency (HQE) version of the R5912. These tubes have a modified version of the bialkali photocathode which is designed to increase quantum efficiency. As such, they boast a minimum quantum efficiency of 32%, with some reaching over 40% at peak wavelength, compared to a typical value of 22% for the standard R5912 [96]. Spectral response characteristics of an example HQE PMT is shown in Figure 2.5. The maximum quantum efficiency is 42.2% at 390 nm wavelength incident light. The PMT operating voltages are determined such that the gain measured at the anode is approximately $0.5 \times 10^7$, with half the signal going to base termination. Given this, the single photoelectron (PE) charge is $e \times 0.5 \times 10^7 = 0.8\,\text{pC}$.

However, there is amplification due to the signal conditioning boards in the electronics chain described below. Figure 2.6 shows the single PE charge distribution for one of the internal PMTs. Data was taken during commissioning of the detector using the aluminium acrylic reflectors (AARF) optical calibration system, discussed below and further in chapter 4. Both full waveform and zero length encoded (ZLE) data (Section 2.2.13) are shown. Full waveform data was taken when the AARF system was not running, confirming the position and size of the pedestal. The mean of the single PE charge is approximately 10 pC. The PMT operating temperature is expected to be maintained at greater than $-30\,^{\circ}$C. There was found to be no significant change of PMT efficiency when testing at $-40\,^{\circ}$C. Operating above this temperature ensures no drop in over all light yield due to thermal effects. Relatively warm temperatures are achieved via the attachment of a thin copper sleeve around each PMT. The sleeve acts as a heat short which locally raises the temperature of the PMT.

The WIMP search takes place in the low PE range, $\sim$ 50 to $\sim$ 300 PE isotropically distributed across 255 PMTs. As such, PMT artifacts, such as after-pulsing and double-pulsing, can have a large effect on energy reconstruction and PSD. After-pulsing, for example, is caused by gaseous impurities ionised by passing photoelectrons subsequently striking the photocathode and releasing more PE. This causes pulses to appear later in the waveform which are unrelated to the physics of the event. These later pulses cause PSD variables like $F_{\text{prompt}}$ to be driven to lower values. Characterisation of the various types of PMT pulse and a method for identifying and removing after-pulses will be discussed in detail in chapter 3.

**Magnetic Compensation** The presence of external magnetic fields, even relatively weak fields such as the Earth's, can adversely affect the performance of PMTs. The field influences the trajectories of photoelectrons travelling from the photocathode to the first dynode causing them to miss and, ultimately, diminish the collection efficiency [98]. A magnetic flux parallel to the photocathode surface (perpendicular to the normal of the PMT) will have the greatest effect on the collection efficiency. The electron trajectories

along the dynode stack are also affected, with an external field having an adverse affect on the PMT gain. For the PMTs of DEAP-3600 a field strength of 0.5 G corresponds to a 25% loss in collection efficiency and a 20% loss in gain. An overall loss in collection efficiency would result in a reduced light yield by the same amount. Elimination of this affect is important so discrimination power can be retained.

There are two detector components in place to compensate for the Earth's magnetic field at the experiment site: passive shielding for each PMT, and magnetic compensation coils surrounding the entire detector. The vertical, $B_z$, component of the Earth's magnetic field affects the majority of the PMTs in the detector; this is compensated for using a two-pair coil arrangement shown in Figure 2.7. The field strength, calculated by Radia [99], is shown in Figure 2.8. The residual horizontal field component would lead to a 2% loss in overall PMT efficiency. This is reduced to below 1% by passive shielding. FINEMET was chosen as the shielding material for its flexibility, light weight, and relatively high permeability [100].

### 2.2.3 Acrylic Vessel and Light Guides

The AV acts as both a containment vessel for the liquid argon, with the light guides shielding the PMTs from cryogenic temperatures, and a neutron shield. It can be divided into three sections, the hollow sphere of the containment vessel, the 255 light guides, and the neck which provides access inside the AV. The hollow sphere has an inner radius of 85 cm and a minimum thickness of 5 cm. 255 stubs are arranged around the outer surface which the light guides are attached to. The light guides are directly bonded to the stubs to maximise transmission from the argon volume. The AV is open at the top allowing for the addition of a 25 cm inner diameter neck. This provides access for the argon cooling system.

Different materials were chosen for the AV and light guides, driven by radio-purity and optical requirements. Being in contact with the liquid argon the AV had a more stringent radio-purity requirement; $\alpha$ decay products on the surface may produce scintillation

light which results in them being reconstructed near the centre of the detector, potentially looking like signal events. Stringent radio-purity requirements and fiducialisation in reconstruction reduce the potential number of these events. Light transmission efficiency, in contrast, was the more important consideration for the light guides. This would ensure minimal loss of potential light yield and, therefore, discrimination power.

Spartech Polycast UVA acrylic was chosen for the light guides [102]. This material has good transmission at 420 nm, the peak of the re-emission spectrum of the wavelength shifter, with an attenuation length of approximately 3.5 m. Working with Spartech, radio purity requirements for the material could also be met. Detailed information on the raw material supply chain was supplied by the company, and production site visits by DEAP collaboration members was also arranged. The light guides also provide thermal insulation to the PMTs. This, along with the copper heat shorts, enables the PMTs to be operated at non-cryogenic temperatures.

The AV is made from methyl methacrylate (MMA) produced by the Thai MMA Co. To minimise the effect of radon which built up on the AV surfaces during construction the inner surface of the AV was sanded off. A resurfacing device was built at Queen's University, Ontario, for the purpose. Two diametrically opposed sanding heads, moving in both $\theta$ and $\phi$ directions, remove up to 1 mm of acrylic. A continuous water flush operates during sanding removing sediment. This is extracted through a suction line next to the sanding head. Figure 2.9 provides an overview of the resurfacer design.

### 2.2.4 Tetraphenyl Butadiene Re-emission Spectrum and Deposition

The R5912-HQE PMTs used in DEAP-3600 are maximally sensitive to the visible spectrum. Liquid argon, however, scintillates at 128 nm in the VUV range. Scintillation light must therefore be wavelength shifted before it is detected. Tetraphenyl butadiene (TPB) acts as the wavelength shifter in DEAP-3600.

From [103], Figure 2.10 shows the TPB fluorescent re-emission spectrum under illumina-

tion of various wavelengths of UV light. Under 128 nm illumination the TPB re-emits with a visible wavelength of 420 nm, close to the peak efficiency of R5912-HQE PMTs. The efficiency, the number of emitted photons per incident photon, of TPB was also measured in [103]. Figure 2.11 shows the total efficiency, assuming re-emission follows a Lambertian function, found for various incident wavelengths. A value of approximately 1.2 was found at a 128 nm incident wavelength. This would suggest the occasional emission of a secondary photon during fluorescence given a sufficiently high energy incident photon. This has the potential to affect our energy resolution if the light yield is incorrectly calculated. However, this emission probability is included in the optical model in simulation and is thus taken into account in the analysis.

The inside of the acrylic vessel was coated with TPB using physical vapour deposition. Figure 2.12 shows the TPB evaporation source constructed to do this. Black filament wrapped around the outside of the sphere is used to heat a copper crucible housed inside, evaporating the TPB powder contained within it. This source was lowered into the centre of the acrylic vessel, which was under $10^{-6}$ mbar vacuum, where deposition took place. A final thickness of $2.8\,\mu$m was measured by an Inficon Front Loaded Quartz Deposition monitor located at the neck of the acrylic vessel. $29.4 \pm 0.2$ g of TPB powder was placed in the crucible, assuming a uniform coating this correlates with a $3.0 \pm 0.02\,\mu$m thickness by mass [104]. Large scale deviations in uniformity will result in mis-reconstruction of the position as more light will be generated in the thicker areas combined with an increase in scattering. The extent of the non-uniformity will be measured using the optical calibration systems described below.

### 2.2.5 Filler Blocks

The void between the light guides is filled with blocks consisting of alternating insulating and neutron shielding materials. Polyethylene, chosen for neutron shielding, was placed between layers of styrofoam used for thermal insulation. Polyethylene, with its greater hydrogen density, is a more effective neutron shield and has a lower overall density than

acrylic. The filler blocks are labelled in Figures 2.4 and 2.13.

The contraction of both the acrylic vessel and filler blocks due to cooling had to be taken into account when machining and positioning the blocks. As such 5 mm gaps were left between the blocks and light guides to account for manufacturing tolerances and to prevent the blocks binding to the light guides during contraction. Retaining springs positioned at the PMT end of the light guides push the filler blocks against the AV and keep them centred while the AV and light guides shrink.

### 2.2.6 Steel Shell

The steel shell, which can be seen in Figure 2.4, houses and supports all of the internal detector components. This includes the AV, LGs, filler blocks, PMTs, cables, and the liquid argon itself. Suspended by its neck from the deck in the SNOLAB cube hall it is both water and light tight. The vessel is designed to be able to withstand a maximum pressure of 30 psig (pounds per square inch gauge). This is required to contain the argon during boil-off should the AV fail. During normal running the inner volume is maintained as a vapour space while being continuously purged with low-radon nitrogen gas.

The steel vessel was fabricated from 304 stainless steel by All-Weld, Toronto. With its inner diameter of 337.82 cm (133 inches), mine shaft size constraints meant it had to be cut into 6 pieces before being transported underground in October 2012. Once underground it was then re-welded together into hemispheres which could subsequently be bolted together once the internal components were in place.

### 2.2.7 Water Veto

The steel shell sits inside an 8 metre diameter tank of ultra pure water. Mounted to the outside of the steel shell 48 PMTs, facing radially outward, act as cosmic muon veto by detecting potential Čerenkov light. SNOLAB is based at the 6800 level (2 km underground) of Creighton mine in Lively, Ontario, Canada. This depth gives the lab an overburden of

6010 m water equivalent [105] which significantly reduces cosmic ray flux. The muon flux to be tagged is less than 0.27 $\mu/\mathrm{m}^2/\mathrm{day}$. Muons can potential cause neutrons to elastically scatter in the region of interest, looking exactly like dark matter; without the veto this rate is expected to be $< 0.042$ events in three years of running.

The water also acts as a shield for other external radiation including, for example, neutrons from the rock walls of the lab which are expected to number around 4000 neutrons/$\mathrm{m}^2$/day.

### 2.2.8 Purification and Cryogenic Systems

As discussed above, the purity of the liquid argon target has a large effect on the light yield. Electronegative chemical contaminants trap electrons liberated by ionisation and reduce the argon triplet lifetime by non-radiative quenching, thus harming discrimination ability. Also, radioactive contamination of the argon by radon and progeny will cause background events from alpha decay. Thus, the purification system must reduce both the radon and electronegative chemical content of the argon.

The system is designed to reduce electronegative impurities to $< 1$ ppb and radon emanation to $\leq 5$ $\mu$Bq over the target volume. There are five main components arranged in a loop:

- Process pump: drives the argon gas through the system. Argon gas is injected into the system at room temperature (300 K) before this point. The gas itself can come from compressed gas cylinders or from a large storage dewar attached to the system.
- Getter: reduces chemical contaminants. The getter accepts high purity argon and reduces contaminants to $< 1$ ppb.
- Charcoal trap: removes radon. This takes argon gas from the getter at 300 K and pre-cools it to 100 K before it is passed through the charcoal. The gas is then passed through a 5 $\mu$m filter before entering the condenser column.

- Condenser column: liquefies the argon before it is fed into the AV. The condenser consists of a stainless steel coiled tube filled with liquid nitrogen.
- Boiler: warms the liquid argon to remove it from the AV. The argon can then be fed back through the purification loop or transferred to the storage dewar.

Maintaining the liquid argon at cryogenic temperatures is achieved using a parallel liquid nitrogen system. Liquid nitrogen is kept in a separate dewar at the top of the SNOLAB cube hall, above the experiment. It is then gravity fed into the detector where it provides cooling for the above mentioned process systems and the argon itself within the condenser column and the main cooling coil. The main cooling coil, which maintains the temperature of the target volume inside the AV, sits within the neck of the detector. The liquid phase of the argon is maintained through the use of flow guides at the base of the neck which regulate convection. Through the use of computational fluid dynamics they were designed to guide warm argon up the neck to be cooled by the coils and back down into the centre of the detector. The main neck cooling coil and the flow guides are shown in Figure 2.13.

### 2.2.9 Calibration

DEAP-3600 is calibrated using various radioactive and optical sources which can be positioned throughout the detector. Calibration will be covered in detail in chapter 4, an overview of the calibration systems will be presented here.

Determining the optical properties of the detector in situ is important, particularly after the bonding and annealing process. Accurately determining the relative efficiency of each LG/PMT module coupled to the AV is paramount for the calibration of position reconstruction. Several light injection systems have been built for this purpose.

The aluminium acrylic reflectors (AARFs) provide DEAP-3600 with a permanent light injection system. Optical fibres are attached to twenty small acrylic reflector units placed at the PMT end of the LGs. These AARFs direct the injected light from the edge of the light guide to the centre of the PMT face, Figure 2.14. From here a fraction of the

light reflects off the PMT face and enters the detector. The injected light will be used to determine the single photoelectron charge distribution and monitor it through time. They will also be used to monitor other time dependent PMT effects such as drift and after-pulsing. Prior to filling with argon a separate optical light source was placed inside the acrylic vessel. This consisted of a flask filled with diffusing gel which acted as a centrally positioned light source in the detector. Data from this source will be used to measure channel to channel timing offsets, TPB uniformity, and relative PMT efficiencies.

Surrounding the steel vessel, inside the water tank, sit various calibration ports shown in Figure 2.15. Calibration ports A (Cal A), B, and E are suspended vertically in the water tank allowing radioactive sources to be lowered from the deck above. Cal F runs around the spherical body of the detector, crossing at the neck. This allows a source to be deployed around the full circumference of the target volume.

Two radioactive sources are used in DEAP-3600: an AmBe neutron source and a $^{22}$Na gamma source. The AmBe source will be deployed in the vertical calibration tubes, populating the detector volume with nuclear recoil like events. This will be used to characterise the PSD distribution for nuclear recoils. The $^{22}$Na source will be run around the Cal F port populating the circumference of the detector with gamma events. This will also allow for PSD characterisation as well as determining the light yield, and position reconstruction resolution near the acrylic vessel.

### 2.2.10 Electronics

The electronics of DEAP-3600 have to cope with two distinct challenges. First, a high trigger rate, namely 3.6 kBq from $^{39}$Ar events. Second, a large range of energies, specifically from the expected keV ($\sim$ 10 PE) of WIMP events to the many MeV ($\sim 10^4$ PE) from possible $\alpha$ background events. With these constraints the design specification for the DAQ required the data rate to be kept below 5MB/s while, simultaneously, ensuring all possible WIMP like events are recorded. The trigger system is designed to reduce the event rate, keeping the data rate low and ensuring the system does not become 100% busy. While

separate sets of digitizer boards attached to high gain and low gain output are designed to handle the large dynamic range.

A schematic of the DEAP-3600 electronics is shown in Figure 2.16. The system is divided into three sections, the front end, the data acquisition system, and the trigger system. The front end system includes the PMTs, and signal conditioning boards (SCBs) (Section 2.2.11). The data acquisition system (DAQ) includes the digitizer boards and readout PCs (Section 2.2.13). Finally, the trigger system includes the digitizer and trigger module (DTM) and the pulse pattern generator (PPG), used for synchronisation (Section 2.2.12).

### 2.2.11 Front End System

The front end includes the high voltage supply for all PMTs and signal conditioning boards. The high voltage supply is adjusted individually for each PMT to ensure a uniform $10^7$ gain across the whole detector. The PMT signals, from both the inner detector PMTs and the outer veto PMTs, are sent through the SCBs. These broaden the PMT signal and provide both low gain and high gain output for each PMT.

The high gain output is sent to CAEN V1720 digitiser boards which have a 4 ns sampling time. Each PMT pulse is 10 ns wide, the SCBs broaden this by a factor of 2 or 3 to ensure the V1720 boards can record an adequate number of samples along the leading edge. Pulses which saturate the high gain channel are sent through the low gain channel to CAEN V1740 digitiser boards. These boards have a slower, 15 ns, sampling time. The PMT pulse is widened and attenuated by a factor of 10 in amplitude by low gain channel. This allows the shape of large pulses, from radioactive background events, to be recorded alongside the relatively small signal events. Veto PMT output is sent to a single dedicated V1740 board.

There are 26 SCBs in total; 22 for the 255 inner detector PMTs, and 4 for the 48 veto PMTs. Each board is connected to 12 PMTs. An analogue sum of the signal from all 12 boards is sent to the DTM which makes the trigger decision.

### 2.2.12 Trigger System

DEAP-3600's trigger decision is made by the DTM. This decision is based, primarily, on the 22 analogue sum signals supplied by the SCBs. The DTM also provides the master clock synchronising all digitiser boards. It also allows for external triggering of the various calibration devices, as well as external triggers from the veto PMTs, calibration devices, and software. Finally, it throttles data collection if the DAQ becomes busy.

The decision as to whether to trigger on internal or external information is based on a set of trigger sources. These map to a set of trigger outputs which decide which devices should receive the trigger signal and whether or not the event should be "pre-scaled". Here pre-scaling means that a configurable percentage of triggered events are ignored. There are four types of triggers available:

- Physics trigger: used during normal running. Discussed in detail below.
- Minimum bias trigger: user for detector characterisation. The 22 separate analogue sum outputs are examined as well as the overall sum. The trigger decision is then based on a threshold for a given number of samples for each of the 23 inputs.
- Periodic trigger: either fires after a set number of clock cycles or following an exponential distribution. The exponential trigger has a similar time profile to that of liquid argon scintillation events, this allows for testing of the effect of multiple triggers in a short time period, for example.
- External trigger: this can come from either the muon veto PMTs or a calibration source. The veto PMTs are connected, through the SCBs, to a V1740 board which sends a trigger signal to the DTM if enough PMTs have fired in coincidence. The neutron and gamma calibration systems each contain small PMTs used for tagging. A signal from these travels to a V1720 which sends a trigger signal to the DTM. The AARF light injection system sends a signal to the DTM when it is fired.

The physics trigger is designed to accept all events in the WIMP energy and PSD region

of interest. It also reduces the acceptance of events sitting in the $^{39}$Ar region through pre-scaling. Event selection is based on three parameters $E_{\text{short}}$, $E_{\text{long}}$, and $F_{\text{prompt}}$. $E_{\text{short}}$ and $E_{\text{long}}$ are calculated from rolling integrals of the sum of the 22 analogue sums over two time windows. Starting from the same time $E_{\text{short}}$ corresponds nominally to 300 ns and $E_{\text{long}}$ to 1600 ns. $F_{\text{prompt}}$ is then calculated, in this case, from the ratio of short to long time windows. Each event is then assigned a trigger out according to its ($E_{\text{short}}$, $F_{\text{prompt}}$) value. The ($E_{\text{short}}$, $F_{\text{prompt}}$) space is divided into 6 regions shown in Figure 2.17. Very low energy events are assumed to be noise and discarded. Medium 50PE $\lesssim$ E$_{\text{short}}$ $\lesssim$ 300PE, high $F_{\text{prompt}} \gtrsim 0.5$ events are all recorded whereas low $F_{\text{prompt}} \lesssim 0.5$ events will be pre-scaled. There is more overlap in $F_{\text{prompt}}$ in the low energy region so the pre-scaling requirements differ. This trigger system is highly configurable, allowing all WIMP-like events within our chosen region of interest to be kept while reducing the number of background events written to disk. A 50 keV nuclear recoil event using the preliminary window above triggers with approximately 99.6% efficiency, the limiting factor being the choice of the $F_{\text{prompt}}$ window. 25 keV nuclear recoils trigger at 93.8% efficiency, and 75 keV trigger at 99.9%.

### 2.2.13 Data Acquisition System

The data acquisition system is comprised of the V1720 and V1740 digitisers which are connected to the read out system PCs. The 32 V1720 cards are connected to 4 of the PCs, the 4 V1740 cards are connected to a single PC, and the veto V1740 is also connected to a single PC.

The V1720 boards are capable of storing data with zero length encoding (ZLE). This means that waveforms are only recorded if, for a given number of samples, they pass a certain threshold. Extra samples before and after those that break the threshold are also recorded. This acts as a noise gate, ensuring single PE pulses are recorded while drastically reducing the data size. The V1740s, however, do not use ZLE and store only full waveforms. Since the low-gain information is only needed when the high-gain channel is saturated V1740 information is not read out for every event.

Each read out PC runs front end software which records the sampled waveforms from the connected boards and sends it to a master computer. Along with digitizer samples the charge and time (QT) information for each ZLE waveform block is calculated and passed along with the V1720 data. The master computer filters the event and can act as a secondary software trigger; analysing V1720 data and making further decisions as to whether data should be saved or not. The master computer also takes information from the DTM, veto, and calibration hardware filters combining everything to build a complete event.

## 2.3 Backgrounds

There are several backgrounds to the dark matter search in DEAP-3600. Each one of them can potentially cause a WIMP-like event in the region of interest. The most prominent backgrounds are described below along with reduction efforts in hardware and software.

### 2.3.1 Neutrons

A problematic background for WIMP-like dark matter experiments such as DEAP-3600 is neutrons. Due to their massive and electrically neutral nature they can mimic a WIMP signature. That is, a neutron may elastically scatter only once in the target volume, leaving a WIMP like nuclear recoil. The neutron-$^{40}$Ar coherent scattering cross section is 0.421 barns [106] which should be compared to the expected sensitivity of the experiment of $10^{-20}$ barns. Neutron shielding is, thus of paramount importance.

Sources of neutrons from ($\alpha$,n) due to Uranium, Thorium, and Radon contamination in all detector components and materials surrounding the experiment were considered, along with neutrons produced in cosmic ray interactions. These neutrons were simulated in the full GEANT4 detector geometry of the experiment site, the water veto, and the detector itself. Background rates were estimated after the full electronics response was simulated and event reconstruction was performed. The total number of WIMP-like events appearing

inside the fiducial volume after 3 years of running was then estimated to be $< 0.379 \pm 0.042$ [107]. The majority of events, $< 0.140 \pm 0.033$, are due to neutrons being generated in an $(\alpha, n)$ reaction from Uranium and Thorium impurities in the glass of the internal PMTs. A gamma assay was performed to determine the abundances of $^{238}$U = 74.1 ppb, $^{235}$U = 0.3 ppb, and $^{232}$Th = 34.2. The neutron yield from each source was then calculated following [108]. Each chain was in secular equilibrium with the neutron yield being determined by adding the intensity weighted yields for particle decay for each element in the PMT glass. This gave a total of $2.6 \times 10^5$ neutrons generated in all the PMT glass over a three year period.

The $10^{-6}$ level of attenuation is due to the acrylic vessel, light guides, and filler blocks thermalising external neutrons. For the first month of physics running $< 0.01 \pm 0.001$ neutrons are expected to cause WIMP like events in the detector, with the error being the statistical uncertainty. High statistics neutron simulations are being generated in order to reduce this error and characterise systematics.

### 2.3.2 Surface Alphas

Possible background events can occur from radon contamination; decays of it and its progeny on the inner surface of the acrylic vessel can cause WIMP-like events. This may be from daughter nuclei causing nuclear recoils around the edge of the volume or from alpha scattering in the TPB and argon.

As mentioned above, to combat this, the re-surfacer was run for 200 hours. This removed $\sim 0.4$ mm of acrylic from the inner walls of the AV. Figure 2.18 shows $^{210}$Pb $\alpha$ activity as a function of depth into the acrylic before resurfacing, after the AV had been exposed to radon-laden air. The blue line shows surface activity from radon daughter deposition, this amounts to $5 \times 10^4$ $\alpha/\mathrm{m}^2/\mathrm{day}$. The red line shows diffusion of surface alphas into the bulk of the acrylic. Once a layer of surface material is machined off this becomes the new surface activity. The cyan line shows the upper limit of $^{210}$Pb activity derived from an assay of the acrylic [109]. Removal of $\sim$0.4 mm leaves the residue activity at

$\sim 10\,\alpha/\mathrm{m}^2/\mathrm{day}$. Preliminary simulation studies have found that this depth corresponds to approximately 0.566 WIMP like events in 3 years reconstructing within the 550 mm fiducial radius. The full detector geometry, DAQ response simulation, and reconstruction were applied [110]. This value will be constrained through full decay chain simulation and fitting to data outside the fiducial volume, 550 < radius < 850 mm, along with further on site assays.

Low energy alphas produced in the neck of the detector pose a further problem. The position reconstruction algorithms do not take the neck geometry into account as both assume a spherically symmetric distribution of PMTs. This leads to events created in the neck potentially reconstructing within the radial region of interest. These events tend to reconstruct along the axis of the neck so re-fiducialisation of the target volume is one simple solution. This will involve cutting out a central cylinder of reconstructed positions such that $\sqrt{x^2+y^2+z^2} < 59.1$ cm and $\sqrt{x^2+y^2} > 25.0$ cm. Optical fibres have also been positioned in the neck coupled to four 2" PMTs which act as a veto. From preliminary simulations usage of this veto combined with a photoelectron (PE) cut between 100 and 300 PE results in $3.6 \pm 0.13$ region of interest events in 3 years [111], where the error is statistical only. A PE region of 120 to 240 PE reduces this value by 0.5. The proposed fiducial cut reduces the target volume by 11% which is undesirable. Studies to improve position reconstruction algorithms and neck event specific discrimination variables should reduce this cut requirement. The gamma calibration source, described in chapter 4, can produce events within the most problematic region, 0 to 70 cm above the neck-AV interface, in order to measure the rejection efficiency of neck events in situ.

### 2.3.3 $^{39}$Ar

$^{39}$Ar is the most prevalent and pervasive background to the dark matter search in DEAP-3600. It is a $\beta$ emitter with an endpoint energy of 565 keV and half-life of 269 years [73]. With an activity in natural argon of ∼1 Bq/kg, it will produce $\sim 3.4 \times 10^{11}$ electronic recoil events. Approximately $9.8 \times 10^9$ of these will appear in the position region of interest

during the three year run of the experiment [74]. After all cuts 0.04 events are expected in the full region of interest. This value is discussed further in Section 3.2. $^{39}$Ar decay is a unique forbidden transition with a well defined spectrum, shown in Figure 2.19 . As mentioned in chapter 4 this spectrum could be used, in conjunction with external sources, to calibrate the energy scale of the detector [112].

With a light yield of 8 PE/keV$_{ee}$ the PE detection window of 120 to 240PE corresponds to an electronic recoil energy window of 15 to 30 keV$_{ee}$. Thus, only 4% of the $^{39}$Ar spectrum will be detected in the energy region of interest. Given the upper limit of the energy window, simulation of the full $^{39}$Ar spectrum is unnecessary. In the following studies a truncated spectrum from 0 to 120 keV, shown in red in Figure 2.19, was used to simulate $^{39}$Ar. Figure 2.21 shows the reconstructed PE distribution with after-pulses removed. Over the relatively small energy range of the PE window the $^{39}$Ar is approximately flat.

As mentioned above the use of depleted argon can improve sensitivity by allowing the energy threshold to be lowered. Figure 2.20 shows dark matter sensitivity curves for DEAP-3600 with and without the use of depleted argon. Argon which has been depleted by a factor of 100 allows the energy threshold to be lowered from 15 keV$_{ee}$ to 12 keV$_{ee}$ improving sensitivity at 100 GeV by a factor of approximately 4.

## 2.4 Conclusion

DEAP-3600 makes use of liquid argon in its search for dark matter through direct detection. Liquid argon's singlet and triplet time constants give it excellent discrimination between electronic and nuclear recoils through the use of PSD.

The most prominent backgrounds to the dark matter search were described. Further studies are under way to characterise all background rates and distributions in the detector. In particular, modelling the position distribution of surface alphas is of paramount importance as neck events presently cause the largest background in the detector.

In chapter 3 the output variables of the detector will be described. In particular, how

derived variables such as energy, interaction position, and PSD are built from the charge and time of each of the 255 PMTs. The GEANT4 based simulation package, RAT, will be described together with its use in reconstruction and calibration.

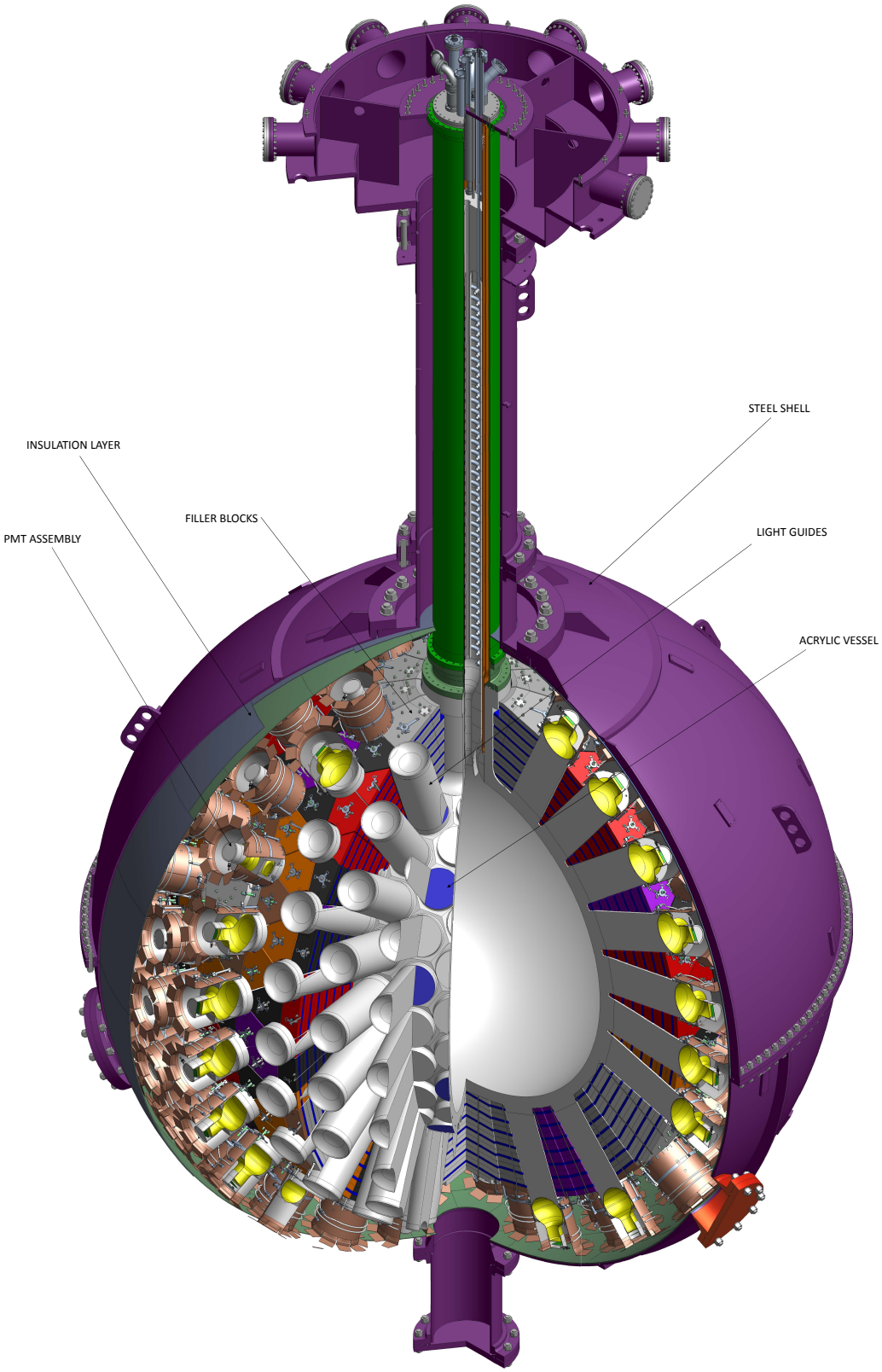


**Figure 2.4:** Rendering of the DEAP-3600 steel vessel with wedge section cut out. Prepared by K. Dering.

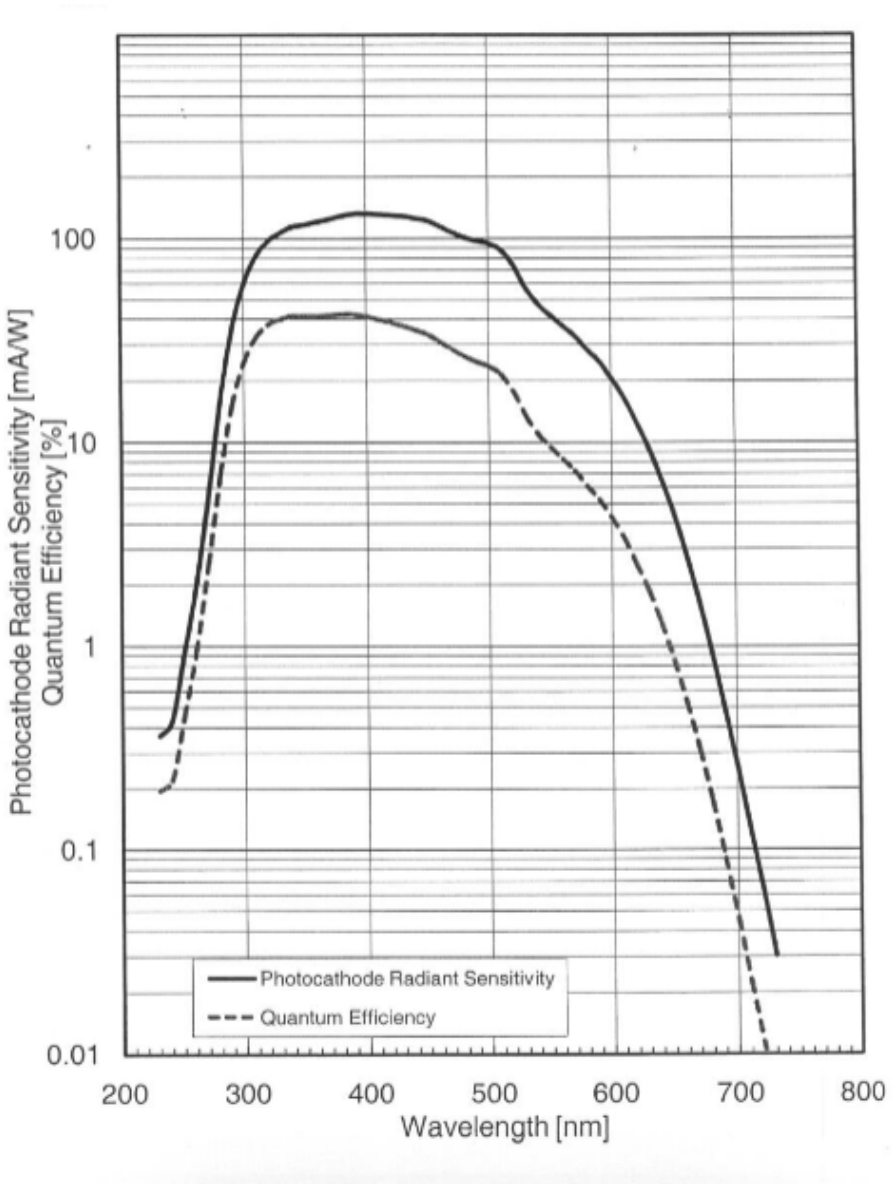


**Figure 2.5:** Spectral response characteristics measured at Hamamatsu for an R5912-HQE PMT. The maximum quantum efficiency is 42.2% at 390 nm wavelength incident light. [97]

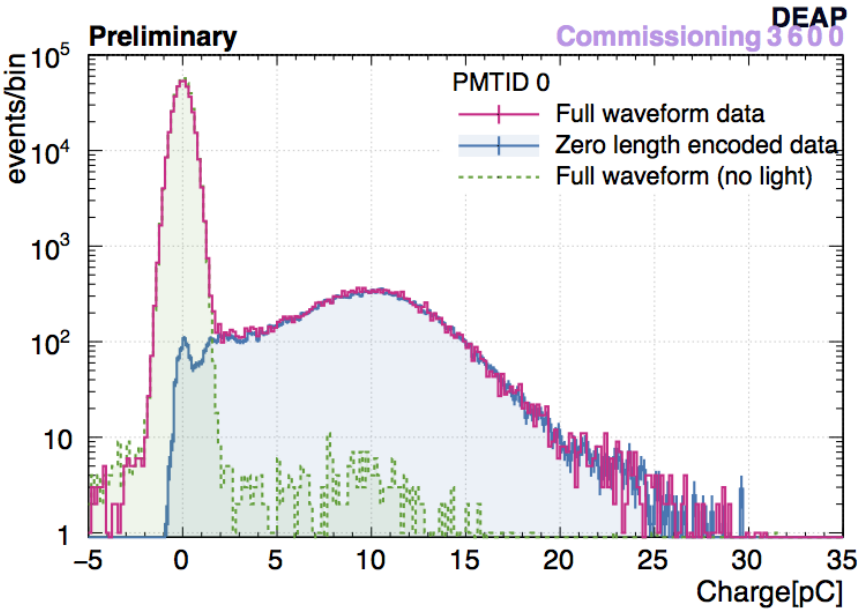


**Figure 2.6:** Single photoelectron charge distribution including the noise pedestal for one of DEAP-3600's internal PMTs. Data was taken during commissioning of the detector using the AARF optical calibration system. Both full waveform and ZLE data (Section 2.2.13) are shown. Full waveform data was taken when the AARF system was not running, confirming the position and size of the pedestal. The mean of the single PE charge is around 10 pC. An analytic form of this charge distribution, used for simulation and reconstruction, will be discussed in chapter 3. Plot prepared by T. Pollmann.

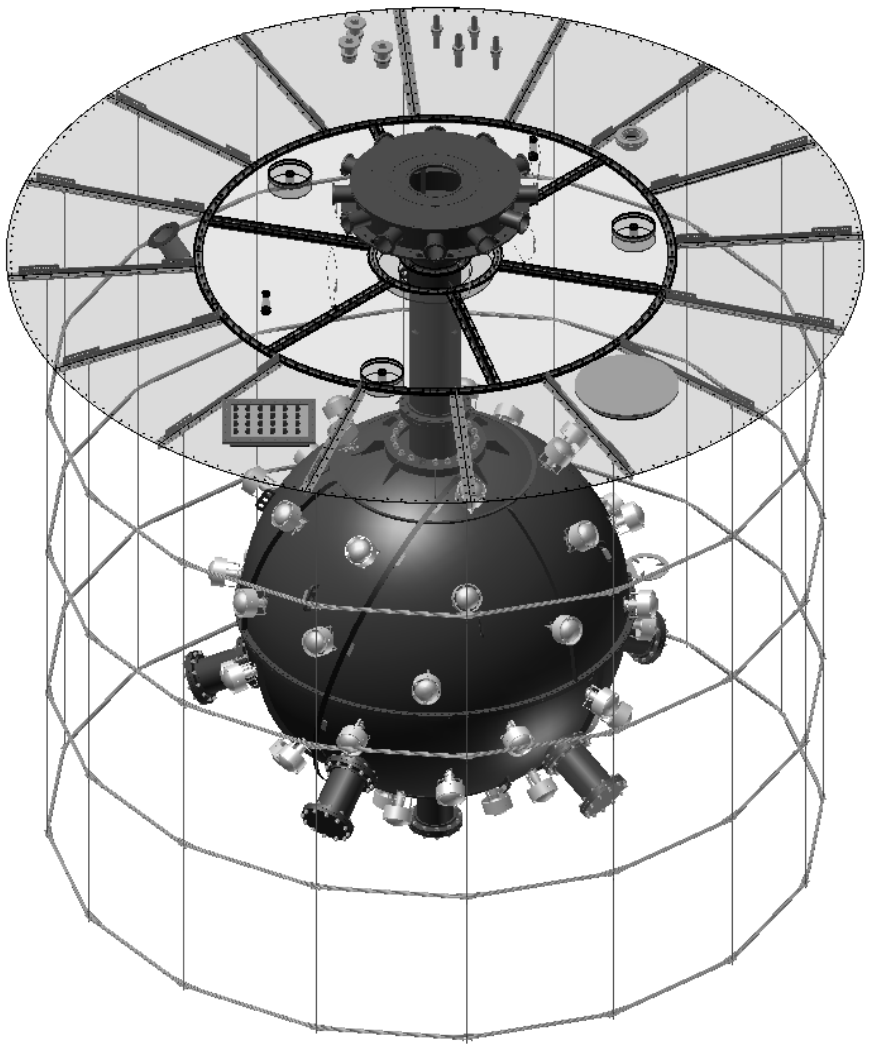

**Figure 2.7:** Rendering of the DEAP-3600 inner vessel with the four surrounding magnetic compensation coils lining the inner wall of the water tank. Two pairs of coils sit symmetrically above and below the steel shell which cancel out the vertical component of the Earth's magnetic field. The field strength, calculated by Radia [99], is shown in Figure 2.8. From [95].

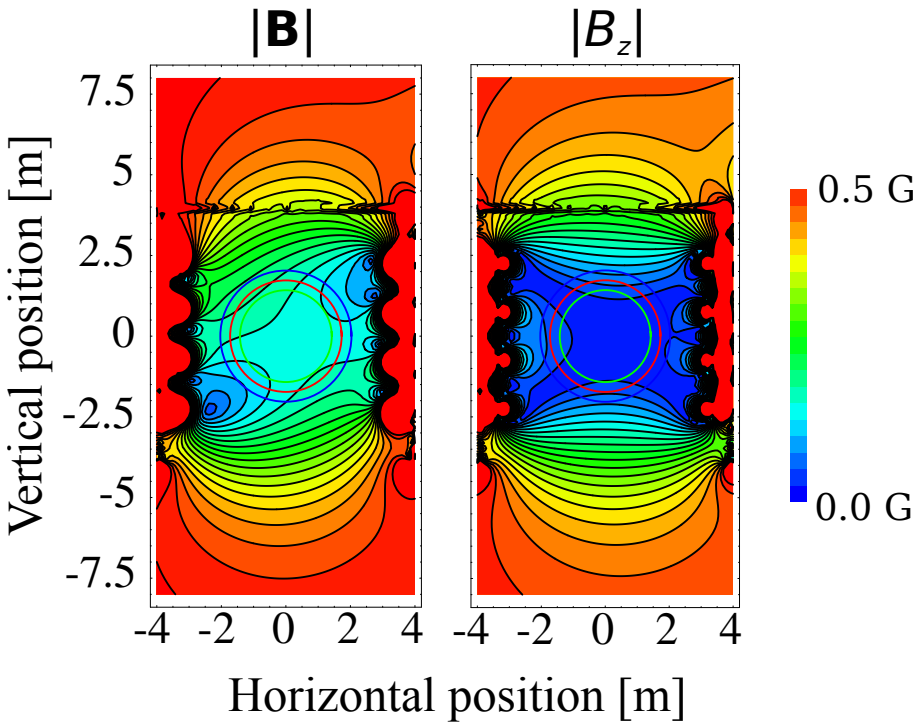


**Figure 2.8:** $|\vec{B}|$ and $|B_z|$ (vertical) field strength created by the magnetic compensation coils surrounding DEAP-3600, on the inner walls of the water tank, calculated by Radia [99]. The three central circles visible on the diagrams correspond to the position of the PMTs (green), the steel shell (red), and the veto PMTs (blue). The ambient magnetic field at the site, taken from a measurement survey at SNOLAB, and the magnetic field created by the compensation coils of the neighbouring experiment MiniCLEAN [101] were both included in the calculation. From [95].

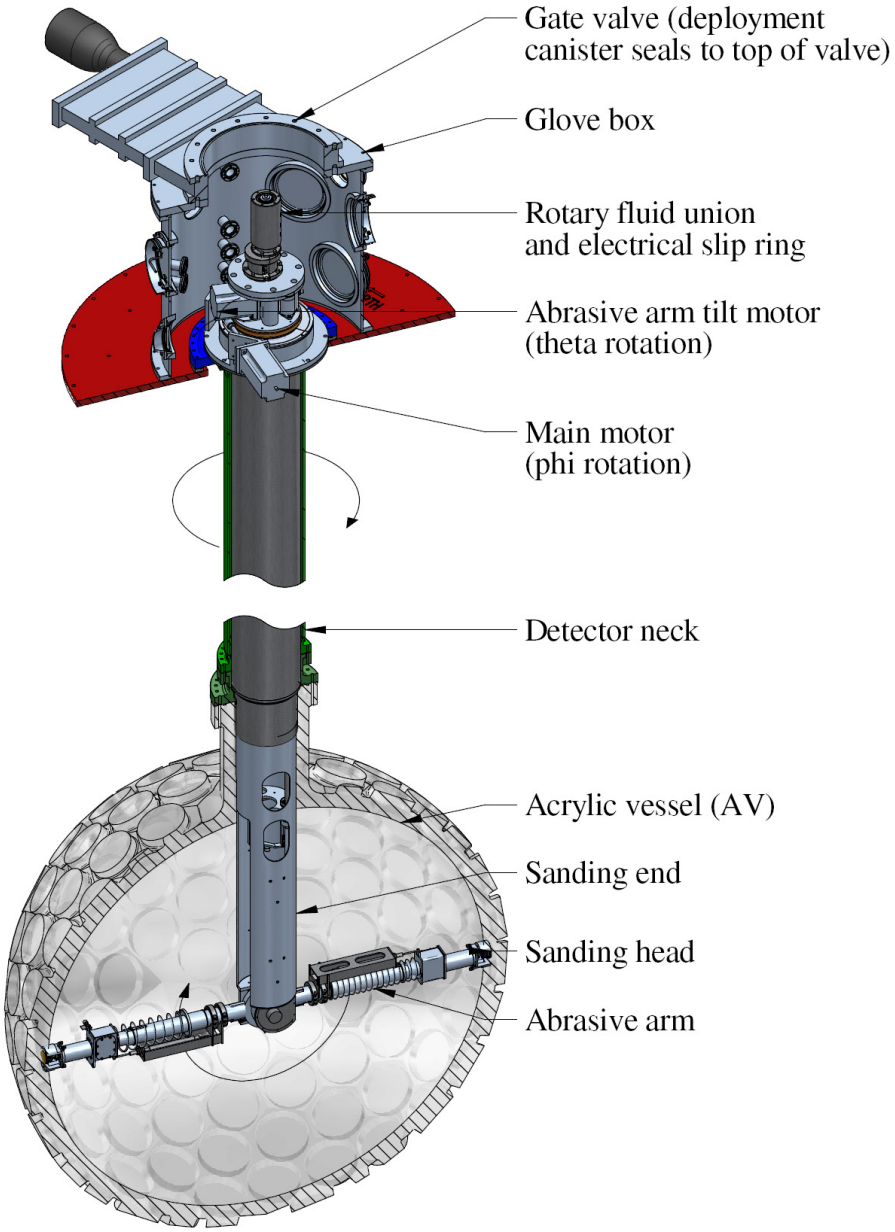


**Figure 2.9:** Overview of the resurfacer system. Sanding heads are able to cover the entire inner surface. From [95].

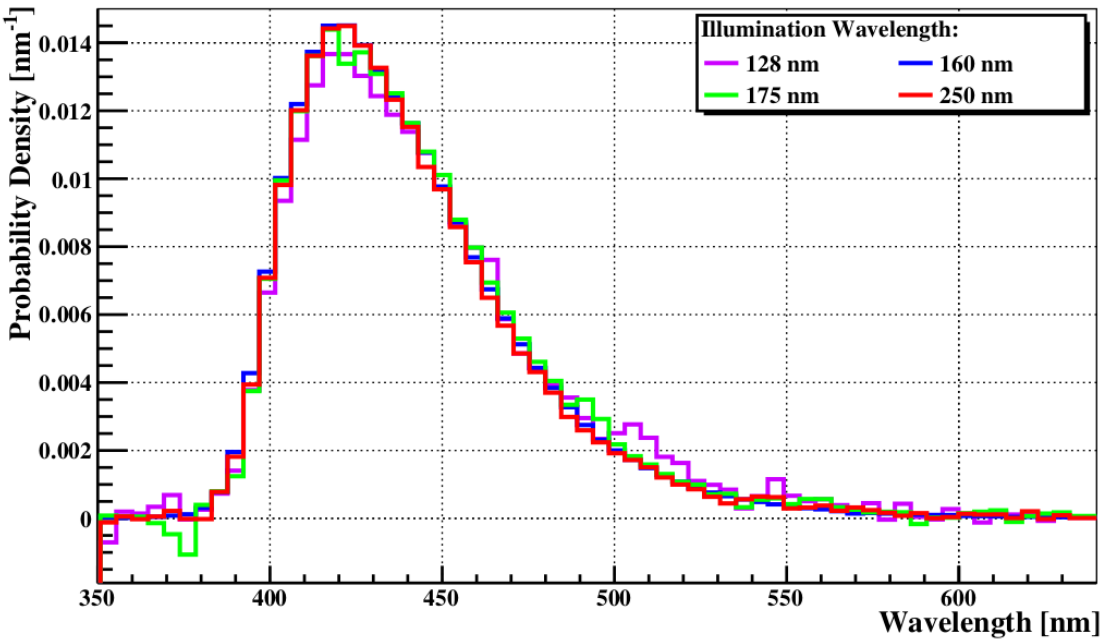


**Figure 2.10:** From [103], the TPB fluorescent re-emission spectrum under illumination of various wavelengths of UV light. Under 128 nm illumination the TPB re-emits with a visible wavelength of 420 nm, close to the peak efficiency of R5912-HQE PMTs.

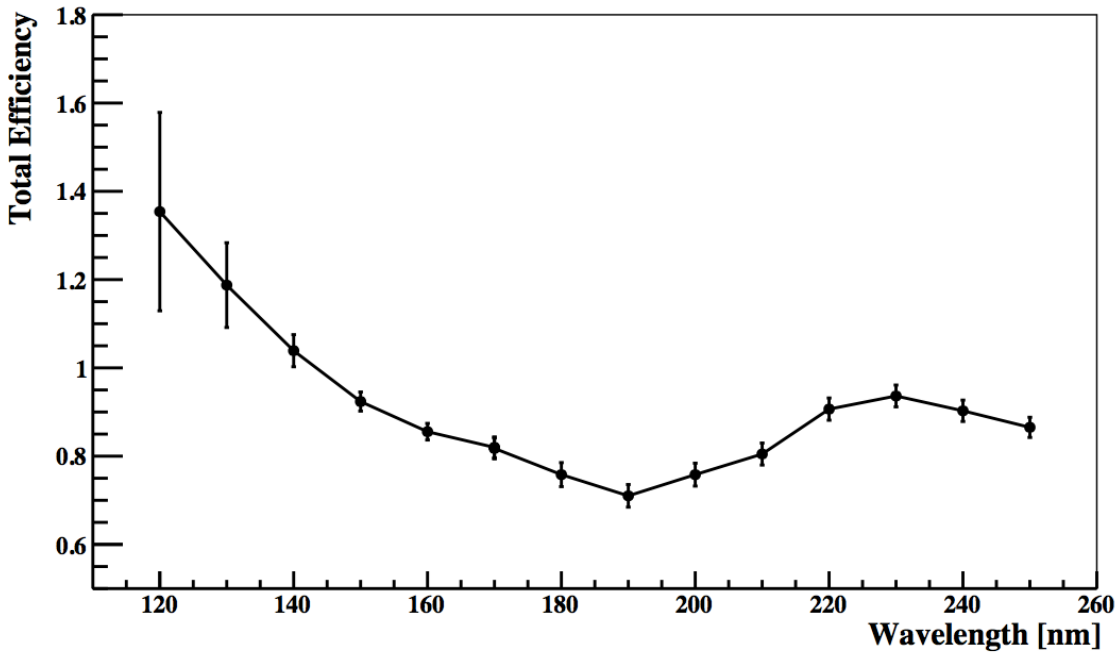


**Figure 2.11:** From [103], the total efficiency, defined as the number of photons emitted over the number of incident photons, vs incident wavelength assuming a Lambertian re-emission distribution.

**Figure 2.12:** The TPB evaporation source. Black filament wrapped around the outside of the sphere is used to heat an inner copper crucible, evaporating the TPB powder contained within it. From [95].

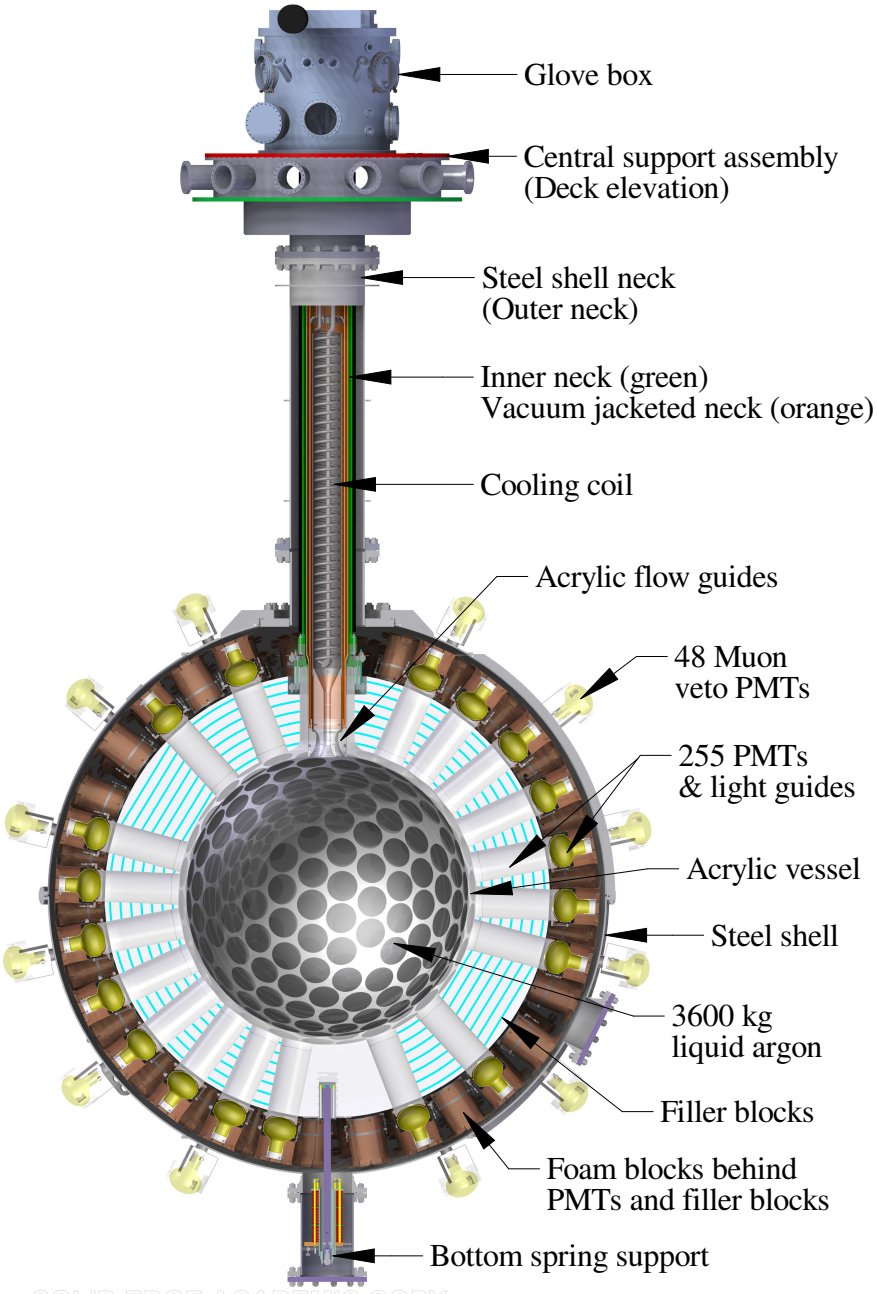


**Figure 2.13:** Cutaway rendering of the DEAP-3600 detector design. The schematic includes the acrylic vessel, light guides, and surrounding filler blocks. The 255 inner and 48 outer veto PMTs are shown along with the steel vessel and neck. Within the neck the cooling coil an be seen along with the acrylic flow guides which regulate the convection of the liquid argon as it is cooled. From [95].

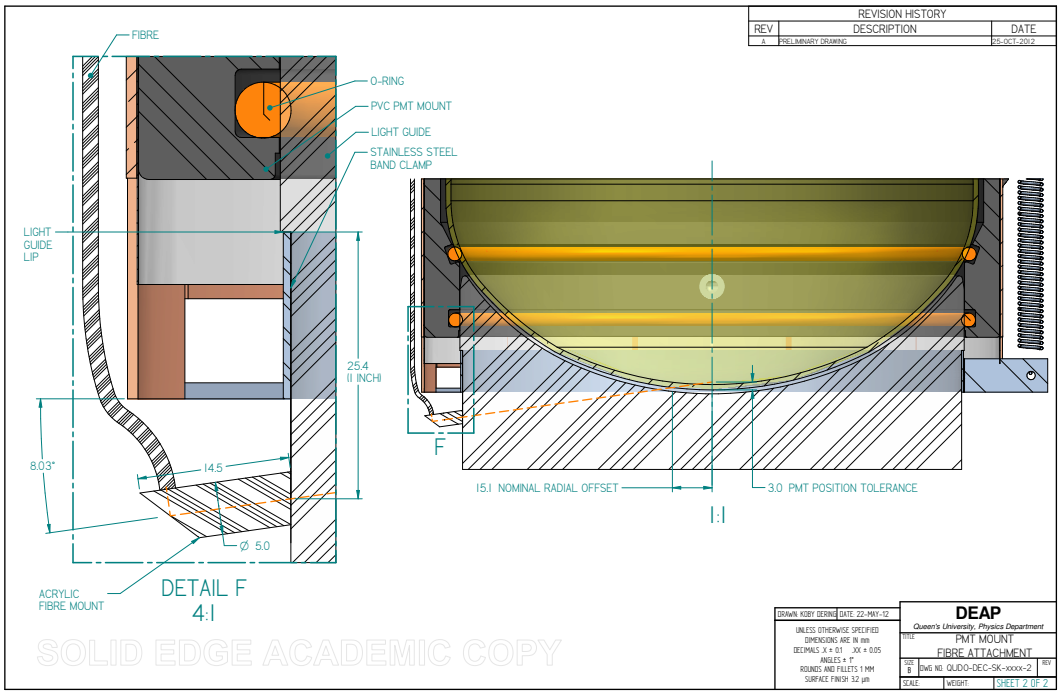


**Figure 2.14:** Schematic of AARF placement for a particular PMT. Optical fibres are attached to twenty small acrylic reflector units placed at the PMT end of the LGs. These AARFs direct the injected light from the edge of the light guide to the centre of the PMT face. Prepared by K. Dering.

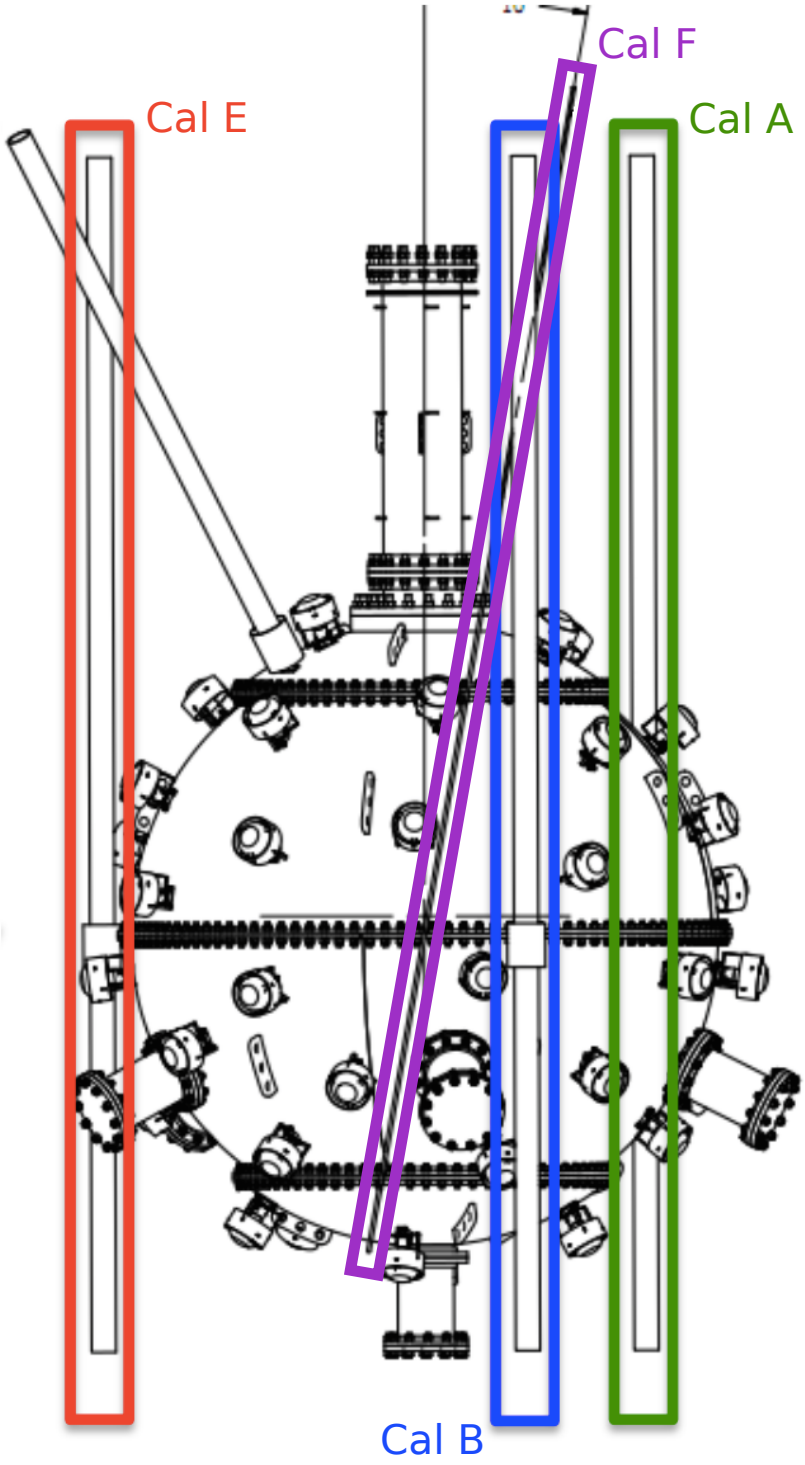


**Figure 2.15:** Schematic showing the positions of the calibration tubes. Cal F runs around the spherical body of the detector, crossing near the neck. The other calibration tubes, Cal A,B and E, are suspended vertically in the water tank. The neutron source can be lowered, from the deck above, with sub millimetre precision down Cal A, Cal B, or Cal E. The gamma source deployment system allows it to move around the Cal F tube. Image courtesy J. Walding.

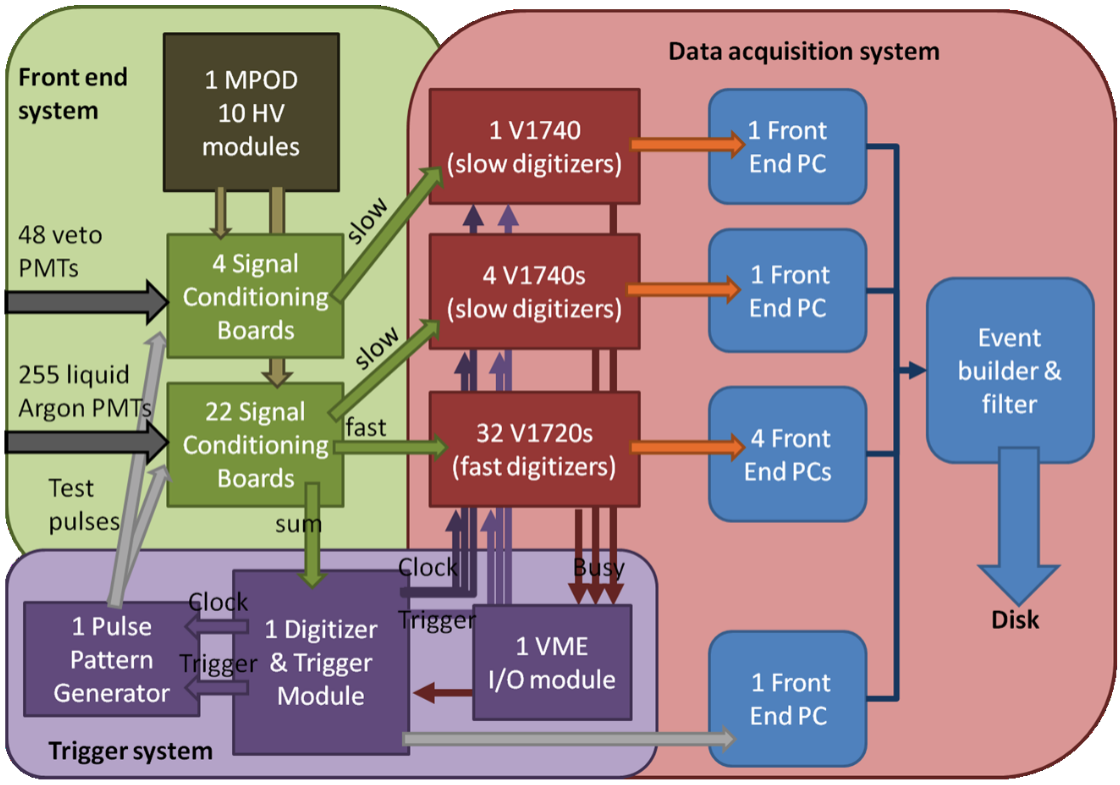


**Figure 2.16:** Schematic of the DEAP-3600 electronics. The PMTs (including those in the veto) are sent through signal conditioning boards to broaden the pulses in time. The pulses are then read by the fast, V1720, and slow, V1740, CAEN digitisers. Each digitised signal is then read by front end PCs. From [95].

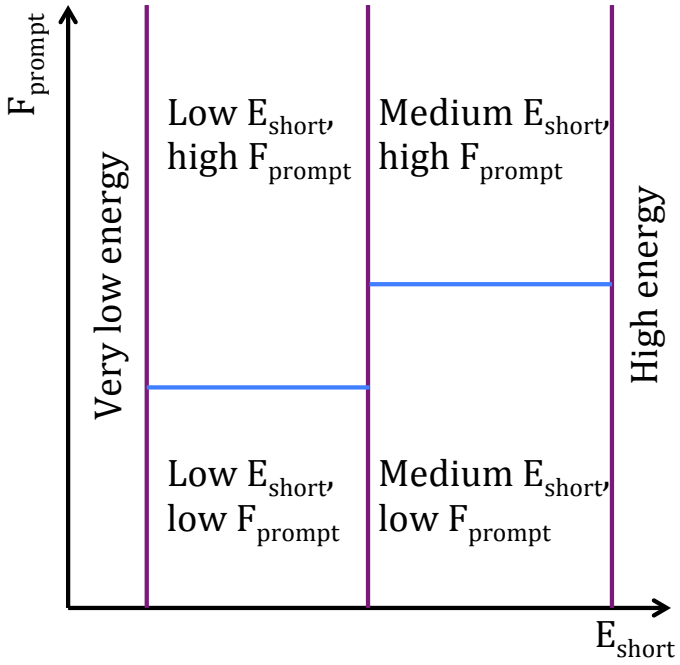


**Figure 2.17:** Physics trigger ($E_{short}$, $F_{\mathrm{prompt}}$) regions which allow for different pre-scaling and read out hardware to be chosen for events in each region. Very low energy events are assumed to be noise and discarded. Medium 50PE $\lesssim \mathrm{E_{short}} \lesssim$ 300PE, high $F_{\mathrm{prompt}} \gtrsim 0.5$ events are all recorded whereas low $F_{\mathrm{prompt}}$ events will be prescaled. There is more overlap in $F_{\mathrm{prompt}}$ in the low energy region so the prescaling requirements differ. The boundary of each region is configurable. From [95].

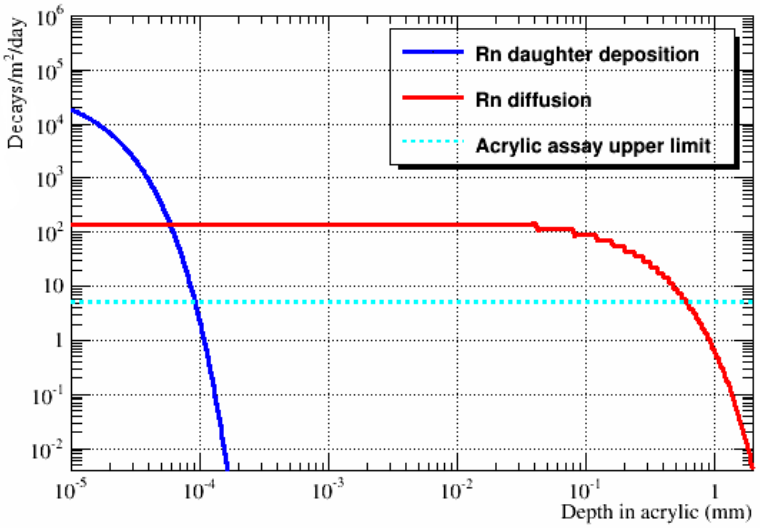


**Figure 2.18:** $^{210}$Pb $\alpha$ activity as a function of depth into the acrylic before resurfacing, after the AV had been exposed to radon-laden air. The blue line shows surface activity from radon daughter deposition, this amounts to $5 \times 10^4$ $\alpha/\mathrm{m}^2/\mathrm{day}$. The red line shows radon diffusion. The cyan line shows the upper limit of $^2$10Pb activity derived from an assay of the acrylic. Removal of ∼0.4 mm leaves the residue activity at $\sim 10\,\alpha/\mathrm{m}^2/\mathrm{day}$. Plot prepared by B. Cai and M. Boulay.

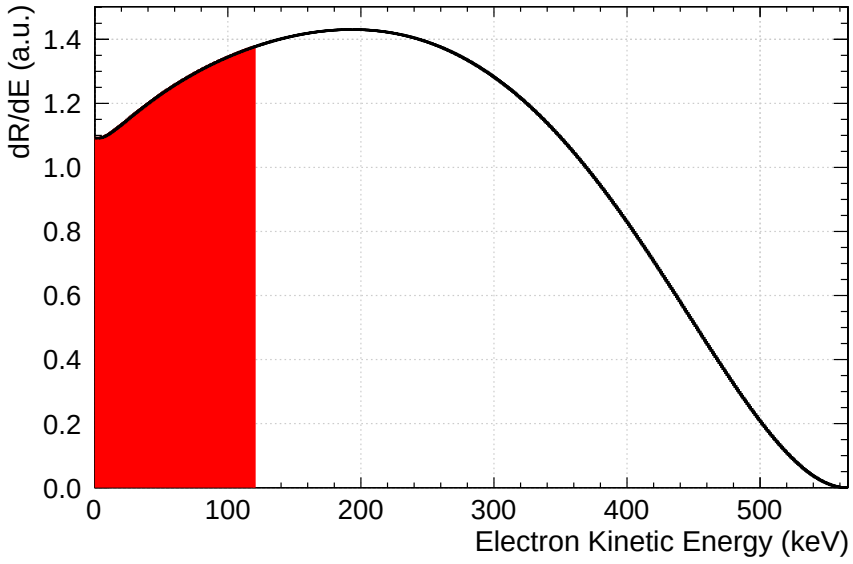


**Figure 2.19:** The $^{39}$Ar decay spectrum. The truncated spectrum from 0 to 120 keV used in simulation is shown in red, this corresponds to 26.4% of the total spectrum. The energy region of interest at 8 PE/keV$_{ee}$ is between $\sim$ 15 to $\sim$ 30 keV.

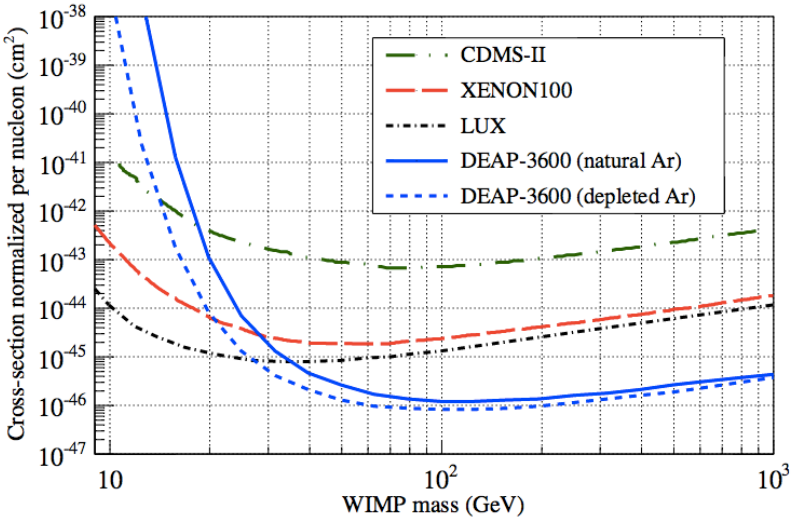


**Figure 2.20:** Dark matter spin-independent WIMP-nucleus scattering cross-section sensitivity of liquid argon, shown alongside LUX, XENON-100, and CDMS-II. Argon which has been depleted by a factor of 100 allows the energy threshold to be lowered from 15 keV$_{ee}$ (solid) to 12 keV$_{ee}$ (dashed). From [113].

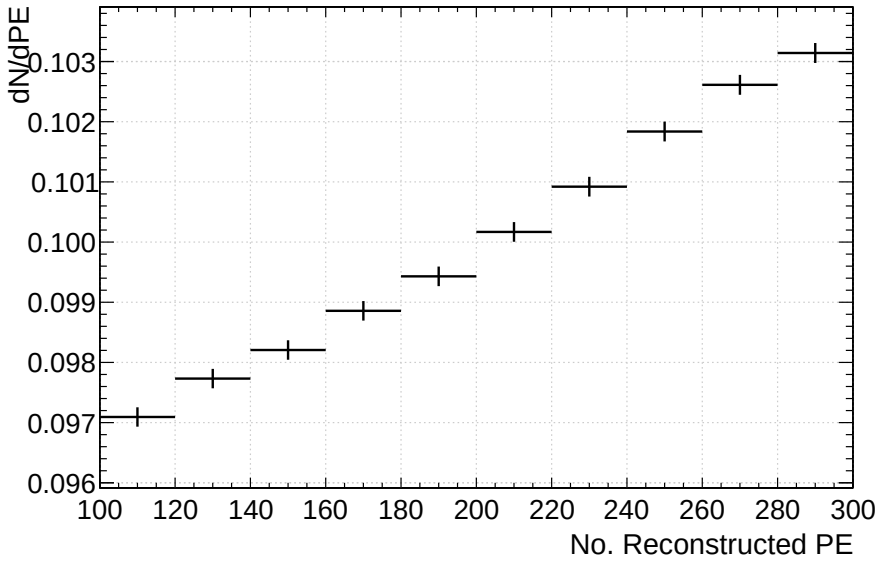


**Figure 2.21:** Distribution of reconstructed PE with after-pulses removed for $^{39}$Ar events with no position reconstruction. The distribution is approximately linear over the relatively small energy window.

# Chapter 3

# Simulation and Reconstruction

*All models are wrong, but some are useful.*

George Box

In this chapter simulation of the DEAP-3600 detector will be discussed. It is performed using the Reactor Analysis Tool (RAT), which propagates the particles through the detector, simulates the DAQ, and carries out higher level analysis. Reconstruction variables used in the experiment will then be discussed including photoelectron (PE) counting, pulse shape discrimination (PSD), and vertex position.

## 3.1 Simulation

RAT [114] is a GEANT4 [115] and ROOT [116] based simulation package originally developed for the Braidwood neutrino experiment [117]. It is designed to perform both the Monte-Carlo (MC) simulation and analysis of liquid scintillator experiments surrounded by PMTs. Particle interaction and propagation through the detector geometry is handled by GEANT4. If a photoelectron is created during simulation the PMT response is handled by the RAT infrastructure. In DEAP-3600 a detailed PMT pulse model has been

implemented including the charge and time characteristics of the various types of PMT pulse. These are described in detail in section 3.1.1. Pulses are then passed to the simulated DAQ. The SCBs, V1720, and V1740 components are all simulated with the SCB response being modelled through FFT convolution. The digitised pulses are then saved in the ROOT Tree format for analysis. A typical simulated event will be approximately 0.5 to 1 MB, this includes all tracking information apart from optical photons.

The analysis portion of RAT does not differentiate between MC generated data and real data. It is comprised of a series of "processors" that analyse individual events. Analysis variables created are added to the same ROOT data structure for each event. An ordered block of processors is run on an event by event basis with each processor potentially using analysis variables created by previous processors. The event by event approach is disadvantageous for calibration data. For this a two phase approach has been chosen where RAT is run over a set of data once to create and apply calibration constants and then again to perform the analysis.

The detector geometry is built using plain text macros of the GEANT4 geometry classes. This allows for ease of creation and modification of the various geometries used. Parts of the GEANT4 detector geometry built in RAT is shown in Figure 3.1. Ray traced images of simulated components are shown along with their corresponding installation photographs. The top shows the light guides attached to the acrylic vessel. The middle shows the filler blocks installed around the light guides and the PMTs mounted. The copper heat shorts which help ensure the PMTs remain above cryogenic temperatures can be seen. The bottom shows the steel vessel and veto PMTs. The water, tank, and surrounding rock of the experiment site are also included in the simulation. Not shown in the ray traced image are the calibration ports. The black Cal F tube can be seen around the centre of the steel vessel.

Similar to the geometry, the physical properties of the materials used in simulation are stored in plain text "ratdb" files. The tables include a combination of literature and test bench values. Liquid argon scintillation is implemented as a separate piece of code

called at the end of each GEANT4 step. The amount of light produced depends on $\Delta E/\Delta x$ which is calculated by GEANT4 once all processes have been executed. Singlet and triplet time constants and prompt fractions for nuclear and electronic recoils are taken from [89]. The liquid argon refractive index as a function of wavelength was taken from [118] and extrapolated. This is required for accurate simulation of Cherenkov radiation. Absorption length in the light guides was obtained from spectrometer analysis of samples of the annealed Spartech acrylic.

The ability of DEAP-3600 to discriminate against electronic recoils is determined by the light yield. Therefore, the accuracy of all parameters related to the optics of the detector are of paramount importance. The TPB is assumed to be uniformly distributed across the inside of the acrylic vessel. This will not be the case in reality, the extent to which the distribution is non-uniform and whether it is within tolerances is currently being determined. During TPB deposition crystalline structures form which may affect the reflection and transmission profile of scintillation light. Scattering in the AV plays a large role with $\sim 30\%$ of photons taking an indirect path to the PMTs. Inaccurate modelling of the scattering/absorption length will result in an under or over estimation of the late light in an event.

### 3.1.1 PMT Simulation

The DEAP-3600 PMTs are simulated in a separate RAT class, with the charge and time characteristics of pulses coming from detailed models. During development a single set of charge and time distribution parameters has been used for all PMTs. Optical calibration data taken during commissioning will allow the implementation of PMT dependent charge parameters.

When a photon strikes a PMT whether a photoelectron is created or not, or whether an early pulse (discussed below) will occur is determined within the simulation tracking. If a PE is created vertex information is passed to the PMT response class. Here, a probabilistic choice is made between the PE causing a standard, late, or double pulse each

of which will have different charge and arrival time characteristics. Further to this, it is determined whether an after-pulse should be created, again with specific time and charge characteristics. Dark hits, through thermionic emission of a PE, are also added external to the simulation with a flat rate per PMT.

The single PE pulse as a function of time is simulated following [119] with the same study being performed on a selection of HQE PMTs. Pulses follow either a double or triple log-normal distribution with the time dependent current given by

$$I(t) = \sum_{i=1}^{n} \frac{Q_i}{t\sqrt{2\pi\sigma_i^2}} \exp\left[ -\ln\left(\frac{t}{\tau_i}\right)^2 / 2\sigma_i^2 \right], \tag{3.1}$$

where $n = 2$ or 3 for double or triple log-normal respectively. For each component, $\tau_i$ is the geometric mean of the electron arrival times, $\sigma_i$ is the geometric root mean square of the arrival times, and $Q_i$ is the total charge. In simulation the $Q_i$ parameters are taken as the relative size of each component with the overall integral size of the pulse being 1. The total charge of the pulse can then be chosen separately. The probability that a PE will form a double or triple log-normal distribution is dependent on the type of pulse.

This total charge of the pulse is drawn from an analytic fit of the single PE charge. Figure 3.2 shows the analytic function along with a preliminary fit to low occupancy data. The model involves a main polya function [120] summed with a low charge secondary polya function and a truncated exponential, this is convolved with a gaussian pedestal. The polya function corresponds to each stage of the dynode chain avalanche being treated as a Poisson process and can effectively be viewed as a compound Poisson distribution. The polya function is given by

$$f_i^{\mathrm{Pol}}(q) = \frac{A_i}{b_i \mu_i \Gamma(\frac{1}{b_i} - 1)} \left(\frac{q}{b_i \mu_i}\right)^{\frac{1}{b_i}-1} \exp\left\{ -\frac{q}{b_i \mu_i} \right\}. \tag{3.2}$$

Here $A_i$ is the relative contribution of the function $i$, $\mu_i$ is the mean and the variance is

given by $\mu_i^2 b$. The full single PE charge distribution is then given by

$$Q_{\mathrm{SPE}}(q) = \begin{cases} \left(\sum_{i=1}^{2} f_i^{\mathrm{Pol}}(q)\right) * \mathcal{N}(q; \mu_{\mathrm{ped}}, \sigma_{\mathrm{ped}}) & \text{if } q \geq \mu_2, \\ \left(\sum_{i=1}^{2} f_i^{\mathrm{Pol}}(q) + B\lambda \exp\{-q\lambda\}\right) * \mathcal{N}(q; \mu_{\mathrm{ped}}, \sigma_{\mathrm{ped}}) & \text{if } 0 < q < \mu_2. \end{cases} \tag{3.3}$$

Here $B$ is the contribution of the exponential truncated between 0 and the mean of the second polya distribution, and $\mathcal{N}$ is a gaussian distribution, representing the pedestal, with mean $\mu_{\mathrm{ped}}$ and standard deviation $\sigma_{\mathrm{ped}}$. When plotting the full model, as in Figure 3.2, the pedestal is added back in with relative contributions, as in $N_{\mathrm{SPE}} Q_{\mathrm{SPE}}(q) + N_{\mathrm{ped}} \mathcal{N}(q)$. The truncated exponential is attributed to double pulsing, discussed below, following [121]. In the following the truncated exponential is not included when simulating single PE charges. The double pulsing charge is handled separately, as in [119]. The single PE charge distribution without the truncated exponential will be referred to as $\widetilde{Q}_{\mathrm{SPE}}$.

Due to the stochastic nature of PMT processes, multiple pulse types are possible each with characteristic arrival times and charge distributions. These pulse types are described below along with their simulation characteristics. The simulation described in the following uses a combination of charges drawn from $\widetilde{Q}_{\mathrm{SPE}}$ and those found following the procedure in [119]. Once a photoelectron has been created in simulation it is assigned a "cathode time". The PE is then handed off to a PMT response class in RAT. This class determines what type of PMT pulse is created, when it is created (assigning an "anode time" to the PE), and its integral charge. Pulse start times used in simulation are shown in Figure 3.3. A summary of PMT pulse types is described below, more information can be found in [98] [121] [122].

### Standard pulses

Standard pulses account for more than 90% of PMT pulses. Shown in black on Figure 3.3 all other pulse times are shown relative to the peak of this distribution. Charges are randomly drawn from the $\widetilde{Q}_{\mathrm{SPE}}$ distribution.

### Early pulses

Early pulses, also called pre-pulses, occur when an incident photon bypasses the photocathode and strikes the first or second dynode directly. The electron avalanche being caused at the first or second dynode results in a smaller amplitude signal at the anode. These pulses also occur earlier relative to standard pulses since there is no transit across the PMT vacuum.

### Late pulses

Late pulses occur when the photoelectron elastically backscatters off the first dynode before striking it again after being re-accelerated by the PMT field. These occur later in time than standard pulses (shown in green in Figure 3.3). The peak of the distribution, 50.52 ns, occurs at twice the mean PMT transit time, 25.26 ns in this case. The charge distribution is assumed to be the same as standard pulses, $\widetilde{Q}_{\mathrm{SPE}}$.

### Double pulses

Double pulses are similar to late pulses. These occur when the photoelectron inelastically scatters off the first dynode. This results in a first pulse on the standard pulse time scale followed by a secondary pulse on the late pulse time scale. During the first scatter electron kinetic energy is lost resulting in a reduced transit distance back into the PMT field. The second, lower than nominal energy, scatter results in a reduced avalanche charge. The single PE charge, drawn from $\widetilde{Q}_{\mathrm{SPE}}$, is thus divided between the two pulses.

### After pulses

After pulses are caused by gases remaining in the vacuum of the PMT being ionised by passing PE. These ions then make their way back to the photocathode where they liberate more PE. This can occur several microseconds later and cause pulses several PE in size.

The probability an after-pulse occurs due to an incident PE, $p_{\mathrm{ap}}$, has been set during development to 0.07. Once an after-pulse has been deemed to occur a second pulse is created drawing from a PE-time joint PDF histogram. Figure 3.4 shows the histogram randomly drawn from in simulation. A pulse is created at the randomly selected time after the incident photoelectron and assigned a certain number of PE, $N_{\mathrm{PE}}$. A charge is then assigned by drawing from the single PE distribution such that

$$Q_{\mathrm{AP}} = \sum_{i=1}^{N_{\mathrm{PE}}} q \sim \widetilde{Q}_{\mathrm{SPE}}. \tag{3.4}$$

**Dark pulses**

Dark pulses, or noise pulses, in the voltage range used by DEAP-3600 are primarily caused by thermionic emission of electrons from the photocathode or dynode stages. These are simulated as a Poisson process with a flat rate in time. The charge distribution is taken to be $\widetilde{Q}_{\mathrm{SPE}}$.

Once pulses have been created for the various pulse types they are passed to the DAQ simulation.

### 3.1.2 DAQ Simulation

The DAQ and trigger simulation in RAT, for DEAP-3600, models the trigger process, the SCB response, the CAEN 1740 digitisers, and the CAEN 1720 digitisers with and without ZLE. It is designed to match the output of the real electronics. This is crucial to the development of reconstruction algorithms, as they can be applied directly to real data through the RAT framework, and systematic effects of the electronics can be modelled.

The CAEN 1720 digitisers have a 4 ns sampling time and are used to read out signal like events. Once digitiser waveforms are created they are stored in ROOT Tree data structures in exactly the same manner as real data.

When a photoelectron is created during a simulation a “true” time distribution is created,

as in Equation 3.1. The pulse time parameter values are stored and a charge is chosen, as described above. These pulses are passed to the trigger simulation. The trigger simulation can be set to either "simple" configuration, with a low threshold using only minimum bias, or "full" configuration, which is close to what will be used in physics running described in chapter 2. The simple configuration is suitable for background studies. The full trigger effect can then be implemented off-line if desired. Once a trigger has been determined the SCB response to these pulses is then modelled using an FFT convolution with an exponential distribution. This broadens the shape of the simulated pulse in time. The broadened pulses are passed to the CAEN digitiser simulation which creates samples and applies noise. ZLE is also applied with the same settings as in the physical CAEN board. Both RAW and ZLE data are saved in the output ROOT Tree. Finally, the simulated data is passed to the event builder, which creates the QT waveforms and determines which physics trigger region the event is in.

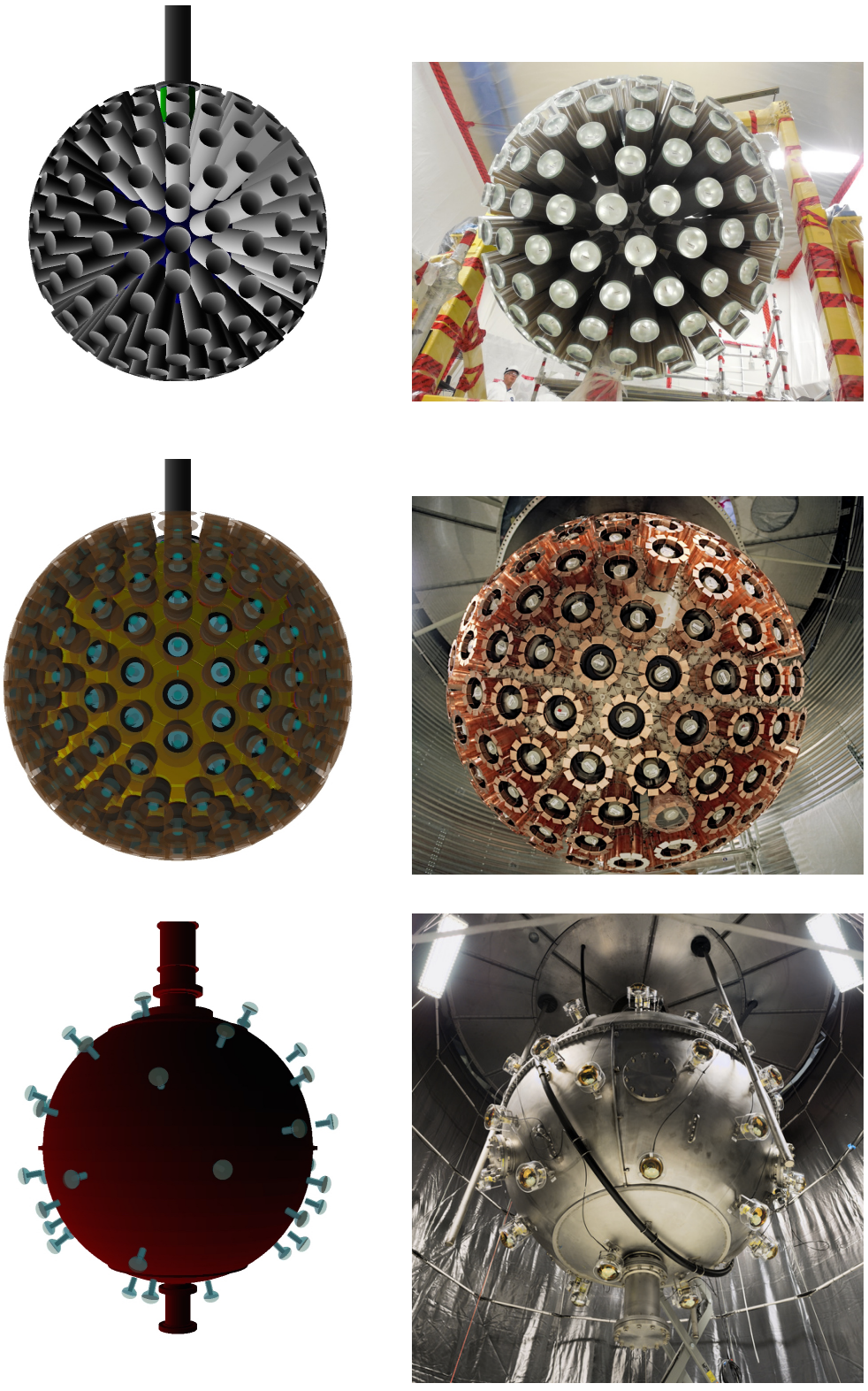

**Figure 3.1:** Ray traced images of components of the DEAP-3600 GEANT4 detector geometry alongside installation photographs. Top: Light guides attached to the acrylic vessel. Middle: Filler blocks and PMTs along with their mounts. Bottom: The steel vessel along with the veto PMTs. The water, tank, and surrounding rock of the experiment site are also included in the simulation.

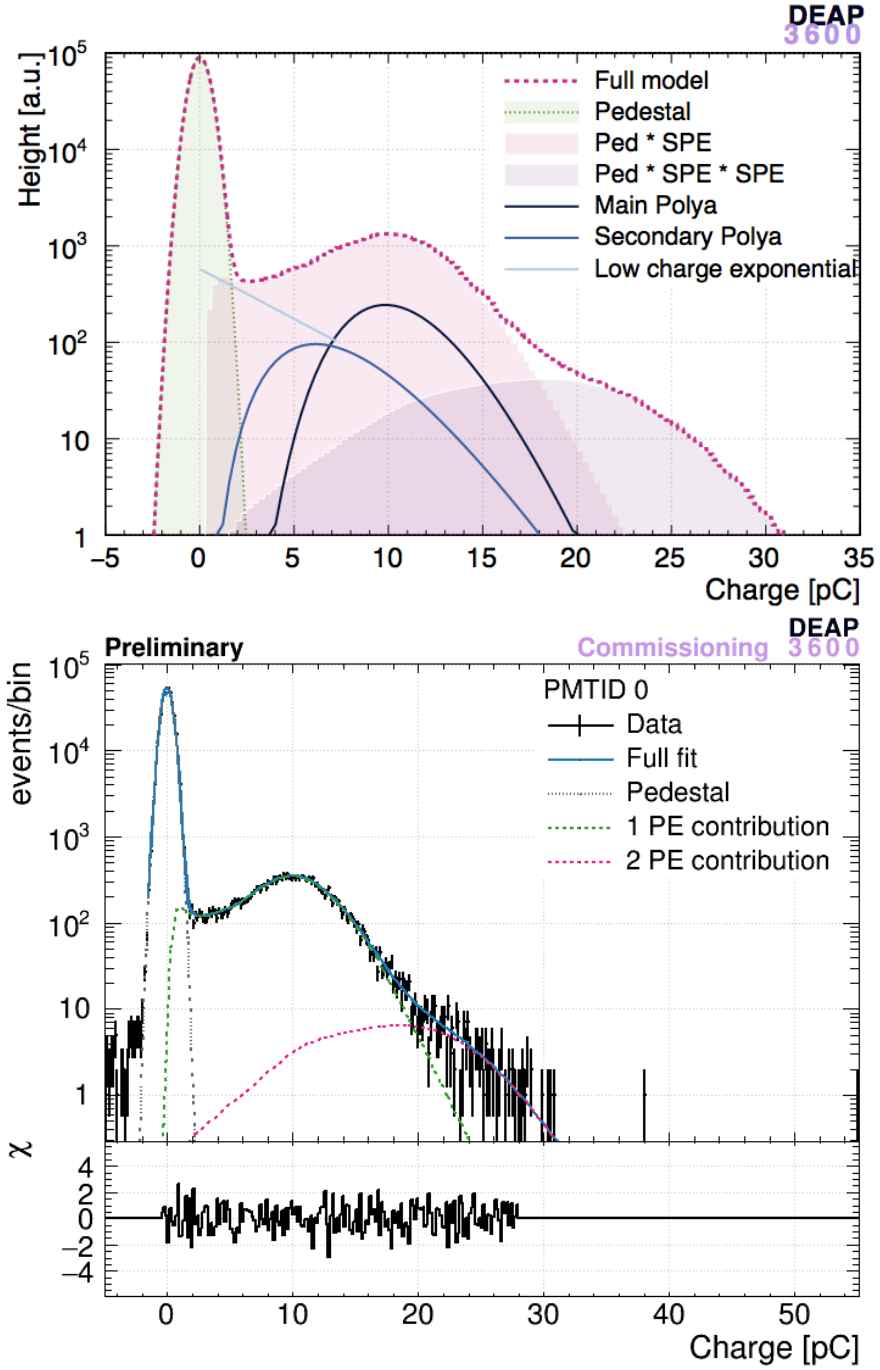


**Figure 3.2:** Single PE charge model used in simulation. Top: Model which involves the sum of two polya functions and a truncated exponential, this is convolved with a gaussian pedestal. Bottom: Fit to optical low occupancy AARF calibration data during commissioning. The 2 PE contribution due to leakage is modelled by convolving the single PE distribution with itself.

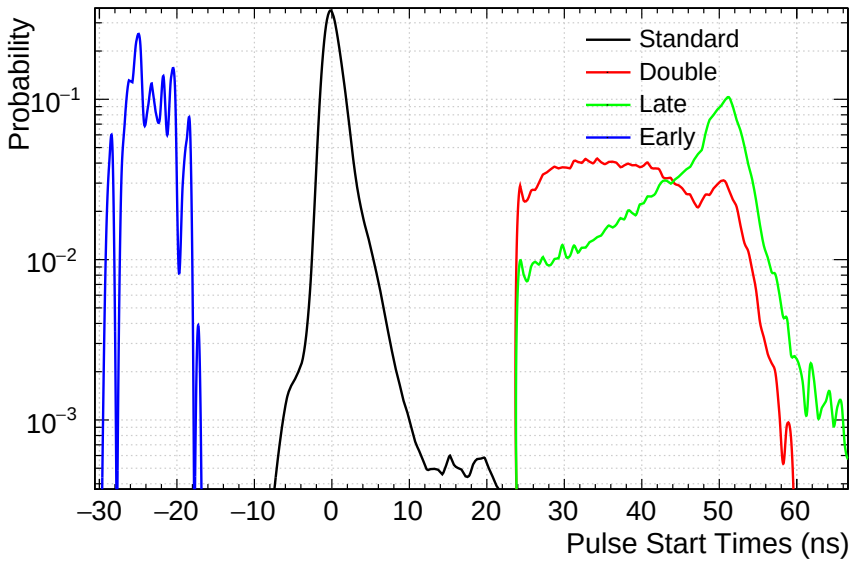


**Figure 3.3:** Start times for pulse types simulated for the R5912-HQE tubes in RAT, each individually normalised to unity. The overall probability of seeing a standard pulse is 0.912, a double pulse is 0.055, and a late pulse is 0.033. Early pulses must be treated separately as it is affected by the geometry and optical properties of the PMT. A value of 0.012 corresponds to the probability of a photon at normal incidence on the centre of the PMT face transmitting through the photocathode and creating a photoelectron on the first dynode.

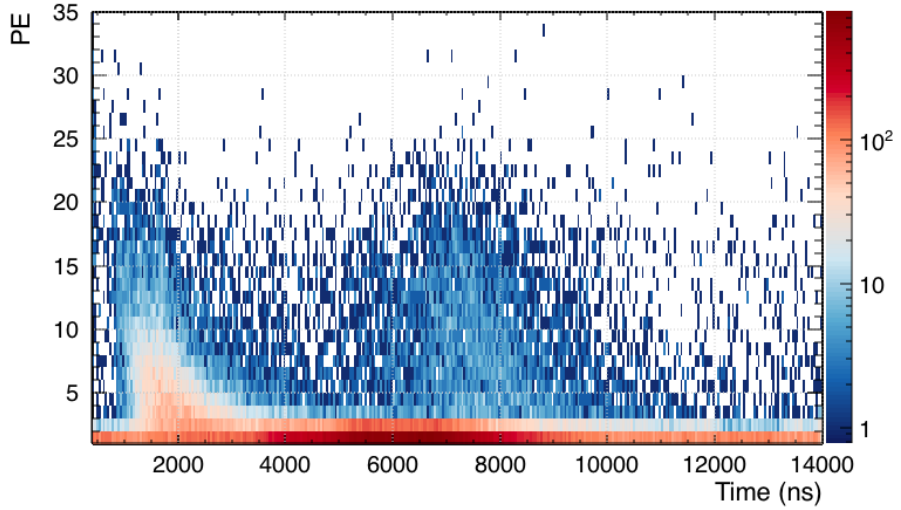


**Figure 3.4:** Plot of the after-pulse PE versus time from initial pulse used during development. When an initial PE is deemed to have caused an after-pulse this histogram is randomly drawn from and a second pulse is created. The size of the pulse is determined by Equation 3.4.

## 3.2 Reconstruction

Reconstruction involves determining the interaction energy, position, and particle type for each triggered event. For all of these the number of PE produced in each PMT per event needs to be accurately determined. A statistical technique for doing this, involving the known scintillation timing PDF created using the $F_{\text{prompt}}$ variable, is described in section (3.2.1). The energy of interactions is determined using the light yield which is presently $9.8 \pm 0.5$ PE/keV$_{\text{ee}}$ in simulation. Higher than the design specification. However, this value includes after-pulsing in the PMTs. Upon removal of the after-pulses using the procedure described below the light yield becomes 9.3 PE/keV$_{\text{ee}}$. With the present optical parameters, a uniform distribution of TPB along with no variation between the light guides, there is no position variation to the light yield dependence. The energy of the interaction affects the variance of the light yield with $9.3 \pm 1$ PE/keV$_{\text{ee}}$ at 10 keV$_{\text{ee}}$, and $9.3 \pm 0.7$PE/keV$_{\text{ee}}$ at 30 keV$_{\text{ee}}$. Calibration using $^{39}$Ar and external radioactive sources will determine the energy scale of real data. The energy region of interest ("ROI") is set by $F_{\text{prompt}}$'s ability to discriminate against the $^{39}$Ar background. As stated above, extrapolated from the DEAP-1 model the nominal PE region of interest is $120 < \text{PE} < 240$. This corresponds to an energy window between 12.9 keV$_{\text{ee}}$ (51.6 keV$_{\text{r}}$) and 25.8 keV$_{\text{ee}}$ (103 keV$_{\text{r}}$). Use of more powerful PSD variables will allow the energy threshold to be lowered, this results in significant gains in rate for the standard WIMP spectrum. Position reconstruction algorithms, described in section 3.2.3, must have excellent resolution near the edge of the target volume with limited leakage from the surface into the position ROI. The preliminary position ROI is set to 55 cm giving a fiducial mass of 1000 kg of liquid argon.

$F_{\text{prompt}}$

The $F_{\text{prompt}}$ variable, described in the previous chapter, is used as the basic PSD particle identification variable as well as in higher level analysis such as photoelectron counting,

described later. Shown again here, we have

$$F_{\text{prompt}} = \frac{\int_{t_0}^{t_{\text{p}}} Q(t)dt}{\int_{t_0}^{t_{\text{end}}} Q(t)dt}. \tag{3.5}$$

For analysis development in the DEAP-3600 experiment $t_0$ was chosen to be -28.0 ns, $t_{\text{p}}$ to be 150 ns, and $t_{\text{end}}$ to be 10 $\mu$s. The peak of the waveform is set as t=0 ns. This window was chosen in the DEAP-1 experiment to maximise the separation of electronic and nuclear recoil distributions and has yet to be optimised for the DEAP-3600 experiment. Figure 3.5 shows $F_{\text{prompt}}$ versus the number of reconstructed PE for simulated $^{39}$Ar events. The median, PE dependent, $F_{\text{prompt}}$ value for nuclear recoils is shown as a red line. The high $F_{\text{prompt}}$ events near the region of interest are due to after-pulsing. After-pulses also push the median value of $F_{\text{prompt}}$, which was expected to asymptote to 0.7 at high energy, to a lower value.

$3.4\times10^{11}$ $^{39}$Ar events are expected across the whole detector, with 2.8% of these appearing inside the energy and position ROI. For studies in this text a data set of $2.54 \times 10^7$ low energy $^{39}$Ar events was simulated. This corresponds to $9.52 \times 10^7$ full spectrum events, 3600 times less than expected with a 3 year exposure. With increased statistics the region of interest will begin to be populated with $^{39}$Ar events due to after-pulsing in the PMTs. Identification and removal of after-pulses is, therefore, of paramount importance. A procedure to do this is discussed in detail below along with its effect on PSD. Leakage values were calculated using the analytic model for $F_{\text{prompt}}$ set out in 2.2. At 50% WIMP acceptance this corresponds to 14.25 events in 3 years, an unacceptably high number. Without after-pulsing removal the $F_{\text{prompt}}$ region of interest was chosen to keep $^{39}$Ar leakage below the nominal 0.2 events. A value $F_{\text{prompt}} > 0.7$ was chosen corresponding to 0.04 events in 3 years of running. Through the use of more powerful PSD, described below, and the removal of after-pulses the 120 PE threshold could potentially be lowered.

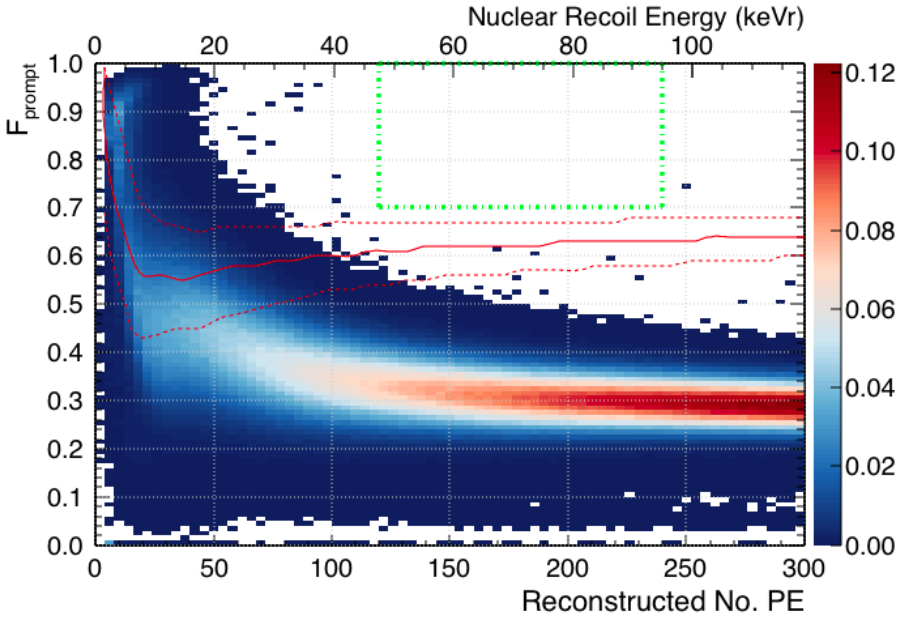


**Figure 3.5:** $F_{\text{prompt}}$ versus the number of reconstructed PE for simulated $^{39}$Ar events distributed throughout the target volume. The median, PE dependent, $F_{\text{prompt}}$ value for nuclear recoils is shown as a red line, with the dashed lines showing 68% of the distribution. The green dash-dot line represents the nominal region of interest. $2.54 \times 10^7$ low energy $^{39}$Ar events were simulated corresponding to $9.52 \times 10^7$ full spectrum events, 3600 times less than the 3 year exposure. The high $F_{\text{prompt}}$ events near the region of interest are due to events with after-pulses. An algorithm to remove these is detailed below.

### 3.2.1 Photoelectron Counting

Photoelectron counting in DEAP-3600 currently involves a statistical method described in detail in [123]. This approach relies on a separate pulse finding algorithm which determines the position and temporal extent of each PMT pulse. Here, and in the following, "pulse" refers to the signal read out by the digitizer rather than the PMT charge response to a photoelectron. That is, each pulse may contain multiple overlapping PE signals. Pulse finding requires identifying deviations from the digitiser baseline which are a result of photoelectron signals. The PE finding method then makes use of a scintillation timing PDF, built from the known singlet and triplet time constants, to determine the most likely number of PEs in each pulse. This timing PDF is built using MC simulation where photons with the liquid argon scintillation wavelength are generated throughout the target volume with the given time constants. Figures (3.6) and (3.7) show the result of these simulations for $\tau_{\text{s}} = 7$ ns and $\tau_{\text{t}} = 1450$ ns respectively. In Figure 3.6 structure due to the PMT response can be seen, with the shoulder at 40 ns being due to double pulsing.

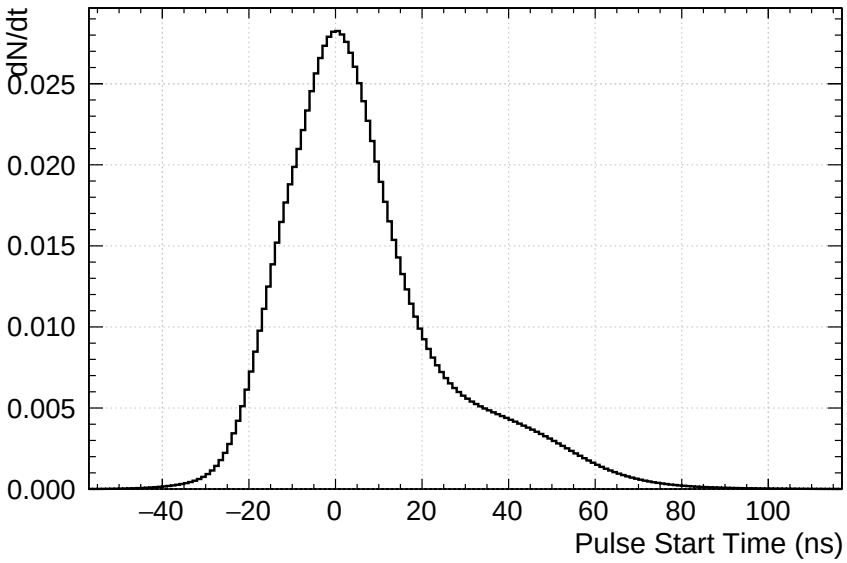


**Figure 3.6:** Arrival time of photons generated using the singlet time distribution with $\tau = 7$ ns. Here photons from double pulsing are included which can be seen in the shoulder at around 40 ns.

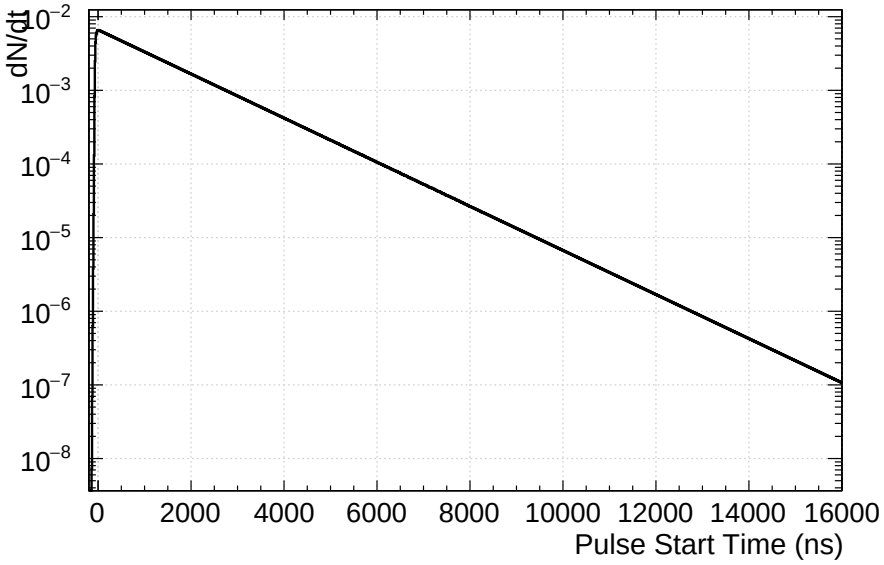


**Figure 3.7:** Arrival time of the photons generated using the triplet time distribution with $\tau = 1450$ ns.

The pulse finding algorithm used by DEAP-3600 involves finding numerical derivatives of the waveform (the full digitiser read out for the event in each PMT). Figure 3.8 shows an example waveform and where the pulse finding algorithm attributed start and end times to pulses. The start of a pulse is set at 3 samples before the derivative $(V_{i+1} - V_i)$ crosses a threshold $V_{\text{deriv}}$. The pulse is ended when the voltage drops below a certain value $V_{\text{end}}$.

If the waveform is below a higher voltage threshold $V_{\text{stop}}$ and the derivative threshold is crossed a second pulse is created. This is the case in the example waveform shown. Currently only the integral size of the pulse and its start and end times are used in PE counting. Work involving the use of the waveform shape in PE counting is ongoing.

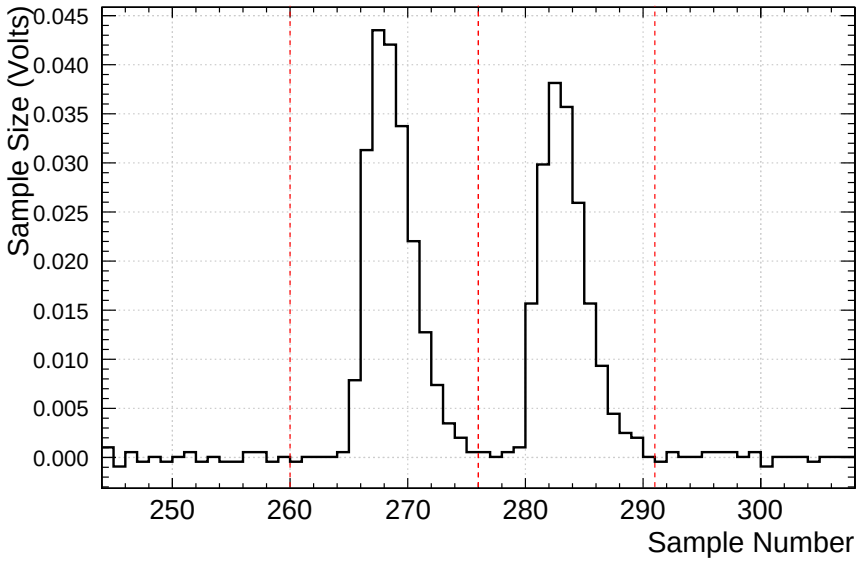


**Figure 3.8:** An example of where the pulse finding algorithm places the beginning and end of a pulse. Here two single PE pulses from one PMT in a single event are identified. Vertical dashed lines show the pulse regions. The algorithm sets the start of a pulse as 3 samples before the derivative crosses a threshold value. The pulse is ended when the voltage drops below a certain value $V_{\text{end}}$. If the waveform is below a higher voltage threshold $V_{\text{stop}}$ and the derivative threshold is crossed a second pulse is created. This is the case in the example waveform shown.

Once pulses have been identified they are passed to the PE counting algorithm. Using Bayes' theorem a probability is assigned to the number of PE each pulse may contain in the following way:

$$\begin{aligned} P_{\text{N}}(n|q,t_1,t_2,F_{\text{prompt}}) &= \frac{P_{\text{Q}}(q|n)P_{\text{N}}(n|t_1,t_2,F_{\text{prompt}})}{P_{\text{Q}}(q|t_1,t_2,F_{\text{prompt}})} \\ &= \frac{P_{\text{Q}}(q|n)P_{\text{N}}(n|t_1,t_2,F_{\text{prompt}})}{\sum_{i=0}^{\infty} P_{\text{Q}}(q|i)P_{\text{N}}(i|t_1,t_2,F_{\text{prompt}})}. \end{aligned} \tag{3.6}$$

Here $P_{\text{N}}(n|q,t_1,t_2,F_{\text{prompt}})$ is the probability that a pulse contains $n$ PE given an integral charge $q$ and start and end times $t_1$ and $t_2$ respectively. $P_{\text{Q}}(q|n)$ is the probability of seeing a charge $q$ given a number of PE $n$. Finally, $P_{\text{N}}(n|t_1,t_2,F_{\text{prompt}})$ is the probability

of finding $n$ PE between time $t_1$ and $t_2$ given an expected timing distribution built using the value of $F_{\text{prompt}}$ for the event. Here

$$P_{\text{N}}(n|t_1, t_2, F_{\text{prompt}}) = \sum_{j=0}^{\infty} \text{Pois}(j|\mu) \times \text{Bin}(n|j, I(t_{n,1}, t_{n,2}, F_{\text{prompt}})), \tag{3.7}$$

where $\text{Pois}(j|\mu)$ is the Poisson probability of seeing $j$ photons in the PMT given an expected number of PE, $\mu$. This expected number is initially calculated through charge division of the total charge seen in the PMT. This is multiplied by the binomial probability, $\text{Bin}(n|j, I(t_{n,1}, t_{n,2}, F_{\text{prompt}}))$, of seeing $n$ of those total $j$ photons in the time interval $t_{n,1}$ to $t_{n,2}$ given the expected time distribution $I$.

The expected PE time distribution is given by

$$I(t_{n,1}, t_{n,2}, F_{\text{prompt}})) = \int_{t_{n,1}}^{t_{n,2}} [F_{\text{prompt}}(1 - f_{\text{d}})S(t) + (1 - F_{\text{prompt}})(1 - f_{\text{d}})T(t)]\, dt + f_{\text{d}}. \tag{3.8}$$

Here $S(t)$ and $T(t)$ are the singlet (Figure 3.6) and triplet (Figure 3.7) lifetime state PDFs respectively. $F_{\text{prompt}}$, discussed above, gives a measure of the distribution of singlet and triplet states in the event so $S(t)$ and $T(t)$ can be weighted appropriately. A pulse appearing late in an event, for example, will be assigned a lower probability for high $n$ PE hypotheses for an electronic recoil (low $F_{\text{prompt}}$) like event than for a nuclear recoil (high $F_{\text{prompt}}$) like event. $f_{\text{d}}$ is the fraction of photons due to the measured dark rate, assumed to be uniformly distributed in time. This, again, is calculated by dividing the expected number of dark hits by $\mu$. The time interval bounds $t_{n,1}$ to $t_{n,2}$ are dependent on the number of hypothesised PE. A cumulative distribution function of the timing PDF is created and divided up into $(n + 1)$ quantiles with the first, $q_1$, and $n$th, $q_n$ being determined. Times are then assigned by taking $t_{n,1} = q_1 - \tau/2$ and $t_{n,2} = q_n + \tau/2$ where $\tau$ represents the sampling time. This method is used to estimate the integration window in lieu of exact knowledge of the PMT pulse shape. Numerical derivative methods currently being developed for PE counting, mentioned above, could potentially be used to determine these time intervals along with better estimates of $\mu$, for example.

$P_{\mathrm{Q}}(q|n)$ is built by convolving the single PE charge PDF with itself $n$ times, i.e. $P_{\mathrm{Q}}(q|n) = (\widetilde{Q}_{\mathrm{SPE}})^{*n}$. Figure 3.9 shows the first few of these multiple charge distributions, with the maximum being 50 PE. Beyond this the ability to discriminate between PE is poor due to the increasing overlap of the distributions. As such, the number of PE can be determined to comparative accuracy but more quickly using charge division (dividing the total charge by the mean single PE charge $|\widetilde{Q}_{\mathrm{SPE}}|$).

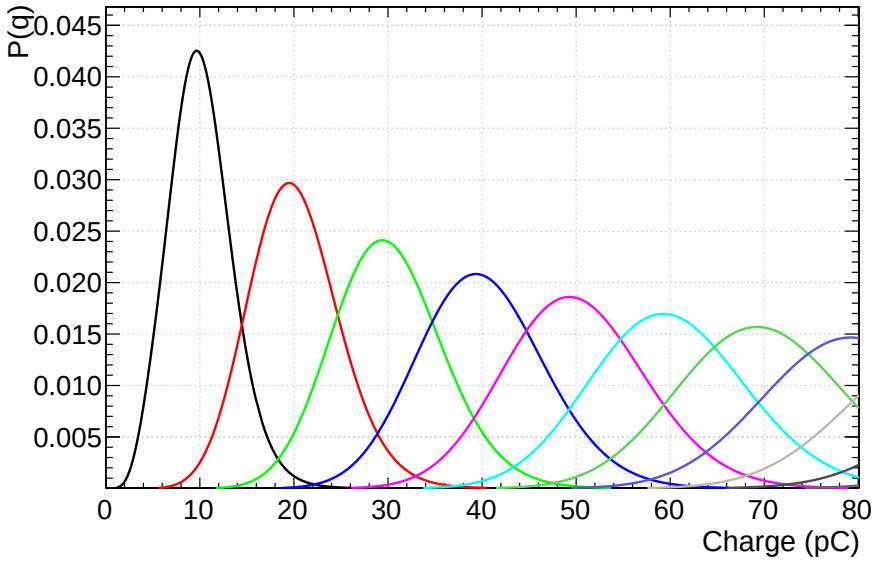


**Figure 3.9:** Charge distributions for multiple PE. These are built by convolving the single PE charge distribution (black) with itself $n$ times.

The number of PE in each pulse is calculated by finding the $n$ which maximises Equation 3.6 through a simple grid search. It is assumed that every pulse identified by the pulse finder contains at least one PE. This gives a minimum bound to $n$ of 1. This provides an advantage when dealing with early pulses. The fractional charge of an early pulse, which would be underestimated by simple charge division, is identified as 1 PE. The maximum is set to be the estimated number of PE in the pulse plus five times the Poisson error. Like $\mu$, this is calculated through charge division where the integral charge of the pulse, $q$, is divided by $\widetilde{Q}_{SPE}$. So the maximum $n$ is given by

$$n_{\mathrm{max}} = \mathrm{ceil}\left(\frac{q}{|\widetilde{Q}_{\mathrm{SPE}}|} + \sqrt{\frac{q}{|\widetilde{Q}_{\mathrm{SPE}}|}}\right). \tag{3.9}$$

As discussed above, if a pulse is found to have $n_{\max}$ greater than 50 PE, charge division is used to the determine the number of PE in the pulse.

Once the most probable number of PE is determined times are assigned to each one. In a similar fashion to the timing integral limits, a CDF is created of the waveform charge over time. This is divided into $(n+1)$ quantiles and PE time is assigned to each of these i.e. a time is assigned once the charge over time reaches some $1/(n+1)$ fraction of the total charge in the pulse. Interpolation of the CDF allows for quantiles to lie between digitiser samples.

This approach does not take after-pulsing into account. The timing PDFs assume only scintillation photons and dark hits cause PE. This means pulses occurring later in the waveform from the singlet peak are preferentially chosen to be 1 PE. After-pulses, which cause multiple PE pulses to occur later in waveform, cause an under-counting bias with increasing PE. This is illustrated in Figure 3.10 which shows the number of reconstructed PE versus true PE for $^{39}$Ar events, normalised to the number of events per true PE bin. The simulated events are distributed centrally, within a radius of 55 cm of the centre of the target volume, to minimise geometrical effects. A green line is drawn along the reconstructed PE equals true PE line to highlight the under-counting bias. Pulses arriving late in the event are more likely to be identified as single PE rather than multi PE. This results in the number of PE in large after-pulses being under estimated. Figure 3.11 shows a straight line fit to Figure 3.10. The slope of $0.909 \pm 0.003$ agrees with what is expected from miscounting after-pulses. A dummy MC simulation confirms this, the result of which is shown in Figure 3.12. Perfect reconstruction of all PE except after-pulses was assumed. When an after-pulse was created, with a probability of 0.07, the true number PE was drawn from Figure 3.4 and the reconstructed number was incremented by 1. A first degree polynomial fit shows good agreement in both slope and intercept with the full simulation.

Accurate reconstruction of PE is essential for both energy and position reconstruction. The preferentially late timing of after-pulses also has a detrimental effect on PSD, making

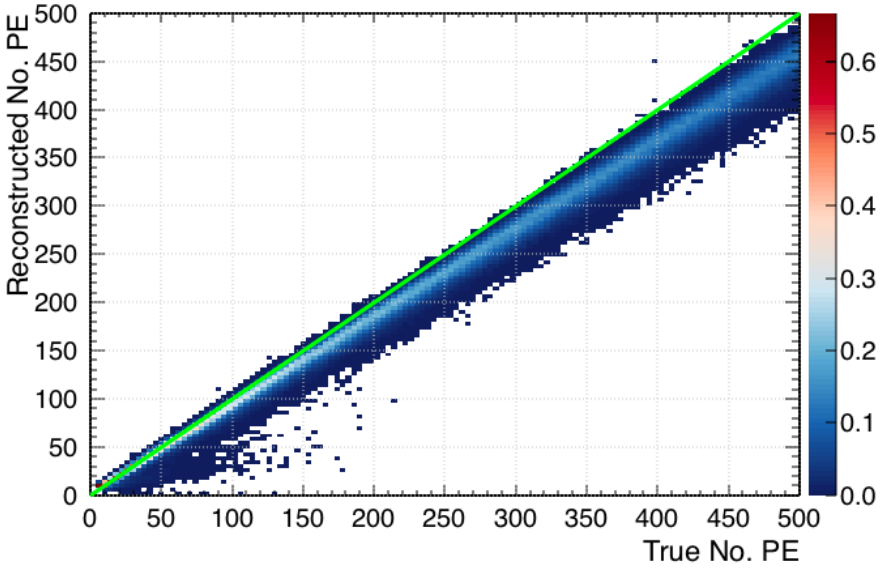


**Figure 3.10:** Reconstructed number of PE versus the true number of PE created in simulation of $^{39}$Ar events, normalised to the number of events per true PE bin. A green line is drawn along the reconstructed PE equals true PE line. This shows an under-counting bias with increasing PE due to after-pulses not being counted accurately. Pulses arriving late in the event are more likely to be identified as single PE rather than multi PE. This results in the number of PE in large after-pulses being under estimated. Events are distributed centrally, within a radius of 55 cm of the centre of the target volume, to minimise geometrical effects.

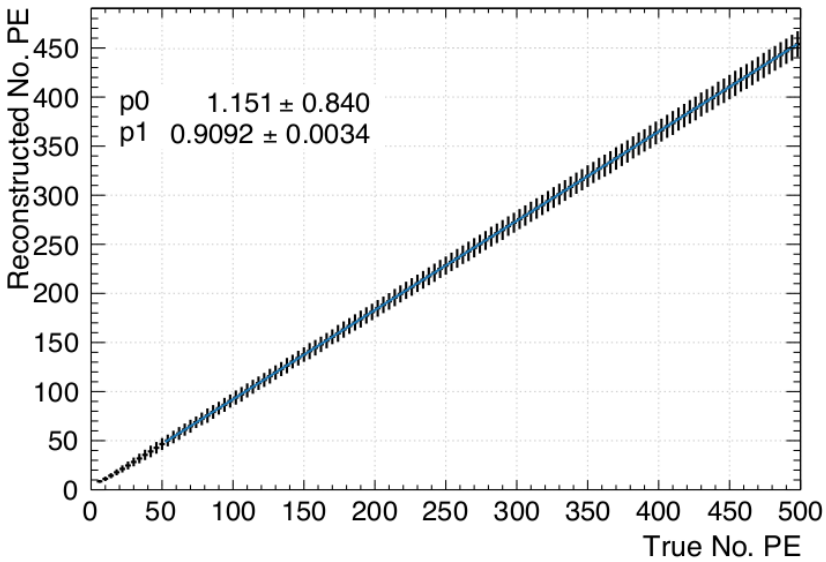


**Figure 3.11:** Profile view of Figure 3.10 fit with a first degree polynomial (where $f(x) = p1 \times c + p0$) above 50 PE. The error bars here represent the spread of the original distribution. The slope of $0.909 \pm 0.003$ agrees with what is expected drawing from the after-pulse distribution, Figure 3.4, and counting all pulses as 1 PE.

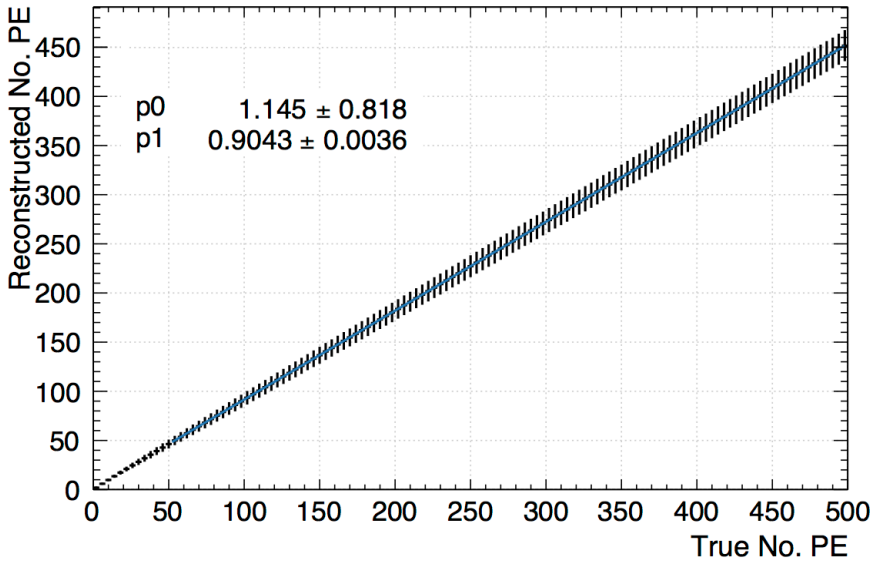


**Figure 3.12:** Dummy MC simulation of $10^4$ events per true PE count. Perfect reconstruction of all PE except after-pulses was assumed. The error bars here represent the spread of the reconstructed PE distribution. When an after-pulse was created, with a probability of 0.07, the true number PE was drawn from Figure 3.4 and the reconstructed number was incremented by 1. A first degree polynomial fit shows good agreement in both slope (p1) and intercept (p0) with the full simulation.

all events look more electronic. A method for identifying after-pulses will be described in the next section. It modifies the PE probability by including an after-pulse PDF in the prior.

### After-pulse Tagging

Every photoelectron created can potentially cause an after-pulse. The probability, $P_{\mathrm{AP}}$, that a waveform pulse is due to an after-pulse is thus dependent on the number of PE preceding the pulse in question and their distribution in time. A PDF must, therefore, be created on an event by event basis.

Since the number of photoelectrons in the waveform is not known ahead of time after-pulse identification and PE counting occurs simultaneously, moving sequentially through the waveform. The first pulse in the waveform is assumed to contain no after-pulses and the number of PE is calculated as described above. For each PE found in this initial pulse after-pulse probabilities are assigned to subsequent pulses. These probabilities are used

to calculate the number of PE, including after-pulses, in the second pulse. The number of PE in the second pulse is then used to assign probabilities to later pulses, and so on. The probability that any single pulse (referred to below as the target pulse) contains $n$ after-pulse PE, $P_{\mathrm{AP}}(n)$, can then be written as

$$P_{\mathrm{AP}}(n|t_1, t_2, N_{\mathrm{cont}}) = \mathrm{Bin}(1; N_{\mathrm{cont}}, p_{\mathrm{ap}}) \left\{ \sum_{i=1}^{N_{\mathrm{cont}}} \times P(n, \Delta\tau_i) \times P(t_i^{\mathrm{cont}}) \right\}. \tag{3.10}$$

Here $N_{\mathrm{cont}}$ is the number of photoelectrons which occur before the target pulse, each of which can cause an after-pulse. The probability that any one of these contributing PE did cause an after-pulse is then given by the binomial distribution $\mathrm{Bin}(1; N_{\mathrm{cont}}, p_{\mathrm{ap}})$. Here $p_{\mathrm{ap}}$ is the probability that a single photoelectron causes an after-pulse in the PMT. For each contributing PE the probabilities of seeing particular after-pulses within the target pulse time window are summed over. This is achieved using the joint probability, $P(n, \Delta\tau_i)$, of seeing an after-pulse of size $n$ given that it was $\Delta\tau_i$ ns after the contributing photoelectron. This is then multiplied by the probability, $P(t_i^{\mathrm{cont}})$, of seeing *any* photoelectrons at the time of the contributing PE.

$P(n, \Delta\tau_i)$ is drawn from the after-pulse histogram shown in Figure 3.4, area normalised. Taking $f(n, t)$ to be joint probability of seeing an after-pulse of size $n$ PE at time $t$ after the initial pulse we have

$$P(n, \Delta\tau_i) = \sum_{\tau_i}^{\tau_i + (t_2 - t_1)} f(n, t)\ \Delta t. \tag{3.11}$$

Here $t_1$ and $t_2$ are the beginning and end of the pulse supposed to contain the after-pulse. With further development of pulse shape analysis this time window could narrowed. The coarse, 40 ns, binning of the after-pulse histogram in use during development limits this. For data reconstruction, after-pulse PDFs will be required for each PMT with finer time binning. Building these PDFs from commissioning data will be discussed in chapter 4.

$P(t_i^{\mathrm{cont}})$ is calculated using the timing PDF, $I(t^{\mathrm{cont}})$, for each PE. This gives the probability that, beyond the PE causing an after-pulse, the original PE exists at the specified time.

Using $\mathrm{Bin}(1; N_{\mathrm{cont}}, p_{\mathrm{ap}})$ assumes that each pulse can contain after-pulses due to only one of the previous photoelectrons. This assumption holds for events with less than $\sim 10$ PE per PMT. Figure 3.13 shows the probability of two or more after-pulses occurring within $\Delta t$ nanoseconds of each other. With $p_{\mathrm{ap}} = 0.07$, events with less than $\sim 10$ PE per PMT have a probability of $< 10^{-2}$ that after-pulses from two separate PE will overlap in time between typical pulse lengths of 50 and 100 ns. This would occur for events distributed in the centre of the detector with $> 2000$ PE, well above the energy region of interest. The calculation complexity without this assumption scales as $O(n!)$. This becomes highly impractical, if not impossible, to calculate for more than a few contributing PE before a pulse.

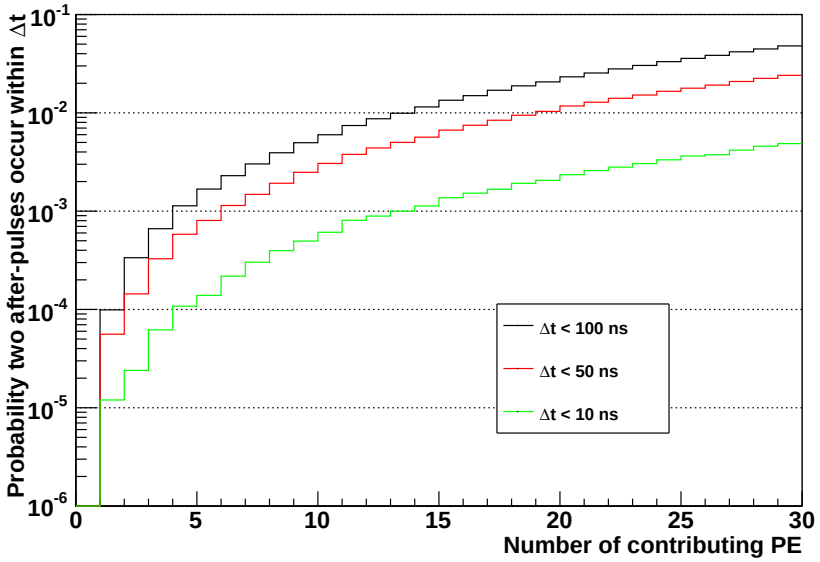


**Figure 3.13:** Probabilty of two or more after-pulses occurring within $\Delta t$ ns of each other. With $p_{\mathrm{ap}} = 0.07$, events with less than $\sim 10$ PE per PMT have a probability of $< 10^{-2}$ that after-pulses from two separate PE will overlap in time between 50 and 100 ns, a typical pulse length.

The calculation described in Equation 3.6 is modified using $P_{\mathrm{AP}}$ such that we have:

$$\begin{aligned} P_{\mathrm{N}}(n|q) &= \frac{P_{\mathrm{Q}}(q|n)\sum_{i=0}^{n} P_{\mathrm{SC}}(n-i) \times P_{\mathrm{AP}}(i)}{P_{\mathrm{Q}}(q)} \\ &= \frac{P_{\mathrm{Q}}(q|n)\sum_{i=0}^{n} P_{\mathrm{SC}}(n-i) \times P_{\mathrm{AP}}(i)}{\sum_{j=0}^{\infty} P_{\mathrm{Q}}(q|j)\sum_{i=0}^{j} P_{\mathrm{SC}}(j-i) \times P_{\mathrm{AP}}(i)}. \end{aligned} \tag{3.12}$$

Here $P_{\mathrm{SC}}$ is the prior probability, $P_{\mathrm{N}}$, in Equation 3.6. For each hypothesised value of $n$ all possible combined probabilities of after-pulse and non-after-pulse PE are summed over. Once the value of $n$ is found which maximises $P_{\mathrm{N}}(n|q)$ the number of after-pulses is then calculated by finding

$$\arg\max_{i} P_{\mathrm{SC}}(n-i) \times P_{\mathrm{AP}}(i). \tag{3.13}$$

If a pulse is found to contain only after-pulse PE or only scintillation (including dark hit) PE, times are assigned to all PE as stated above. If there is a combination of pulse types after-pulses are assigned times which occur within half a sample of each other. If there is a disagreement between the number of after-pulses found from time grouping and the number found from Equation 3.13, preference is given to time grouping.

Figure 3.14 shows the result of after-pulse removal on PE counting for $^{39}$Ar events occurring in the middle of the detector. The number of reconstructed scintillation and dark hit pulses is plotted versus the true number, the lack of overall bias can immediately be seen when compared to unmodified PE counting. The small, non-zero reconstructed PE, population at 0 true PE can be attributed to events which only contain after-pulses, due to earlier dark hits, being assigned scintillation pulses. Figure 3.15 shows a first degree polynomial fit to a profile of Figure 3.14. A slope of $0.9995 \pm 0.0026$ shows no bias within error.

This improvement over the original method is not as dramatic for nuclear recoil like events. Figure 3.16 shows reconstructed versus true PE with after-pulses removed for nuclear recoil events simulated in the middle of the detector with a flat distribution in energy. An increasing discrepancy can be seen between the reconstructed value and true value for increasing PE. This is due to scintillation pulses being misidentified as after-pulses. For nuclear recoils the triplet time PDF is given a smaller weight, $\sim 0.3$, than with electronic recoils. This results in the after-pulse probability having greater power later in the waveform. The effect is further compounded by having more contributing PE at higher energies. Since PE counting is performed separately for each PMT, there is also radial dependence to the bias; events at high radii will have larger PE counts in individual

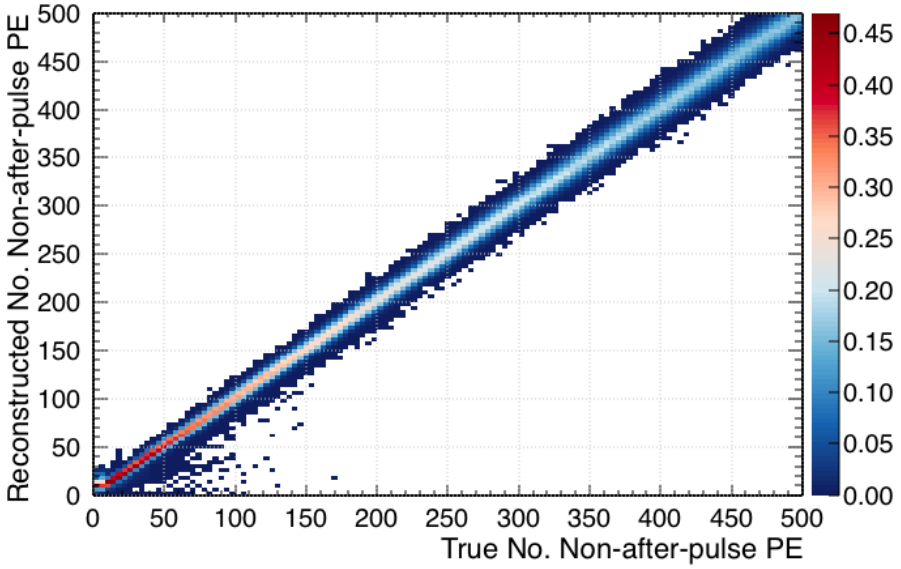


**Figure 3.14:** The number of reconstructed PE identified as not being after-pulses versus the true number of non-after-pulse PE for $^{39}$Ar events within 55 cm of the centre of the detector. The lack of overall bias can immediately be seen when compared to unmodified PE counting.

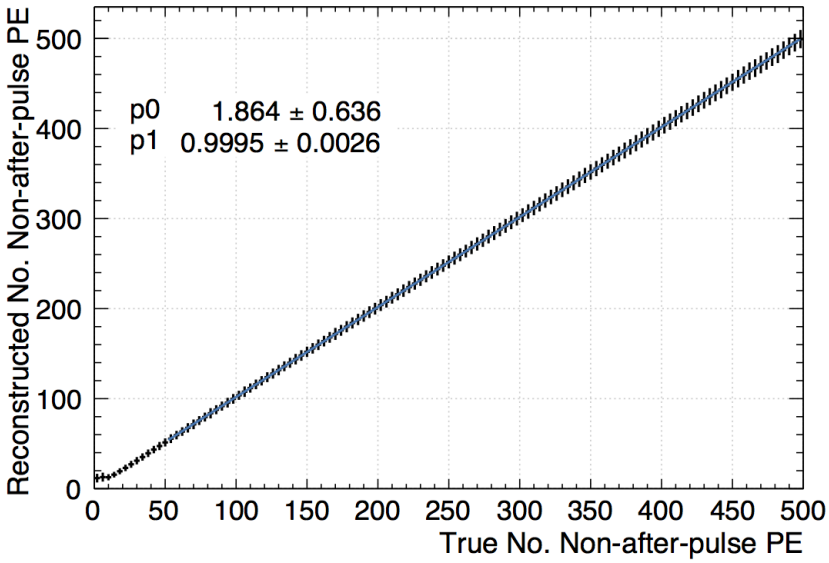


**Figure 3.15:** Profile of Figure 3.14 fit with a first degree polynomial above 50 PE. The error bars here represent the spread of the original distribution. Removal of tagged after-pulses results in a slope (p1) close to 1, showing no bias within error.

tubes. This is illustrated in Figure 3.17 where only events which occurred with a radius of greater than 55 cm are included. A large population of events with under-counted scintillation PE can be seen. Figure 3.18 shows profile views for regions of equal volume

in the detector. Events near the edge of the detector show the most disagreement with the true PE count. This effect is much less pronounced with $^{39}$Ar events, shown in Figure 3.19, where central and high radius events are indistinguishable in the energy region of interest.

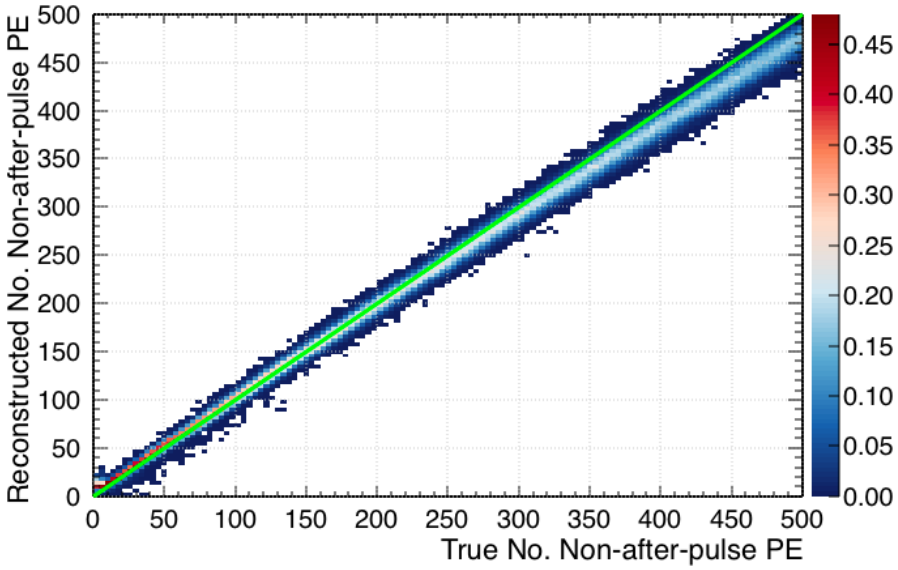


**Figure 3.16:** The number of reconstructed PE identified as not being after-pulses versus the true number of non-after-pulse PE for nuclear recoil events.

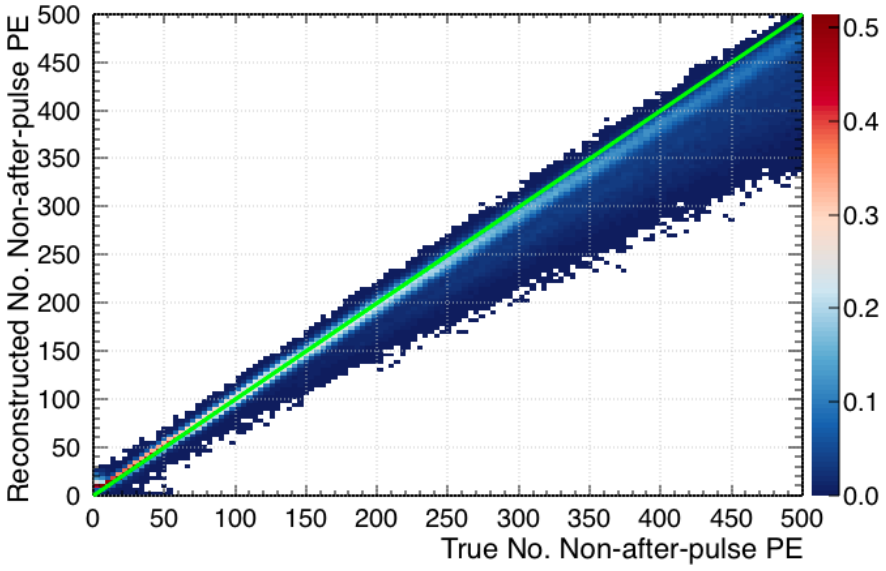


**Figure 3.17:** The number of reconstructed non-after-pulse PE versus true non-after-pulse PE for nuclear recoil events which occurred at a radius greater than 55 cm. The radial dependence to the counting bias can be seen.

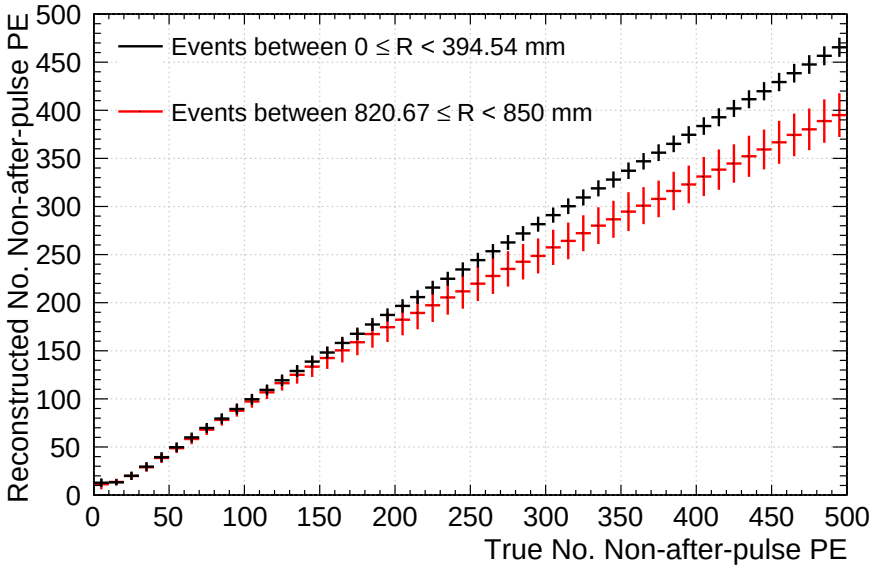


**Figure 3.18:** Profile of nuclear recoil reconstructed PE count for regions of equal volume in the centre and outer edge of the detector. The error bars here represent the spread in reconstructed PE. Events which occur near the outer edge of the detector show a large under-counting bias.

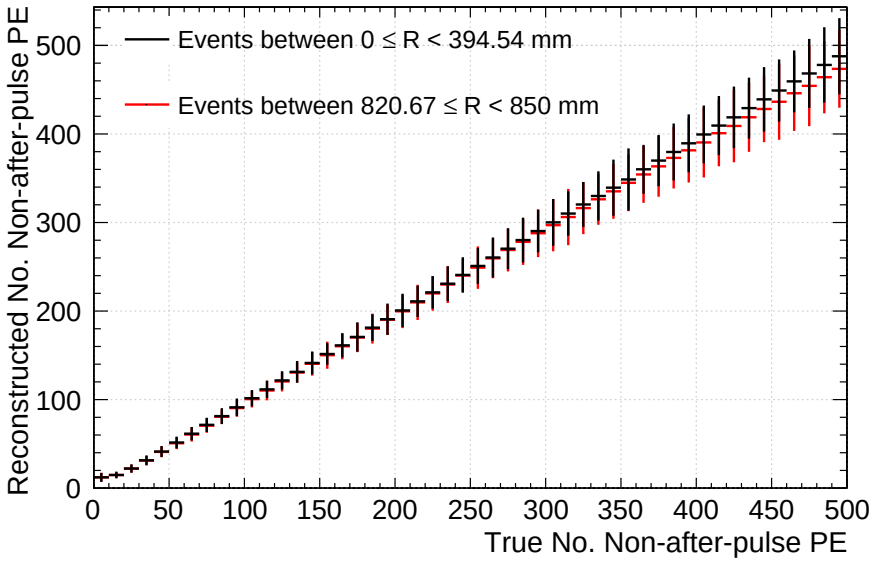


**Figure 3.19:** Profile of $^{39}$Ar reconstructed PE count for regions of equal volume in the centre and outer edge of the detector. The error bars here represent the spread in reconstructed PE. A small bias can be seen towards high PE for high radius events. In the PE region of interest central and high radius events are indistinguishable.

Figure 3.20 shows reconstructed versus true non-after-pulse PE for events found to be within 55 cm radius by the MB position fitter, described below. A first order polynomial

fit around the PE region of interest, 50 to 250 PE, shows a slope of 0.97. This is sufficiently accurate for the following work. Adjustments can be made to the after-pulse finding procedure once liquid argon data is available. Pulse information from previous events can be added to the after-pulse probabilities of the beginning of the waveform. If there is no previous event within a small enough time window probabilities could be added by making assumptions about the noise rate of the PMT in question. With the addition of pulse shape analysis more accurate initial estimates of the number of PE could be made along with their dispersion in time within the pulse. Finely binned after-pulse joint PDFs for each PMT, along with pulse shape analysis, will allow for a more accurate determination of the time order of PE in pulses containing a mixture of after-pulse and non-after-pulse PE.

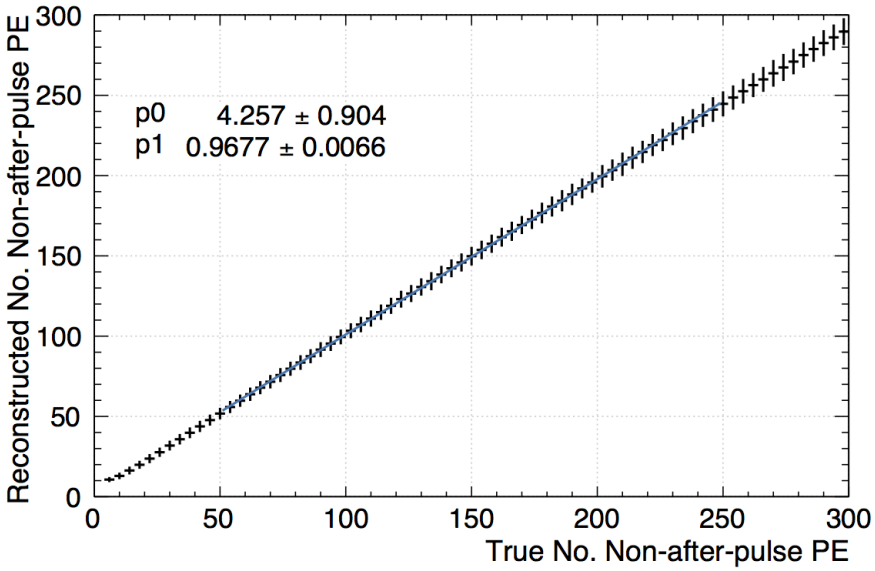


**Figure 3.20:** Reconstructed versus true non-after-pulse PE for events found to be within 55 cm radius by the MB position fitter. The error bars here represent the spread in reconstructed PE. A first order polynomial fit between 50 to 250 PE shows a 3% bias.

### 3.2.2 Pulse Shape Discrimination

As well as the $F_{\text{prompt}}$ variable two other PSD variables are described in [123], $R_{\text{prompt}}$ and $L_{\text{recoil}}$. Both are more powerful discrimination variables than $F_{\text{prompt}}$ making use of photoelectron counting and, in the case of $L_{\text{recoil}}$, full use of timing information. Use of both of these variables in DEAP-3600, with and without after-pulse identification, is described below.

#### The $R_{\text{prompt}}$ Variable

The $R_{\text{prompt}}$ variable is the PE analogue of the $F_{\text{prompt}}$ variable. Given the set of $n$ PE times, $\mathcal{T}_{\text{PE}} = \{t_1 ... t_n\}$, we have

$$R_{\text{prompt}} = \frac{|\{t : t \in \mathcal{T}_{\text{PE}}, t_0 < t < t_p\}|}{|\{t : t \in \mathcal{T}_{\text{PE}}, t_0 < t < t_{end}\}|}, \tag{3.14}$$

which is the number of PE in the prompt window over the total. The time window values are the same as for $F_{\text{prompt}}$. Using PE instead of charge removes some of the variance caused by the charge distribution of the PMTs. The $R_{\text{prompt}}$ distribution for $^{39}$Ar events distributed throughout the detector is shown in Figure 3.21, with the median of the nuclear recoil distribution shown as a red line. The nuclear recoil median $R_{\text{prompt}}$ is higher than that of $F_{\text{prompt}}$. This is because the unmodified PE counter preferentially counts later pulses as single PE. This reduces the effect large after-pulses have on the value of $R_{\text{prompt}}$.

Figure 3.22 shows $R_{\text{prompt}}$ versus PE reconstructed after the after-pulse tagging procedure. The population of high PSD events near the region of interest has been removed. After-pulses in low PE events, distributed across the full PSD window, pushed these events to higher PE. Both the nuclear recoil median and $^{39}$Ar distribution are pushed to higher $R_{\text{prompt}}$ in comparison with Figure 3.21. However, the separation between the two populations is increased, improving the discrimination power. Figure 3.23 shows the $R_{\text{prompt}}$ variable with after-pulses removed for electronic and nuclear recoil events in the middle of the detector distributed around 120 PE. Electronic recoils are distributed below $\sim 0.55$,

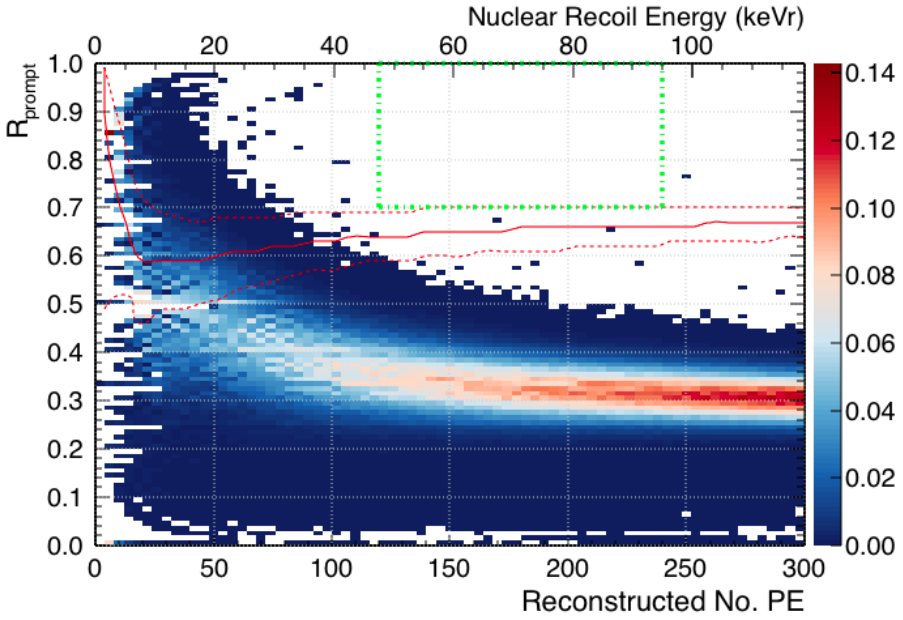


**Figure 3.21:** $R_{\text{prompt}}$ distribution for $^{39}$Ar events distributed throughout the detector. The median of the nuclear recoil distribution is shown as a red line, with the dashed lines showing 68% of the distribution. The green dash-dot line represents the nominal region of interest.

and nuclear recoils above $\sim 0.55$. This is plotted with the true $R_{\text{prompt}}$ value, built from true non-after-pulse PE times, and $F_{\text{prompt}}$ which has no after-pulse removal. After-pulse removal places the $R_{\text{prompt}}$ distribution close to the true value, which represents the best possible discrimination power with this variable. The $F_{\text{prompt}}$ separation of means was found to be 0.30, compared with an $R_{\text{prompt}}$ separation of 0.35. Taking the nuclear recoil acceptance region to be above 0.7 for this set of events, the nuclear recoil efficiency is improved by a factor of 5 at threshold.

### The $L_{\text{recoil}}$ Variable

The $L_{\text{recoil}}$ variable makes use of the full liquid argon scintillation timing distributions shown in Figures (3.6) and (3.7). It is the log-likelihood ratio between nuclear recoil and electronic recoil hypotheses. Making use of the set of $N$ PE times, $\mathcal{T}_{\text{PE}}$, it is defined as

$$L_{\text{recoil}} = \frac{1}{N} \sum_{t \in \mathcal{T}_{\text{PE}}} \left( \log P(t, E|\text{n}) - \log \text{P(t, E|e)} \right) \tag{3.15}$$

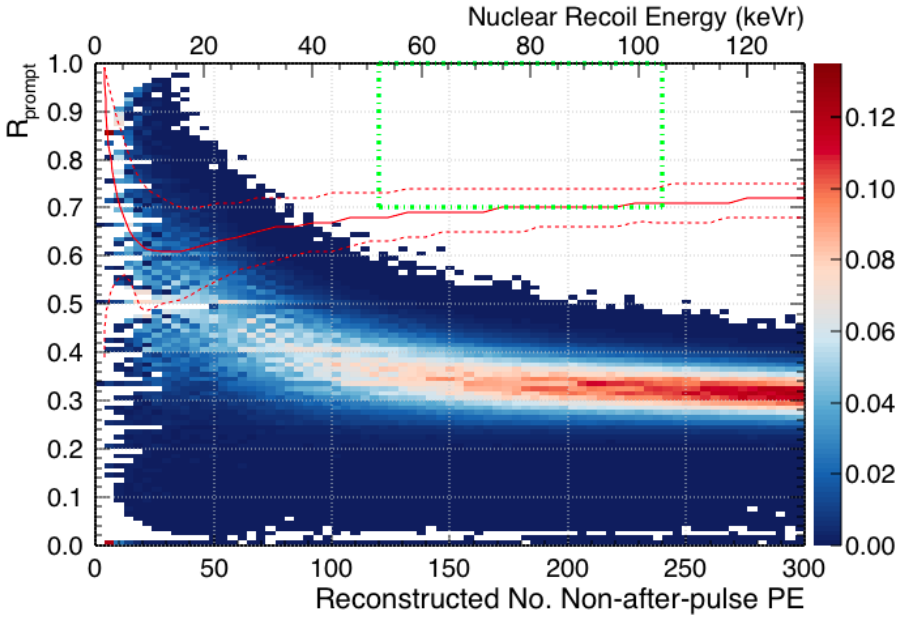


**Figure 3.22:** $R_{\text{prompt}}$ distribution versus reconstructed PE with after-pulses removed for $^{39}$Ar events distributed throughout the target volume. Both the nuclear recoil median and $^{39}$Ar distribution are pushed to higher $R_{\text{prompt}}$ in comparison with Figure 3.21. However, the separation between the two populations is increased, improving the discrimination power.

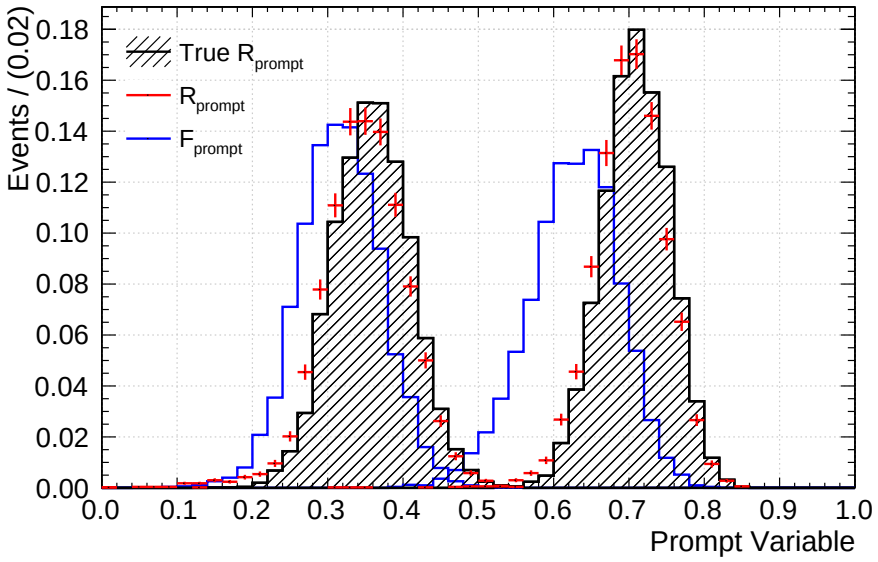


**Figure 3.23:** The $R_{\text{prompt}}$ variable with after-pulses removed for electronic and nuclear recoil events in the middle of the detector distributed around 120 PE. Electronic recoils are distributed below $\sim 0.55$, and nuclear recoils above $\sim 0.55$. This is plotted with the true $R_{\text{prompt}}$ value, built from true non-after-pulse PE times, and $F_{\text{prompt}}$ which has no after-pulse removal. After-pulse removal places the $R_{\text{prompt}}$ distribution close to the true value, which represents the best possible discrimination power with this variable.

| PSD variable | Lowest PE value |
|---|---|
| $F_{\text{prompt}}$ | 141 |
| $L_{\text{recoil}}$ | 107 |
| $L_{\text{recoil}}$ no AP | 94 |

**Table 3.1:** The lowest PE value, for an upper limit of 240 PE, for which less than 0.2 total $^{39}$Ar events would leak into the 50% nuclear recoil acceptance region. $F_{\text{prompt}}$ is compared against $L_{\text{recoil}}$ and $L_{\text{recoil}}$ after after-pulses are removed (no AP).

where $P(t, E|\text{n/e})$ is the time PDF for a recoil of energy $E$ under the assumption of a nuclear, $n$, or electronic, $e$, recoil hypothesis. The division by $N$ keeps the value of $L_{\text{recoil}}$ in a similar range between events of different energies. $P(t, E|\text{n})$ and $P(t, E|\text{e})$ are built in a similar fashion to the integrand of Equation 3.8

$$P(t, E|\text{n/e}) = \text{f}_{\text{n/e}}(\text{E})(1 - \text{f}_{\text{d}})\text{S(t)} + (1 - \text{f}_{\text{n/e}}(\text{E}))(1 - \text{f}_{\text{d}})\text{T(t)} + \text{f}_{\text{d}}. \tag{3.16}$$

where $f_{\text{n/e}}$ is the energy dependent singlet fraction. The energy is taken to be the total number of PE reconstructed divided by the light yield. For nuclear recoils this value is then divided again by the quenching factor $\mathcal{L}_{\text{eff}}^{\text{Ar}} = 0.25$.

The $L_{\text{recoil}}$ distribution versus reconstructed PE is shown in Figure 3.24. The median of the nuclear recoil distribution is plotted as a red line. The use of timing information from every photoelectron, as opposed to binning in two time regions, gives it greater discrimination power at lower energy than $F_{\text{prompt}}$. Removal of after-pulses improves the separation of nuclear and electronic recoil distributions. This is shown in Figure 3.25 where the median nuclear recoil value is more positive with the removal of tagged after-pulses. Table 3.1 shows the lower limit of the PE window which results in less than the nominal 0.2 leakage events over 3 years. Here the nuclear recoil acceptance region is defined as 50% of the total integral over the PE window. $F_{\text{prompt}}$ is compared against $L_{\text{recoil}}$ and $L_{\text{recoil}}$ after after-pulses are removed. $L_{\text{recoil}}$ combined with after-pulse tagging results in a possible 22% increase in the energy acceptance window size.

The radial bias of after-pulse removal is evident when viewing $L_{\text{recoil}}$ versus reconstructed PE for nuclear recoil events. Figure 3.26 shows the median $L_{\text{recoil}}$ versus reconstructed

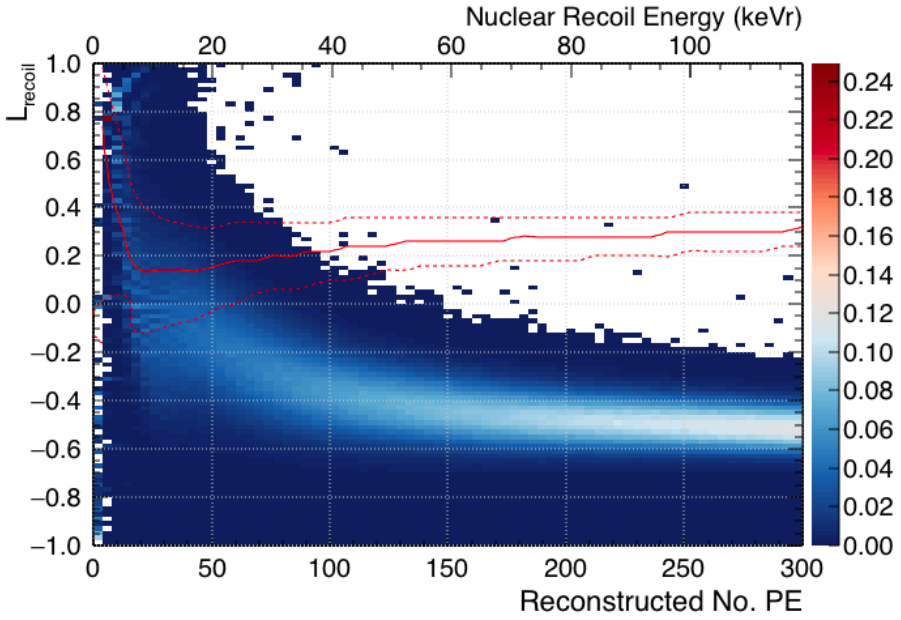


**Figure 3.24:** The $L_{\text{recoil}}$ variable versus the reconstructed number of PE for $^{39}$Ar events distributed throughout the detector volume. The median value for nuclear recoils is shown as a red line, with the dashed lines showing 68% of the distribution.

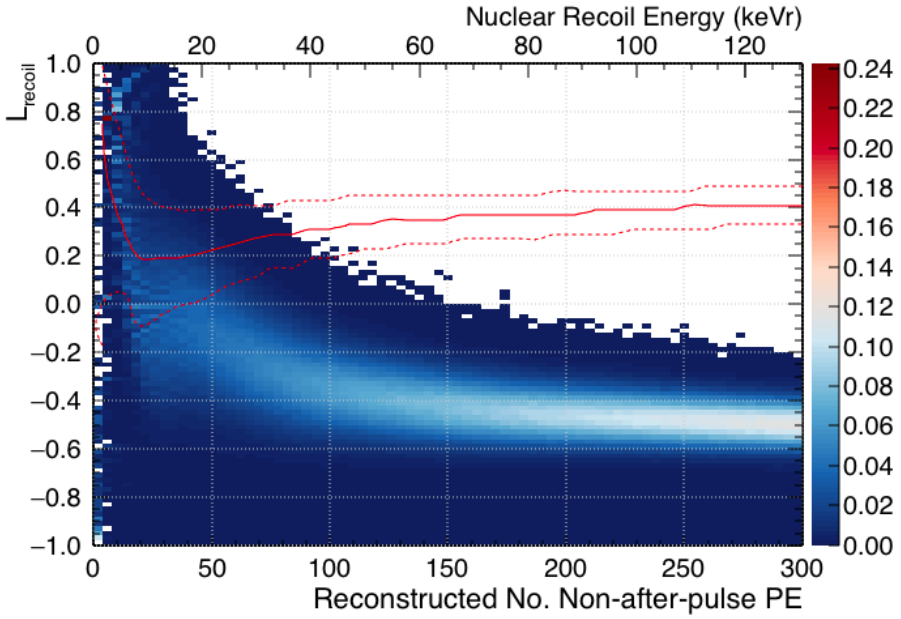


**Figure 3.25:** The $L_{\text{recoil}}$ variable versus the reconstructed number of PE with after-pulses removed for $^{39}$Ar events distributed throughout the detector volume. Removal of after-pulses improves the separation of nuclear and electronic recoil distributions.

radius in bins of equal volume for both nuclear recoil and electronic recoil events. The strong radial bias due to after-pulse tagging can be seen. Non-after-pulse photons are removed preferentially later in the waveform, causing events to look more electron like.

The bias is less pronounced within the fiducial region shown by the vertical dashed line. If the number of PE is restricted to between 100 and 240 PE, as shown in Figure 3.27, the bias virtually disappears for events within $R < 675\,\text{cm}$ ($R^3/R_0^3 < 0.5$).

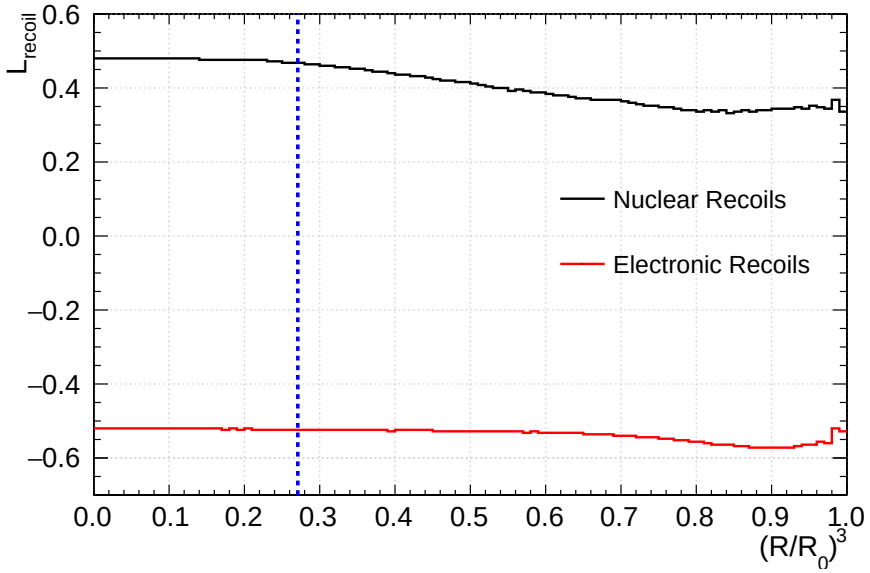


**Figure 3.26:** Median $L_{\text{recoil}}$ value versus $(R/R_0)^3$ for nuclear and electronic recoils. $R$ is radius reconstructed by the MB fitter, and $R_0 = 85$ cm. The strong radial bias due after-pulse tagging can be seen. Non-after-pulse photons are removed preferentially later in the waveform, causing events to look more electron like. The vertical line shows the fiducial volume edge of 55 cm.

### 3.2.3 Position Reconstruction

Position reconstruction algorithms in DEAP-3600 rely primarily on the relative distribution of charge, or photoelectrons, across the detector. Radioactive background contamination will primarily occur on the surface of the acrylic vessel. Accurately reconstructing the position of these surface events allows for fiducialisation; mitigating the number of surface background events by taking a reconstructed region in the middle of the detector where they will not occur.

Work is being done to include time information in the reconstruction process. This will use the times of the first detected photons to constrain the position. The size of the detector combined with the relatively slow argon scintillation lifetimes limits the power of this

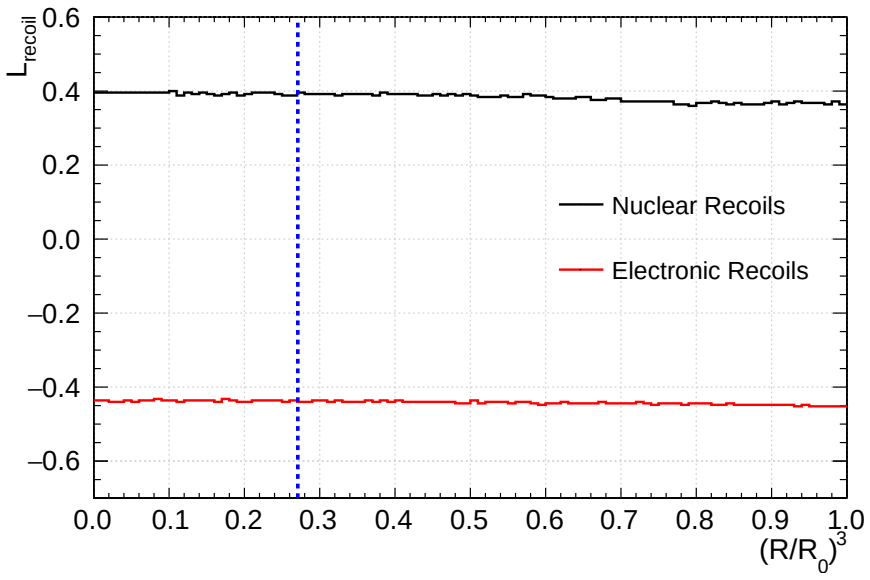


**Figure 3.27:** Median $L_{\text{recoil}}$ value versus $(R/R_0)^3$ for nuclear and electronic recoil events between 100 to 240 PE. $R$ is radius reconstructed by the MB fitter, and $R_0 = 85$ cm. The radial bias due to after-pulse tagging

approach. However, development will prove useful for the next generation of detectors, where photon flight time becomes comparable with the prompt scintillation lifetime.

Two position reconstruction algorithms are currently in development for the experiment, "Shellfit" and "MBLikelihood". Both use a similar approach, assuming spherical symmetry in the detector and making use of MC generated tables of positions relative to PMTs. The use of TPB in the detector complicates position reconstruction as photons can be re-emitted in the opposite direction to the incident scintillation light. The resulting distribution of PE looks more isotropic than what is expected when light is propagated directly. Recourse is made to Monte-Carlo, where the effect of TPB on relative light intensity can be mapped to positions.

Simulation currently assumes uniform light propagation throughout the liquid argon volume. Variations in hydrostatic pressure and temperature will affect the refractive index and further the Rayleigh scattering length. An experimental value of the scattering length has been reported as being 66 cm [124], with a theoretical value of 90 cm [125]. Preliminary simulations, using ShellFit, investigated the effect of varying the Rayleigh scattering

length between these two values. Using 20 keV electrons generated between radii of 840 to 850 mm it was found that $0.61 \pm 0.04\%$ of events reconstructed within a radius of 550 mm for 90 cm and $0.48 \pm 0.04\%$ for 66 cm. A test bench experiment is currently being performed at Royal Holloway to determine the Rayleigh scattering length, as well as the absorption length. The absorption length is due to impurities in the liquid argon, the level of impurity will be determined using the value of the triplet lifetime. Further to this, leakage studies will be performed using the expected temperature and pressure variations of the liquid argon in DEAP-3600.

**ShellFit**

Four assumptions are made by ShellFit during operation [126]:

- The detector is approximately spherically symmetric with respect to light guide placement. This is true for DEAP-3600 aside from the neck.
- Scintillation light is emitted isotropically from the event vertex.
- TPB is positioned in a spherical shell of fixed radius. This is again true for DEAP-3600 with the exception of the neck.
- TPB re-emission does not depend on the direction of the incident UV photons.

A likelihood is maximised which is function of the number of UV photons detected, $N_{\mathrm{UV}}$, given the measured set of PMT charges, $\vec{q}$, and some hypothesised event position, $\vec{r}_{\mathrm{event}}$. Given a set of measured charges $q_i$ over M PMTs in an event we have

$$\mathcal{L}(\vec{q}, N_{\mathrm{UV}}, \vec{r}_{\mathrm{event}}) = \prod_{i=1}^{M} P(q_i|\bar{C}(\vec{r}_i, N_{\mathrm{UV}}, \vec{r}_{\mathrm{event}})). \tag{3.17}$$

Here $\bar{C}(\vec{r}_i, N_{\mathrm{UV}}, \vec{r}_{\mathrm{event}})$ is the mean number of PE detected from an event which produces $N_{\mathrm{UV}}$ photons at hypothesised position $\vec{r}_{\mathrm{event}}$ in a PMT at position $\vec{r}_i$. $P(q_i|\bar{C})$ then gives the Poisson probability of seeing charge $q_i$ given mean $\bar{C}$.

$\bar{C}$ is built from a Monte-Carlo simulation of a simplified version of the detector. Photons are generated at several thousand radial positions, $\vec{r}_{\text{event}}$, in a line through the target volume with isotropic directions. These photons produce re-emitted photons across the TPB surface. These re-emission positions are sampled at $N$ points, $\vec{p}_j$, with uniform solid angle with respect to $\vec{r}_{\text{event}}$. The function $\bar{C}$ can then be given by

$$\bar{C}(\vec{r}_i, N_{\text{UV}}, \vec{r}_{\text{event}}) = N_{\text{UV}} \frac{1}{N} \sum_{j=1}^{N} E(\theta_{ij}). \tag{3.18}$$

$\theta_{ij}$ is the angle between the PMT position $\vec{r}_i$ and the point on the TPB surface $\vec{p}_j$. $E(\theta_{ij})$ is a lookup table, giving the probability that a UV scintillation photon, created at $\vec{r}_{\text{event}}$ and absorbed at $\vec{p}_j$ is detected at the PMT in location $\vec{r}_i$.

The creation of the lookup table can be performed at the beginning of each simulation or RAT analysis run. Assuming detector symmetry means a single lookup table can be built by summing over all PMT positions. This gives adequate statistics to the table which can then be used by all PMTs by applying relative photon detection efficiencies.

#### Mikhail Batygov Likelihood

The Mikhail Batygov (MB) likelihood fitter works in a similar manner to ShellFit. Through each hypothesised position $\vec{r}_{\text{event}}$ an axis, $Z'$, is drawn from the centre of the detector. The hypothesised event is then said to lie at distance $g$ along this axis. For each $g$ a probability density function $P_g(\theta_i)$ is extracted where $\theta_i$ is the angle between point $g$ and PMT $i$ such that $-1 < \cos(\theta_i) < 1$. Cylindrical symmetry is assumed about axis $Z'$. The hit pattern $P_i$ is drawn from an interpolated table of $g$ versus $\cos(\theta)$ built in simulation. Like ShellFit, this table is assumed to be the same for all PMTs. Normalising each $P_i$ to the total number of expected hits, $N_{\text{Exp}}$, the likelihood function to evaluate is

$$\mathcal{L}(\vec{r}_{\text{event}}, N_{\text{Exp}}) = \prod_{i=1}^{M} \text{Poisson}(n_i | N_{\text{Exp}}, P_g(\theta_i)), \tag{3.19}$$

where $n_i$ is the number of observed hits in PMT $i$. The hit pattern for each possible vertex is generated from high statistics simulations. This gives MBLikelihood a disadvantage when compared to ShellFit's on the fly table generation, as several hundred CPU hours of simulation are required.

### Performance with $^{39}$Ar

The accuracy of each of the position reconstruction algorithms depends on the number of PE detected in an event. This is illustrated in Figure 3.28 where the magnitude of the vector difference between reconstructed and generated points is plotted as a function of reconstructed PE. Below 50 PE the accuracy of both algorithms degrades sharply. Both algorithms have a reconstruction resolution of approximately 10 cm above 100 PE, with MBLikelihood having a marginally better mean accuracy over all energy ranges.

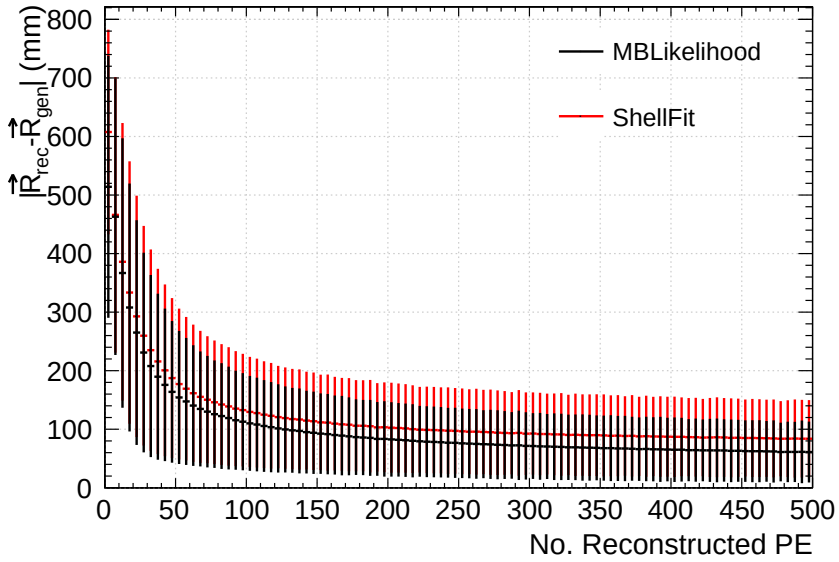


**Figure 3.28:** The magnitude of the vector difference between reconstructed and generated points plotted as a function of reconstructed PE. Below 70 PE the accuracy of both algorithms degrades sharply.

Since the $^{39}$Ar spectrum is well understood and uniform throughout the target volume it can be used to evaluate the performance of position reconstruction. Figure 3.29 shows simulated $^{39}$Ar events which reconstruct within 100 to 240 PE. Both position fitters are biased towards the centre and edges of the detector. Towards the centre of the detector

light is distributed isotropically within Poisson error, preventing an accurate determination of vertex position. Towards the edge of the detector the assumption of spherical symmetry breaks down, giving individual PMTs more power to skew the position of the reconstructed vertex towards them. Both reconstruction algorithms ultimately lead to an overpopulation of events within the fiducial volume. MBLikelihood causing $1.12 \pm 0.001$ times as many events generated there and ShellFit causing $1.09 \pm 0.001$.

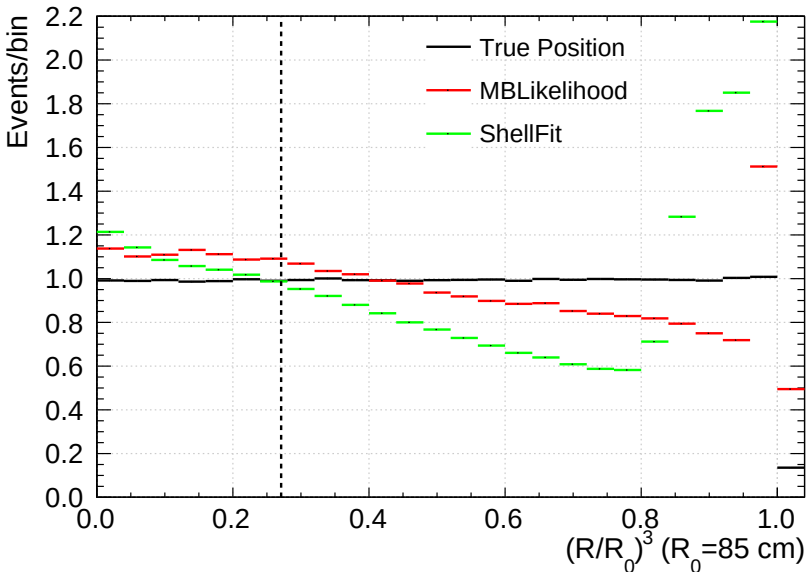


**Figure 3.29:** The number of events between 100 and 240 PE reconstructed in bins of equal volume with both MBLikelihood and ShellFit compared to the number generated. The vertical dashed line is at 550 cm, the edge of the fiducial volume.

### Energy Reconstruction

Both ShellFit and MBLikelihood use a hypothesised energy scale in the form of an expected number of photons. In ShellFit the total number of UV photons is estimated. To convert this to electron equivalent energy this number is divided by the scintillation yield of 40 photons/keV. In MBLikilihood the expected number of detected PE is divided by the detected light yield. In both fitters the PMT model is not yet fully implemented with Poisson statistics being assumed. PMT effects such as after-pulsing and double pulsing skew the energy reconstruction results.

## 3.3 Conclusion

In this chapter the RAT simulation framework has been described. It is designed to accurately replicate both the physics of DEAP-3600 and the data output. RAT makes no distinction between MC generated and real data when performing analysis allowing ease of development of analysis software. A time based statistical approach to photoelectron counting has been described and its modification to include after-pulses. The after-pulse modification adequately counts scintillation and noise PE for both nuclear and electronic recoils within the region of interest. Use of this modified PE counting in higher level PSD was shown to increase the separation between nuclear and electronic recoil populations. Further development of this technique will involve more accurate after-pulse PDFs built from calibration data and the use of pulse shape analysis.

In the next chapter calibration hardware and software will be described. A preliminary after-pulse PDF using optical calibration with the laserball will be presented.

Initial analysis of DEAP-3600 will use the "nominal" region of interest ($120 < \mathrm{PE} < 240$, 1000 kg fiducial mass, 50% signal acceptance) extrapolated from DEAP-1. As has been shown in section 3.2.2 the threshold value can be placed below 120 PE, keeping the other nominal values fixed. The region of interest should be optimised, by maximising the value of $\mathrm{signal}/\sqrt{\mathrm{signal} + \mathrm{background}}$ in bins of PE, for example. This will require accurate modelling of the surface background distribution, on which work is currently being carried out. A full background simulation is required with detector optical properties constrained by calibration data. Further to this, surface backgrounds must be extrapolated into the central region of the detector as the amount of simulation data required to do this would be impractical. The affect of systematics on the number of signal and background events will also have to be explored. For a likelihood based analysis full background PDFs will have to be determined along with systematics which affect both the shape and normalisation of each distribution.

# Chapter 4

# Detector Calibration Systems

*The neutron is a bit of a drama queen.*

Sean Carroll

The DEAP-3600 calibration system is comprised of two external radiation sources, two optical photon sources, and a pulse generator for separate calibration of electronics channel timing offsets. An overview of the calibration systems will be presented here with preliminary studies of optical calibration data used to determine the extent of after-pulsing in each PMT. The neutron calibration system was delivered by Royal Holloway, University of London. It will be used to populate the detector with nuclear recoil like events to characterise pulse shape discrimination. The gamma calibration system was designed and built by the Rutherford Appleton Laboratory. This will be used to characterise the position reconstruction resolution at the edge of the detector as well as overall energy scale (light yield). The optical calibration systems were delivered by the University of Sussex. These will be used to characterise PMT responses and detector optics. Finally, the in situ timing electronics was implemented by TRIUMF. This will be used to calibrated channel to channel timing in the detector.

## 4.1 Test Pulse Time Calibration

Time offsets between channels must be compensated for in order to provide accurate timing information for PSD. Channel timing calibration is performed using a pulse-pattern-generator (PPG). These pulses are injected periodically during a run through the SCBs into the electronics chain. The digitizer sampling time is 4 ns, while the PMT timing jitter is 1 ns. The timing calibration should be limited by the PMT jitter i.e. better than 1 ns. In order to do better than the digitizer sampling time the PPG pulse shape and position is fit using an RC function:

$$V(t) = \begin{cases} A\left(\frac{t-t_0}{\tau}\right)^2 \exp\left\{-\frac{t-t_0}{\tau}\right\} & \text{if } t \geq t_0 \\ 0 & \text{if } t < t_0. \end{cases} \tag{4.1}$$

where $t_0$ is the start of the pulse. The normalisation factor, $A$, and time constant, $\tau$, are left as free parameters in the fit. An example of a PPG pulse fit using this function is shown in Figure 4.1. The fit region is shown in red with the full function shown in blue. The beginning of the fit region is set to where the leading edge falls below twice the baseline. The end of the region is set to where the samples fall below 30% of the pulse height. This ensures the leading edge of the pulse is enclosed while avoiding the potentially noisy tail region.

An example of the distribution of $t_0$ times found during a run for PMT 143 is shown in Figure 4.2. PPG pulses were distributed through all channels at 50Hz during an optical calibration run. To determine the overall channel offsets a 1 ns window is chosen which contains the highest number of $t_0$ times. The arithmetic mean of times within this window is then taken as the channel time. This limits the effect of spurious noise pulses in the waveform. To calculate the relative offsets the 4 ns sample which contains the most PPG pulses across all channels is selected as the reference time. Channel times are then recorded relative to this reference time. Sub nanosecond precision is obtained through fitting the PPG pulses as described above, with the typical RMS for PPG pulse distributions being $\sim$0.1 ns.

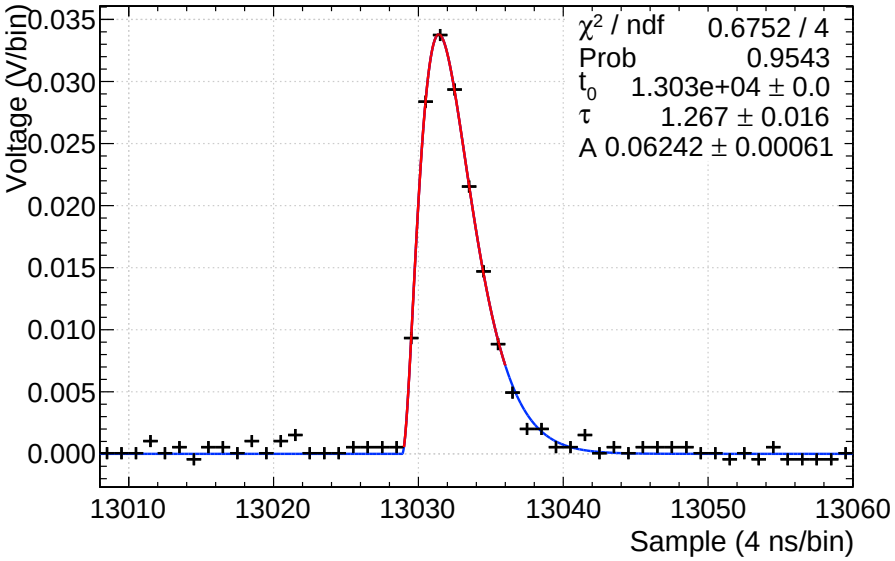


**Figure 4.1:** Example of baseline subtracted PPG pulse fit with Equation 4.1, the sample error is set to be the baseline RMS. The fit region is shown in red with the full function shown in blue. The beginning of the fit region is set by moving from the maximum voltage backwards until the samples fall below twice the baseline. The end of the region is set to where the samples fall below 30% of the maximum. This ensures the leading edge of the pulse is enclosed while avoiding the potentially noisy tail region.

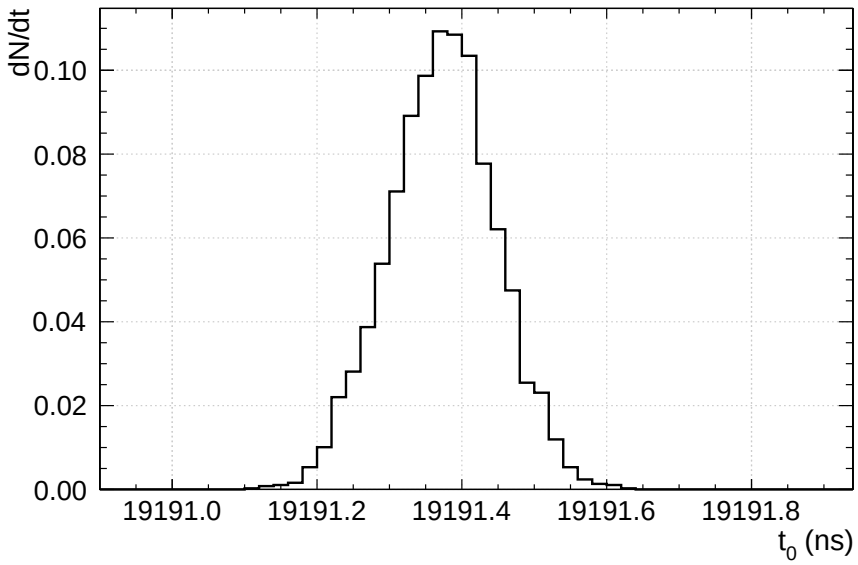


**Figure 4.2:** Distribution of $t_0$ times from PPG pulses generated during an optical calibration sub run for PMT 143, showing a mean of $t_0$=19191.37 ± 0.07 ns. A 1 ns window is chosen which contains the highest number of $t_0$ times. The arithmetic mean of times within this window is then taken as the channel time. This limits the effect of spurious noise pulses in the waveform. To calculate the relative offsets the 4 ns sample which contains the most PPG pulses across all channels is selected as the reference time. Channel times are then recorded relative to this reference time.

## 4.2 External Radioactive Calibration Sources

Two radioactive sources are in use in the experiment to calibrate the detector's response to nuclear and electronic recoils. Nuclear recoils will be calibrated using a neutron source, described in Section 4.2.1, and electronic recoils using a gamma source, described in Section 4.2.2. These sources will be deployed in to the detector calibration ports periodically throughout the lifetime of the experiment.

**Figure 4.3:** The gamma (left and middle) and neutron (right) source deployment systems on site at SNOLAB. The neutron source deployment system is designed to lower the source canister down the vertical calibration tubes. The gamma source deployment system is designed to move the source canister around the circular Cal F tube as well as the vertical ports. Image courtesy of M. Ward.

### 4.2.1 Neutron Calibration System

The neutron calibration system populates the detector with nuclear recoils from a known spectrum. It uses a 74 MBq AmBe source which is deployed externally to the steal shell. The neutron source deployment system, shown on the right in Figure 4.3, is designed to lower the AmBe source down the vertical calibration tubes surrounding the detector.

The source canister consists of several components for both encapsulation and tagging. Tagging is achieved through the use of two back-to-back $40 \times 51$ mm NaI crystals which surround the source. Each of these is coupled to a 38 mm ETL 9102 PMT. A neutron is created when an alpha particle, produced by $^{241}$Am, strikes a $^{9}$Be nucleus. This produces, among other things, an excited $^{12}$C state and a neutron. Figure 4.4 shows the AmBe neutron energy spectrum plotted in arbitrary units. The $^{12}$C then de-excites releasing a 4.4MeV gamma which can potentially deposit its energy into one of the NaI crystals. In simulation it was determined that 22% of the de-excitation gammas deposit more than 500keV of energy [95], with 10% depositing 4.4 MeV. This was set as the crystal trigger threshold, with a further requirement of a threshold number of hit PMTs in the detector before the event is written to disk. $^{241}$Am also emits 60keV gammas at a high rate. The AmBe source is wrapped in 2 mm of lead foil which reduces these gammas by 99.9%. Activation in the steel shell was studied in preliminary simulations. No long lived unstable isotopes were created, i.e., those with half lives greater than the order of seconds. Events occurring within an hour of source removal will be ignored further mitigating the risk of activated isotopes causing events in the detector.

Due to the neutron shielding materials surrounding the target volume, and the distance of the calibration tubes, the rate of interactions in the target volume is low. From a simulation of $6 \times 10^7$ neutrons only 0.023% interacted in the liquid argon volume and 0.008% deposited more than 50 keV of energy. Of that 0.008% of neutron interactions 19% were single nuclear recoil scatters, i.e., WIMP like events.

Neutrons take a relatively long time to travel from the calibration tube to the target

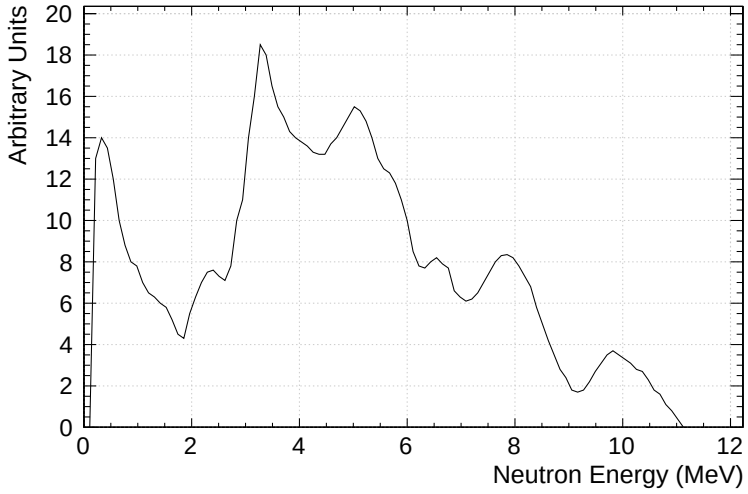


**Figure 4.4:** The AmBe neutron energy spectrum plotted in arbitrary units.

volume, with only 43% of neutrons arriving in the detector within 100 ns. A large detection window will increase the rate of neutron acceptance, however, the size of this window is limited by pile-up with $^{39}$Ar events. A detection time window of 100 ns was defined from the NaI crystal trigger to the inner detector PMT trigger. When combined with the 22% efficiency of the NaI crystal this gives a 9.5% tagging efficiency. This results in a tagged neutron event rate of 0.05 Hz. When compared to the $^{39}$Ar rate in the same energy region of 0.02 Hz this gives a signal-to-noise ratio of approximately 2:1. Each data run will require $10^4$ neutron elastic scatter events to populate the fiducial volume of the detector, giving a statistical error of 1%. These events will primarily be used for characterising nuclear recoil pulse shape discrimination.

### 4.2.2 Gamma Calibration System

The gamma calibration system populates the detector volume with gamma rays of a known energy. These will be used to calibrate the energy scale and resolution of the detector in conjunction with $^{39}$Ar. A 1 MBq $^{22}$Na source is used which, like the neutron system, is deployed externally to the steel shell. The gamma source deployment system, shown in the middle and left of Figure 4.3, is designed to move the source canister around the circular

Cal F tube.

$^{22}$Na emits a 1.27MeV gamma ray together with a positron. The annihilation of the positron, causing the subsequent emission of a pair of 511keV photons, is used to tag the calibration source. Like the neutron source, the $^{22}$Na is sandwiched between two crystal scintillators each coupled to a PMT. In this case LYSO (Cerium-doped Lutetium Yttrium Orthosilicate) crystals are used along with two Hamamatsu R9880U PMTs. A tagged event must deposit 511 keV of energy in each crystal within 20 ns and cause a 1.27 MeV gamma interaction in the liquid argon. From simulation approximately 29% of the high energy gammas make it into the liquid argon with full energy.

The extent of random coincidences and pile-up with $^{39}$Ar events was estimated using Monte-Carlo. The rate of double coincidence with both LYSO crystals was found to be 223 kHz. The rate of these events coinciding within 20 $\mu$s of an $^{39}$Ar event was found to be 0.032 kHz. In contrast, the rate of double coincidence events occurring in conjunction with a 1.27 MeV gamma interaction in the target volume was found to be 1.2 kHz. There is an additional background rate from the $^{176}$Lu found in the LYSO material. The decay of this isotope causes a cascade of three gammas of 307, 202, and 88 keV energies. The expected rate falling within a 100 keV energy window of 511 keV is 220 Hz, taking into account the 8% energy resolution of the LYSO crystal [95].

The 1.27 MeV gamma events populating the detector will be used to determine the light yield and energy resolution of the detector. The known $^{39}$Ar spectrum will then be used to extrapolate down into the energy region of interest. The spectrum will be scaled to simulation to determine the energy scale. This scale will be matched with that found for the gamma events. A mismatch between these values would indicate a non-linearity in the detector energy response. In addition to the tagged high energy calibration events the detector will be populated with relatively low energy gammas from scattering. From simulation it was found that these gammas most frequently enter the detector with an energy of around 50keV. At this energy the attenuation path length in liquid argon is 1 cm. This provides low energy surface events for determining the efficacy of position

reconstruction algorithms, particularly when making use of the circular Cal F tube. Uniformly distributed $^{39}$Ar events would give an indication of the overall bias of the position fitting algorithms. However, on an event by event basis the true position is unknown. A source at a known position would break this degeneracy, allowing for characterisation of the leakage of AV surface events towards the centre of the detector.

## 4.3 Optical Calibration

Determining the optical properties of the detector and its ability to transmit scintillation light is of paramount importance. There are two optical calibration systems used in the experiment. The internal AARF light injection system, described in Section 4.3.1, and the optical diffusion flask, or "laserball", photon source, described in Section 4.3.2. The optical diffusion flask was deployed prior to filling with liquid argon and after TPB deposition in July of 2015. The AARF light injection system will be used throughout the lifetime of the experiment. Data from the optical flask deployment will be used to:

- determine the timing of the PMT channels from a centralised light source in combination with input test pulses, described in Section 4.1.
- characterise the after-pulse rate and distribution for each PMT, see Section 4.3.2.
- set limits on the distribution of TPB using a UV light source.

Both the AARF and laserball systems are used to characterise the PMT response in combination with the optical properties of the AV and light guides close to the TPB emission spectrum. The AARF system will be used to determine the single photoelectron (PE) charge prior to each physics run.

### 4.3.1 Aluminium and Acrylic Reflectors

The position of the aluminium and acrylic reflectors ("AARFs"), relative to the host PMT, is shown in Figure 4.5. The central axis of the AARF points towards the centre of the

face of the PMT. In addition to the 20 distributed around the inner detector PMTs, two are positioned in the neck to characterise the effect of neck geometry. Light is supplied by optical fibres which are connected to 435 nm LEDs. The LED driver electronics delivers a fast, 2 ns, rise time. Each LED has a dedicated APD which monitors the light intensity fed into the optical fibre.

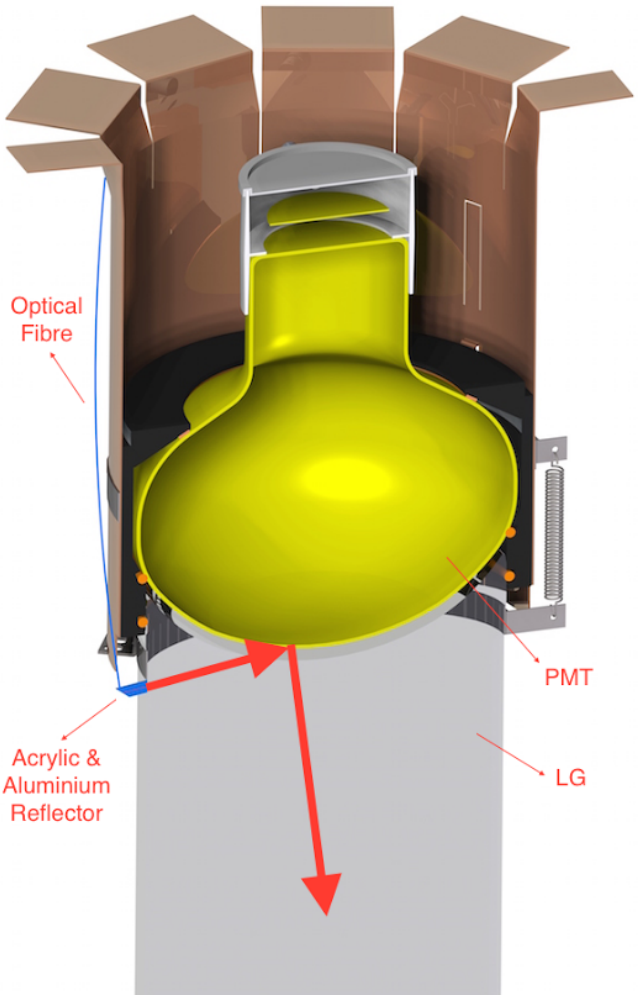


**Figure 4.5:** Rendering of the position of the AARF with respect to its host PMT. The AARF is angled such that its central axis points towards the centre of the face of the PMT. Light is transmitted down the optical fibre and AARF, bounces off the face of the PMT, and makes its way into the inner detector.

The AARF system is used to calibrate the single PE charges, in response to a triggered light source, over the lifetime of the experiment. The majority of generated light is detected by the host PMT with a fraction being reflected. The distribution of light from a single AARF run while the AV was under vacuum is shown in Figure 4.6. The total charge

detected in the waveform peak relative to the host PMT is plotted across the angular distribution of PMTs in $\cos(\theta)$ versus $\phi$. Figure 4.7 shows how this peak charge was defined for pulses seen in PMT 100. AARF number 1 was fired, which is connected to PMT ID 21, at $\cos(\theta) = 0.8$ and $\phi = -2.5$ radians. This was removed from the plot so smaller charge fractions can be distinguished. The vast majority of reflected light is detected in the PMTs immediately surrounding PMT 21. From simulation this was found to correspond to light which internally reflects in the AV. Figure 4.8 shows the peak charge relative to PMT 21 for PMTs sorted by their distance from PMT 21. The vast majority of charge is found in the host PMT with the surrounding PMTs seeing just 3% of that initial charge. The arrangement of 20 AARFs ensures coverage of all PMTs in the detector.

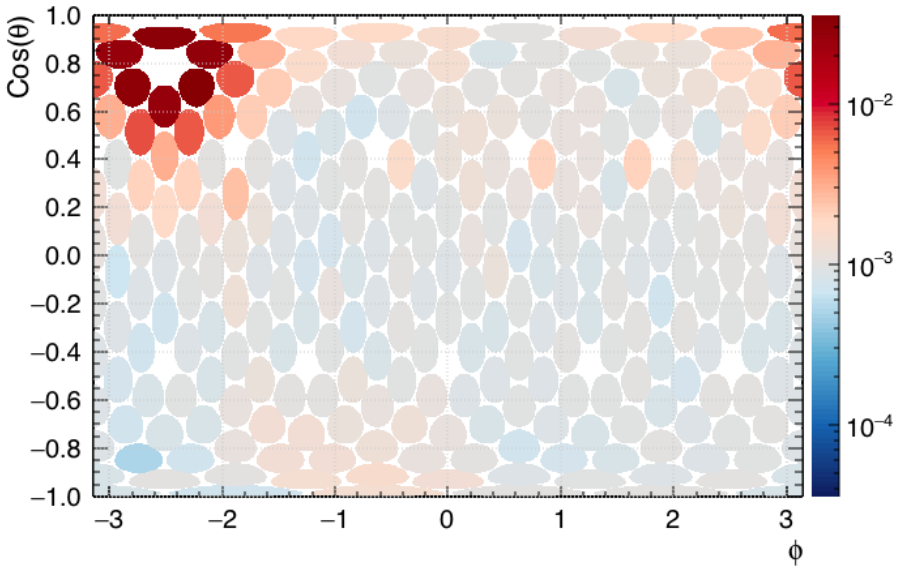


**Figure 4.6:** The total charge detected in the waveform peak (see Figure 4.7) relative to the host PMT is plotted across the angular distribution of PMTs in $\cos(\theta)$ versus $\phi$. AARF number 1 was fired, which is connected to PMT ID 21, at $\cos(\theta) = 0.8$ and $\phi = -2.5$ radians. This was removed from the plot so smaller charge fractions can be distinguished. The vast majority of reflected light is detected in the PMTs immediately surrounding PMT 21.

### 4.3.2 Optical Diffuser Flask

The optical diffuser flask is designed to supply an approximately isotropic source of photons of various wavelengths from the centre of the detector. The optical response of each PMT

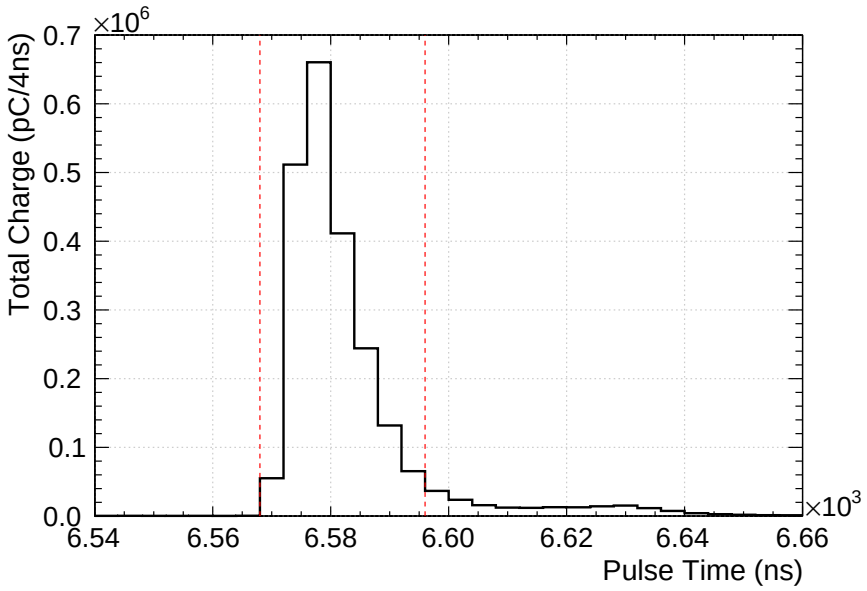


**Figure 4.7:** Total charge per pulse sample for PMT 100. Vertical lines show the integration window used to define the peak charge in the channel. The start is defined as when a sample is greater than 5 times the RMS of the first 4 $\mu$ss of samples. The end is defined as when the pulse drops below 10% of the maximum. This avoids the shoulder caused by after pulsing at times greater than 6.61 $\mu$s.

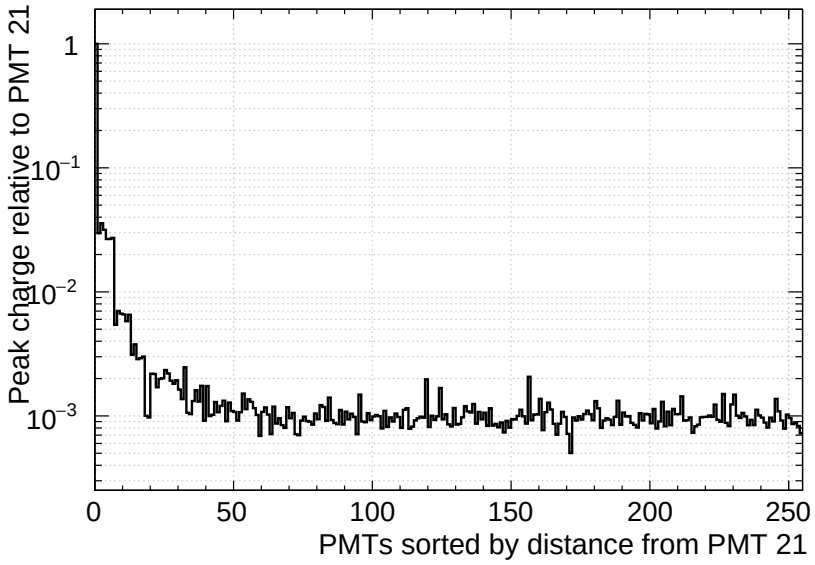


**Figure 4.8:** Peak charge relative to PMT 21 for PMTs sorted by their distance from PMT 21. The vast majority of charge is found in the host PMT with the surrounding PMTs seeing just 3% of that initial charge.

in combination with its light guide can then be calibrated. The source was deployed before argon filling but after TPB deposition. The flask itself, shown in Figure 4.9, is made from

perfluoroalkoxy alkane (PFA) and filled with 40 $\mu$m glass beads suspended in silicone gel. Light is supplied by a laser situated on the deck via an optical fibre. A Hamamatsu PLP-10 picosecond light pulser is used in conjunction with three different laser diode heads of 375 nm, 405 nm, and 445 nm wavelength [127, 128, 129]. The 375 nm wavelength activates the TPB providing information about its distribution and thickness. The 445 nm wavelength does not activate the TPB and can be used to calibrate the relative timing response of the PMTs. The direct activation of the PMTs and known start time can also be used to characterise after-pulsing in individual PMTs. The 405 nm wavelength has better transmission through the light guide but will cause some activation of the TPB.

The PFA flask does not emit light isotropically. More light is transmitted through the bottom of flask resulting in $\theta$ non-uniformity. This is due to the fibre position near the centre of the flask combined with a higher density of glass beads near the top of the flask. Imperfections in the PFA also cause rotational, or $\phi$, non-uniformity. To decouple this non-uniformity from the data calibration runs were performed with the flask in several positions. Here we define (0,0,0) as the centre of the acrylic vessel and the positive $z$ axis as the centre of the neck. The flask was deployed in three positions (0,0,0), (0,0,550 mm), and (0,0,-550 mm) within $\pm$20 mm. It was also rotated in $\phi$ in four positions separated by $90^\circ \pm 5^\circ$.

Figure 4.10 shows the distribution of peak charge (as defined in Figure 4.7) compared to the maximum peak charge for the 445 nm laser head in the (0,0,0) position. The non-uniformity of the flask can be seen as charge generally increases towards $\cos(\theta) = -1$. This is combined with the relative efficiency of each of the PMT and light guide modules at this wavelength. The 445 nm distributions in the (0,0,550 mm) and (0,0,-550 mm) positions are shown in Figures (4.11) and (4.12) respectively. The $\theta$ non-uniformity in the flask causes the fractional difference in peak charge to change at a steeper gradient in $\cos(\theta)$ in the (0,0,-550 mm) position than the (0,0,550 mm) position. Decoupling the non-uniformity of the source from the optical properties of the detector will use a similar approach to Section 7.1.3 of [130].

**Figure 4.9:** Optical diffuser flask made from perfluoroalkoxy alkane (PFA) and filled with 40$\mu$m glass beads suspended in silicone gel. Light is supplied from a laser situated on the deck via an optical fibre. A Hamamatsu PLP-10 picosecond light pulser is used in conjunction with three different laser diode heads of 375 nm, 405 nm, and 445 nm wavelength.

### After-pulsing

A study of the extent of after-pulsing can be performed on a PMT by PMT basis and need not take any relative differences into account. Using an optical flask calibration run with a low PMT occupancy light pulse of the 445 nm laser head, and an event time window of 200 $\mu$s, a preliminary study of after-pulsing in PMT 254 was performed.

Channel to channel timing offset calibration has yet to be applied so the initial hit time was determined from the data. The time region for the laser pulse was set by the trigger

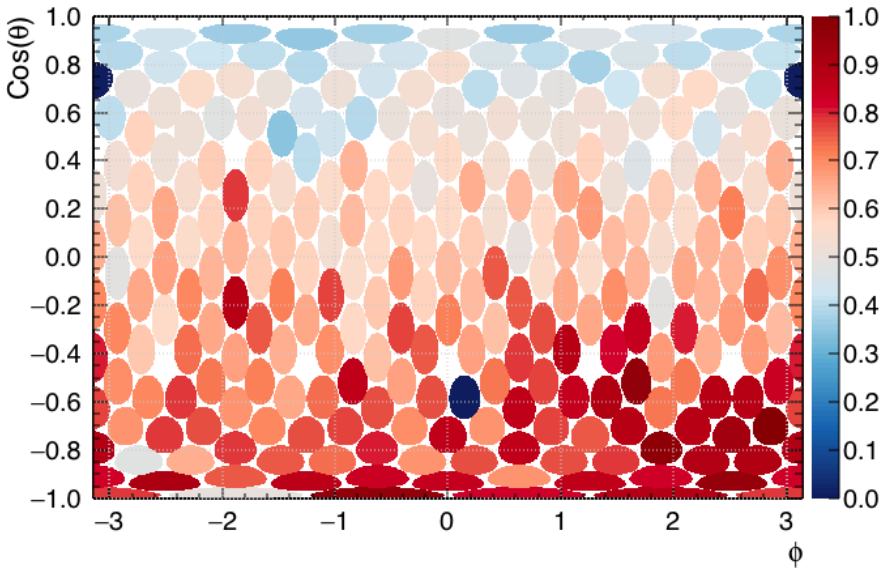


**Figure 4.10:** The distribution of peak charge (as defined in Figure 4.7) compared to the maximum peak charge for the 445 nm laser head in the (0,0,0) position. The non-uniformity of the flask can be seen as charge generally increases towards $\cos(\theta) = -1$. This is combined with the relative efficiency of each of the PMTs at this wavelength.

information to be between 19.2 and 20 $\mu$s. Within this region time constraints were set in a similar manner to the AARF pulses above. Figure 4.13 shows pulse times weighted by pulse integral charge for a sample of the run. The start of the arrival time region was set to where the charge became 10 times the RMS of the 100 ns region preceding the trigger time. The end was set to when the charge per bin dropped below 5% of the maximum. This results in a 20 ns window which cuts out much of the potential PMT effects such as double pulsing.

The noise rate of the PMT was then determined in situ. Events were chosen where no pulses occurred in PMT 254 between 19.2 and 20 $\mu$s and more than one pulse occurred outside this region. Since the dark rate follows a Poisson arrival distribution, time differences between consecutive pulses were recorded and fit to an exponential distribution outside the potential after-pulse region. The result of this is shown in Figure 4.14 where a noise rate of $12.2 \pm 0.085$ kHz was found for PMT 254. This is a reasonable value at room temperature.

Candidate after-pulse events were chosen to be those which contained only two pulses in

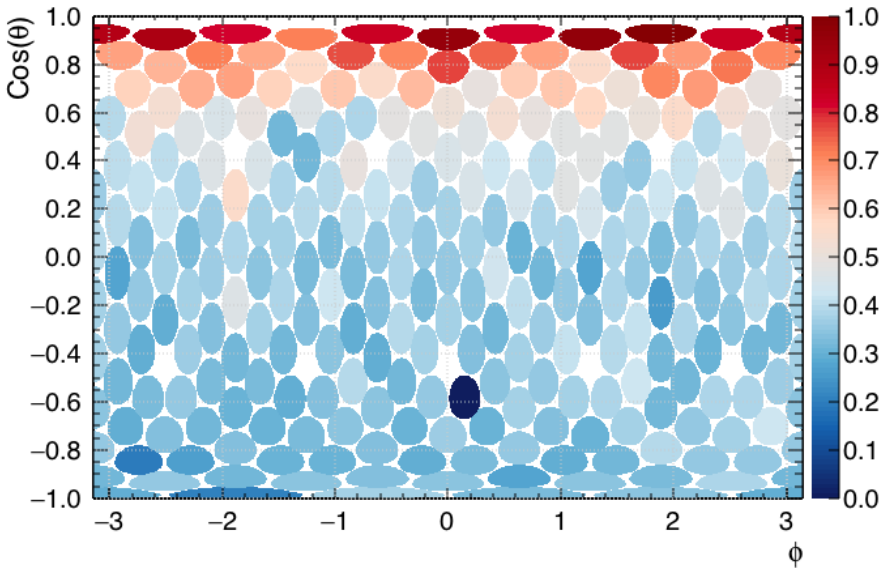


**Figure 4.11:** The distribution of peak charge (as defined in Figure 4.7) compared to the maximum peak charge for the 445 nm laser head in the (0,0,550 mm) position.

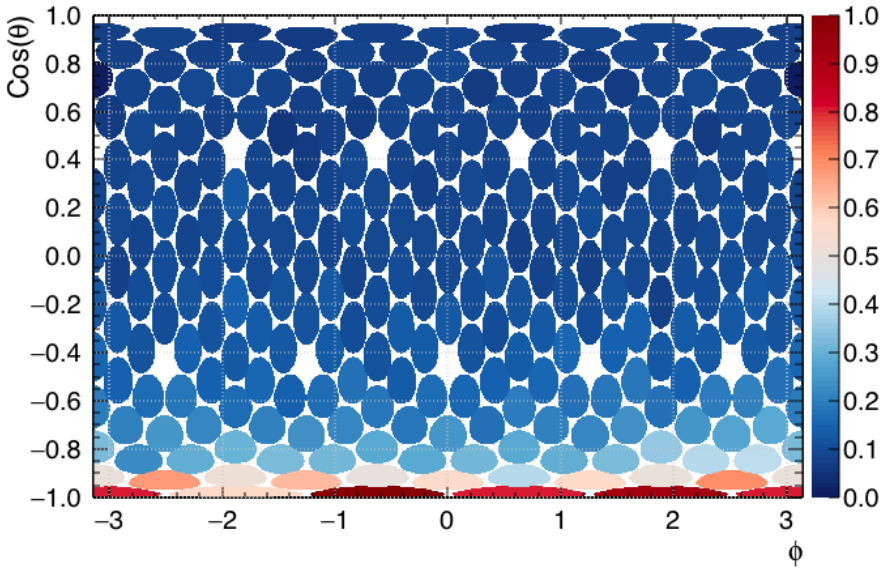


**Figure 4.12:** The distribution of peak charge (as defined in Figure 4.7) compared to the maximum peak charge for the 445 nm laser head in the (0,0,-550) position.

PMT 254. The first pulse was required to occur within the 20 ns laser pulse window. The second pulse was then assumed to be a dark hit, double pulse, or after-pulse. Figure 4.15 shows the charge versus time distribution of the second pulses relative to the first pulse time. Multiple PE after-pulses can be seen distributed around 2 and 7 to 8 $\mu$s, and a single

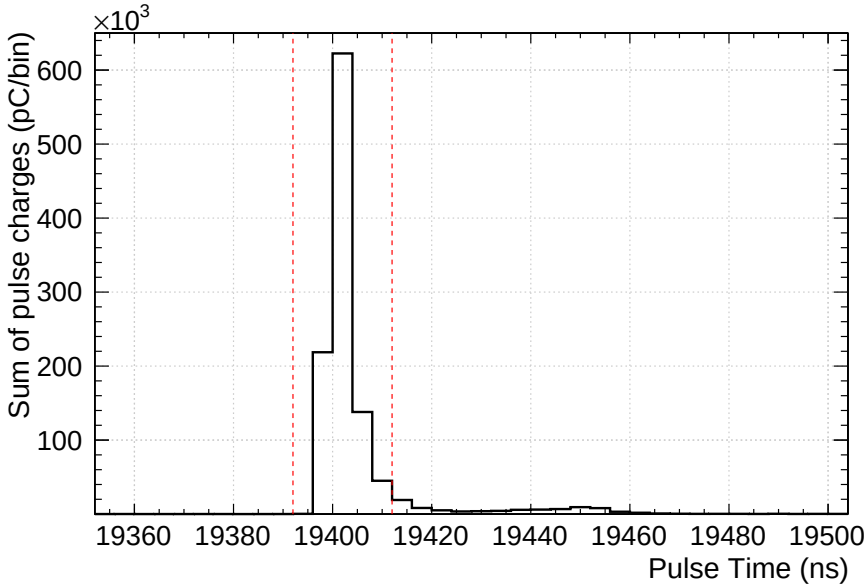


**Figure 4.13:** Pulse times weighted by pulse integral charge for a sample of the run, vertical lines show the laser pulse arrival window used in the study. The start of the arrival time region was set to 10 times the RMS of 100 ns region preceding the trigger time. The end was set to when the charge per bin dropped below 5% of the maximum.

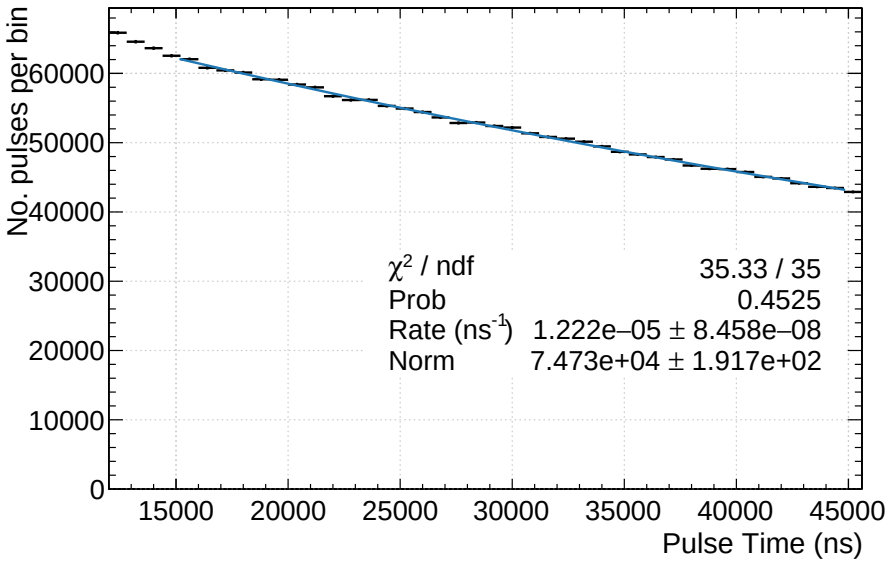


**Figure 4.14:** Consecutive pulse times for events with no laser hit. These times were fit with an exponential distribution to determine the noise rate in situ for this PMT. The noise rate was found to be $12.2 \pm 0.085$ kHz, reasonable for a room temperature PMT.

PE after-pulse distribution around 7 $\mu$s. Removing the expected single PE dark rate from this distribution will give a measure of the after-pulse rate. The earliest pulses seen are

due to double pulsing, this can be seen in Figure 4.16. The peak of this distribution sits at $50 \pm 2$ ns which agrees with the ex situ measurements described in chapter 3. These pulses do not contribute to the after-pulse PDF but show a possible study of the double-pulsing rate could be performed with the optical flask data. Using the after-pulse arrival time function set out in [131] for a quadratic PMT field:

$$t_{\text{arrive}} = \frac{4}{\pi}\sqrt{\frac{2m}{qV_0}}L \tag{4.2}$$

and applied to PMT 254, an estimation of the first after-pulse time can be calculated. Here $L = 10.5$ mm is the distance from the centre of the photocathode to the first dynode, and $V_0 = 535$ V is the potential difference between the photocathode and first dynode. Setting the mass and charge to that of an $H^+$ ion, and applying the correction factor set out in the paper, the earliest arrival time is expected to be distributed around 442 ns. Setting the earliest considered secondary pulse time to 300 ns minimises the double pulse contribution to the PDF and ensures all after-pulses are captured.

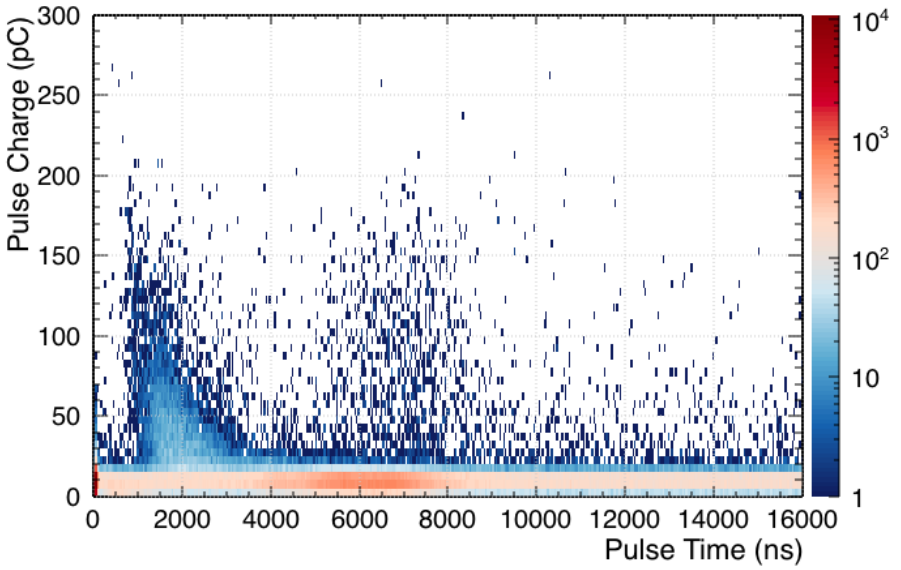


**Figure 4.15:** Charge versus time distribution of single pulses occurring after an initial pulse inside the laser pulse arrival window. Multiple PE after-pulses can be seen distributed around 2 and 6 to 8 $\mu$s.

Stipulating only two pulses per PMT waveform somewhat limits the sample size. However, it simplifies matters by removing the possibility of after-pulses of after-pulses being

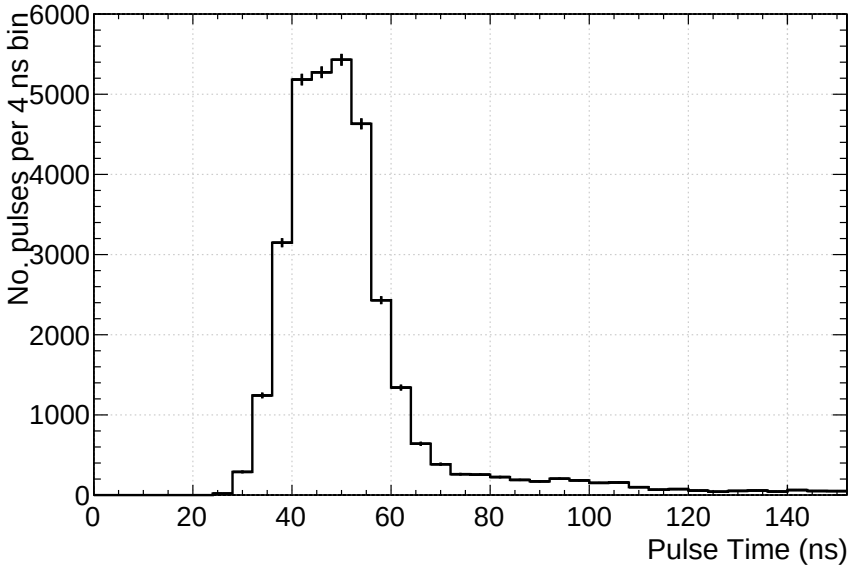


**Figure 4.16:** Distribution of secondary pulses corresponding to double pulses. The peak of this distribution sits at $50 \pm 2$ ns which agrees with the ex situ measurements described in chapter 3.

recorded. After-pulses caused by noise hits occurring earlier in the event are also disqualified. The distribution of dark hits in the resulting histogram is uniform in time with after-pulses superimposed. This can be seen in Figure 4.17 where the time distribution of pulses reverts to the flat dark hit PDF past 12 $\mu$s. Following [131] after-pulse arrival times were fit to Gaussian distributions:

$$N_{\text{pulse}}(t) = C_{\text{dark}} + \sum_{i=1}^{5} N_i \exp\left(-\frac{(t-t_i)^2}{2\sigma_i^2}\right) \tag{4.3}$$

where $i$ signifies an after-pulse ion type, and $t_i$ and $\sigma_i$ are the mean and standard deviation of the arrival times with normalisation $N_i$. $C_{\text{dark}}$ corresponds to the flat dark hit rate which was found to be $9.45 \pm 0.03$ ns$^{-1}$. Here 5 after-pulse components were included. The distribution in Figure 4.17 suggests more possible components in the 7 and 9 $\mu$s regions which could be included if confirmed with a larger sample size. With an accurate field map of the R5912-HQE PMTs these times could be attributed to the specific ion impurities present in each of the PMTs.

The after-pulse joint PDF can be created by simply removing the dark hit pedestal from

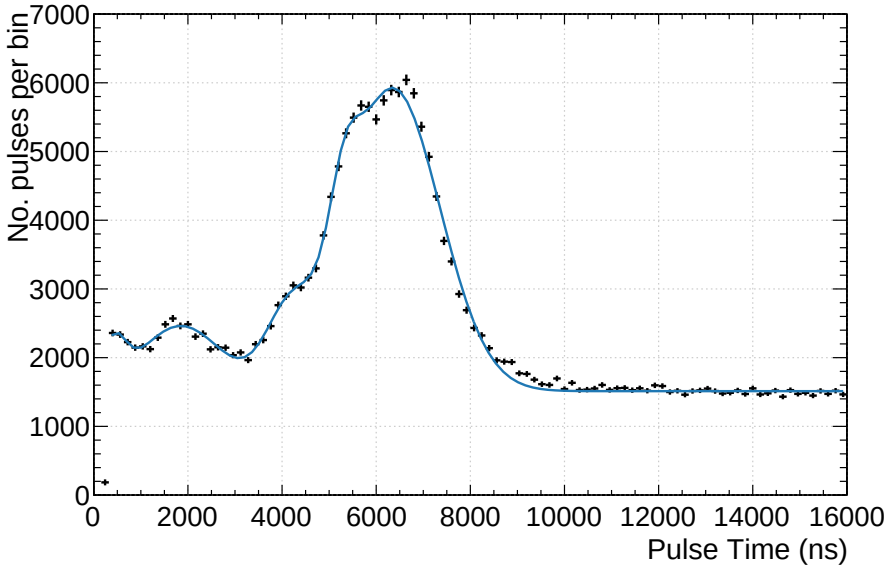


**Figure 4.17:** Distribution of secondary pulses fit with a sum of Gaussian distributions combined with a constant component corresponding to dark hits which appear as a flat distribution past 12 $\mu$s. Five after-pulse contributions were included. The distribution suggests more possible components in the 7 and 9 $\mu$s regions which could be included if confirmed with a larger sample size. The flat dark hit rate was found to be $9.45 \pm 0.03$ ns$^{-1}$

the charge versus time histogram of secondary pulses. The charge distribution of the initial laser pulse is shown in Figure 4.18. Here the 1 PE and 2 PE components of the charge distribution, discussed above, are included in red and green respectively. The single PE contribution, scaled to the expected number of dark hits, can then be removed from the charge-time distribution. This is shown in Figure 4.19 where the expected number of noise hits derived from the single PE distribution were subtracted from each bin keeping a minimum of 0 hits. If the number of pulses, $N_{\mathrm{p}}$, satisfied $\mathrm{Poisson}(N_{\mathrm{p}}; N_{\mathrm{dark}}^{\mathrm{expected}}) > 0.99$ the number of pulses was set to 0.

The after-pulse probability, $p_{\mathrm{ap}}$, can be determined by accounting for the fact that an after-pulse only occurs in the recorded data if a noise pulse does not and vice versa. The ratio of after-pulses to dark hits, $N_{\mathrm{AP}}/N_{\mathrm{DH}}$ is then

$$\frac{N_{\mathrm{AP}}}{N_{\mathrm{DH}}} = \frac{p_{\mathrm{ap}} \times \mathrm{Poisson}(0; R_{\mathrm{DH}}\, 200\,\mu s)}{(1 - p_{\mathrm{ap}}) \times \mathrm{Poisson}(1; R_{\mathrm{DH}}\, 200\,\mu s)}. \tag{4.4}$$

Here $\mathrm{Poisson}(n; R_{\mathrm{DH}}\, 200\,\mu s)$ is the Poisson probability of seeing $n$ dark hits given the mea-

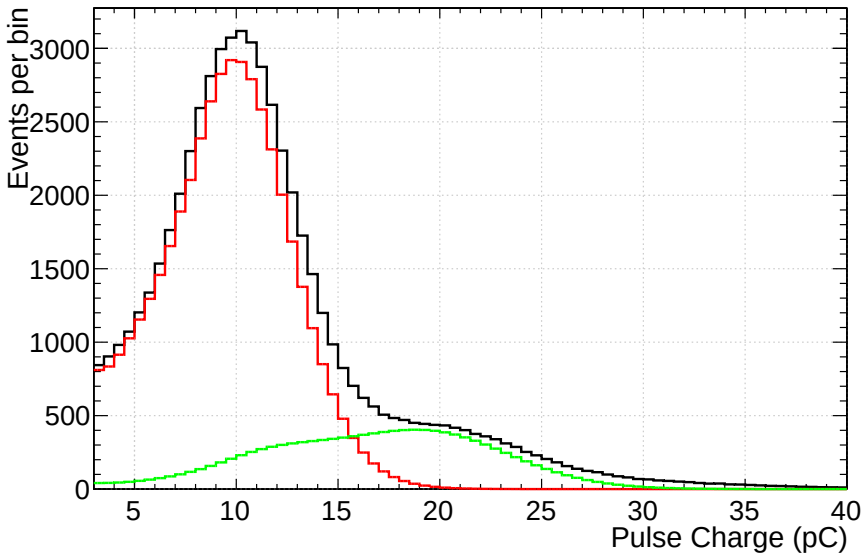


**Figure 4.18:** Distribution of charge for the initial laser pulse. The 1 PE and 2 PE double Polya distributions are shown in red and green respectively. The single PE distribution mean is $10.65 \pm 0.01$ pC.

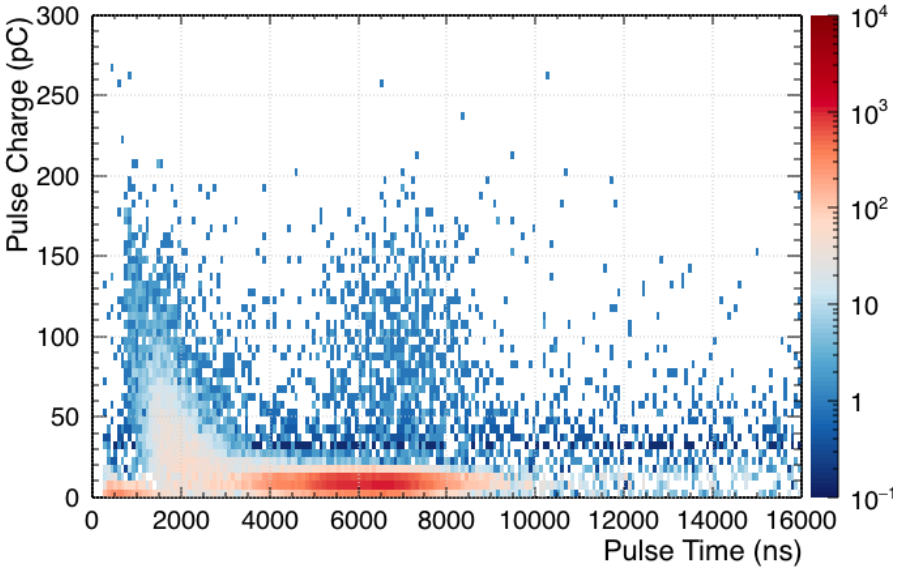


**Figure 4.19:** Charge versus time for secondary pulses with the single PE dark hit contribution removed. The structure due to after-pulses at early times is resolved and single PE pulses after 10 $\mu$s are greatly diminished.

sured dark rate $R_{\mathrm{DH}}$ over the 200 $\mu s$ event window. From this the after-pulse probability was found to be $0.11 \pm 0.002$, where the error is from uncertainty on the contributing fits propagated through with statistical error added in quadrature. The after-pulsing proba-

bility is that of a single photoelectron causing an after-pulse. Taking into account 2 PE pulses from the relative size of the second double polya contribution in Figure 4.18, 26.7%, we find $p_{\mathrm{ap}} = 0.083 \pm 0.001$ for single photoelectrons. This is close to the 7% after-pulse probability assumed in simulation. An ex situ measurement of the after-pulsing rate of PMT 254 is quoted as being 0.119. This is in agreement with the initial result, not taking into account the 2 PE contribution.

Across the detector, preliminary analysis using AARF data during commissioning shows the after-pulse probability can be anywhere between 2 and 10%. The after-pulsing tagging analysis described in chapter 3 takes probabilities for individual PMTs into account, so variation will not affect this result. This rate is dependent on the applied voltages of the PMTs, having a $\sqrt{V}$ dependence, and also the temperature, with the rate dropping by a few percent over the $\sim 60^{\circ}$ temperature drop as gaseous impurities adhere to the inner surface [132]. Monitoring of the PMTs while the detector is cooling will allow us to measure the change in after-pulsing rate. Pre-cooling data will be used to determine if there is a change in after-pulse rate over time. Once liquid argon is in the detector the overall event rate from $^{39}$Ar will make monitoring the single photon after-pulse rate and distribution extremely difficult. Extrapolation of data taken during commissioning will be necessary to determine after-pulse rates once the detector is filled.

Removal of the dark hits reveals much of the structure due to after-pulsing at low charge and early times. Past 10 $\mu$s single PE pulses have been removed almost entirely. The PDF used in simulation built from ex situ measurements contains much of the uniform structure attributed to dark hits. Removal of this uniform component should improve after-pulse tagging by differentiating it from the flat noise PDF already in use. Simulation and tagging of higher PE after-pulses using this PDF could make use of the multiple PE charge PDF, scaling each contribution to match the charge projection, to determine the number of PE produced. However, this will only be accurate in the range of a few PE, even with a larger sample, due to the variance of multiple PE charge distributions. The approach could be reformulated to draw only the charge from this distribution. A secondary multi PE likelihood PDF could then be included in the after-pulsing prior.

## 4.4 Conclusion

Overviews of the external radiation sources which will be deployed during detector operation were presented. Preliminary simulation of the neutron system shows a possible 2:1 signal-to-noise ratio of nuclear recoils to $^{39}$Ar background events. This will allow the nuclear recoil PSD to be measured to less than 1% statistical uncertainty per data run. The gamma source will populate the detector with electronic recoils of a known energy with a high signal-to-noise ratio. These will be used in combination with the known $^{39}$Ar spectrum to determine the light yield (energy scale) of the detector. The source will also be used to characterise position reconstruction resolution near the edge of the detector. The data rate of this source will have to be prescaled since it will be larger than the digitiser band width, as such, statistical error will not be a limiting factor.

The AARF system can cover the detector with photons of a wavelength close to the TPB re-emission spectrum. It will be used to measure PMT performance during the lifetime of the experiment and to monitor changes, such as after-pulse rate, during the cooling phase of the detector. The after-pulse rate has a direct affect on PSD, under-counting after-pulses for a given ROI by 7% could increase leakage by a factor 70. The optical flask, used in the detector after TPB deposition, has provided data on the detector response to three different wavelengths of centrally distributed light. The non-uniformity of source distribution will have to be decoupled before limits can be set on relative PMT efficiencies and light guide attenuation lengths, for example. A study of after-pulsing in PMT 254 was performed. The after-pulse rate was found to be close to that assumed in simulation. The more structured after-pulse PDF, particularly in the single PE region, should enhance tagging efforts.

Relative timing offsets of each of the electronics channels will be determined on a run by run basis using a PPG. Fitting of the PPG function to determine channel timing returns sub-nanosecond resolution of the timing offsets. This is more than adequate to ensure accuracy in time based analyses such as pulse shape discrimination.

# Chapter 5

# The Dark Matter Limit

*Have you found it yet?*

Jennifer Wright

In this chapter the Poisson method originally used in the projected sensitivity of DEAP-3600 is revisited with updated simulation and discrimination variables. The impact of the work in this thesis on the experimental sensitivity, including modelling and mitigating the effect of after-pulsing, as well as using information from the scintillation time distribution with the $L_{\text{recoil}}$ variable, will be quantified. Finally, a likelihood approach to setting a WIMP-nucleon cross section limit, including $L_{\text{recoil}}$, as well as known backgrounds, is described.

## 5.1 Limit Setting

The initial projected 90% confidence level sensitivity for DEAP-3600 was calculated using the Poisson method [133]. That is, a cross section value, $\sigma_{\chi\text{n}}^{\text{up}}$, was determined for each mass such that the number of expected WIMP like events solves

$$\alpha(\sigma_{\chi\text{n}}^{\text{up}}) = \exp(-N_{\text{exp}}) \sum_{m=0}^{N_{\text{obs}}} \frac{N_{\text{exp}}^{m}}{m!} = 0.1, \tag{5.1}$$

where $N_{\text{obs}}$ is the observed number of events. Figure 5.1 shows the result of this method for the original projected characteristics of DEAP-3600 (dashed line) along with updated sensitivities from simulation. A 120 to 240 PE window, at 8 PE/keV$_{\text{ee}}$, was used which was motivated by the ability of the $F_{\text{prompt}}$ variable to reject background events with a 50% nuclear recoil efficiency. A three year exposure was assumed with a 1000 kg fiducial mass corresponding to a radius of 55 cm. The specification of $< 0.6$ background events over the three years yields a greater than 88% chance of a background free dataset, which was assumed.

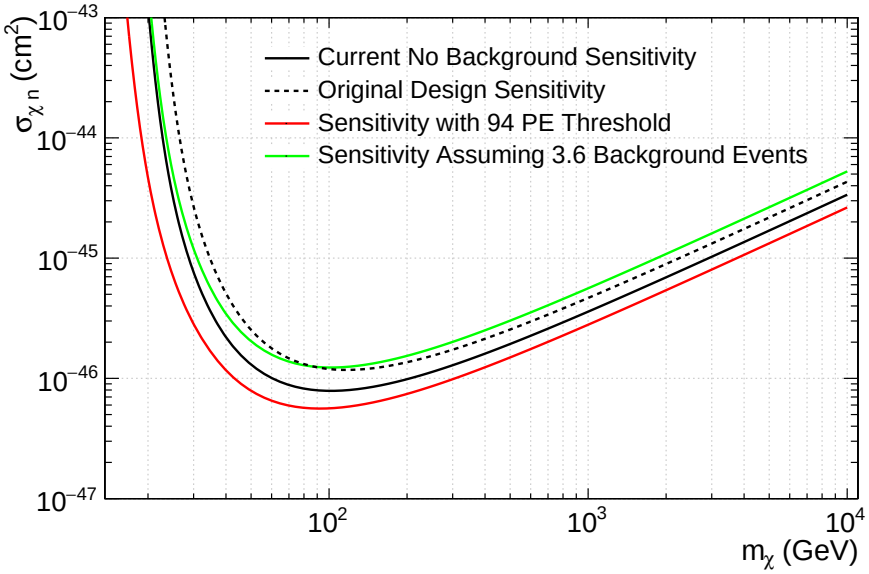


**Figure 5.1:** The original projected characteristics of DEAP-3600 (dashed), and the current projected sensitivity from simulation (black). Improvement on the original sensitivity is due to the increased light yield. The sensitivity when the major background to the dark matter search, alpha events in the neck, is included is also plotted (green). The sensitivity gained from the increase in light yield is removed by the presence of this background. Finally the sensitivity taking the PE threshold to be 94 PE is plotted (red). This assumes the $^{39}$Ar background dominates and the threshold can be safely lowered. The increased window improved the limit from $7.7 \times 10^{-47}$ cm$^2$ to $5.6 \times 10^{-47}$ cm$^2$, or 27%.

The detector response function used to determine the dark matter spectrum was built from a Monte-Carlo simulation of $7.5 \times 10^6$ nuclear recoil events distributed uniformly throughout the detector with a flat energy spectrum between 0 and 300 keV. The resulting PE spectrum was then re-weighted by the expected rate at the corresponding nuclear recoil energy for each value of $\sigma_{\chi\text{n}}$ and $m_\chi$ being investigated. That is, an n-tuple of nuclear recoil events was looped through which contained information about the true energy and

position of each scatter along with reconstructed values. The weight of each event was then calculated using the true energy and placed in a PE histogram. This histogram was then integrated to obtain the expected number of events. The statistical uncertainty is 0.17%. Figure 5.2 shows the PE spectra of 40 and 100 GeV WIMPs with a wimp-nucleon cross-section of $10^{-45}\,\mathrm{cm}^2$. A position reconstruction cut was applied using the Shellfit algorithm. A 50% total acceptance region was selected in both cases, so the choice of pulse shape discrimination (PSD) variable ($L_{\mathrm{recoil}}$ in the new limit case) does not contribute to the change in the sensitivity projection.

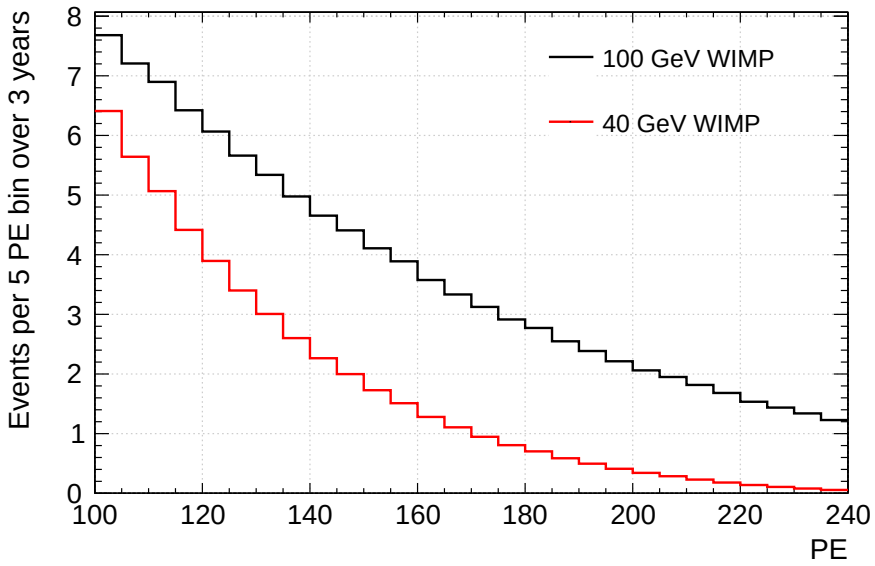


**Figure 5.2:** WIMP recoil spectra in terms of PE for 40 and 100 GeV masses. A uniform nuclear recoil distribution was generated and re-weighted according to the rates of its corresponding interactions energies.

The current projected sensitivity from simulation is also plotted in Figure 5.1 (black line), with the nominal PE window. Improvement on the original limit is due to the increased light yield; lower energy, higher rate, WIMP events appear higher in the PE spectrum. This is illustrated in Figure 5.3 which shows the sensitivity for various light yields. An increased light yield results in a logarithmic increase in the peak sensitivity.

The major background to the dark matter search, alpha events in the neck, is assumed in the green line on Figure 5.1. This assumes no uncertainty on the number of background events. The cross section was scaled such that, if it were any higher, it would produce an

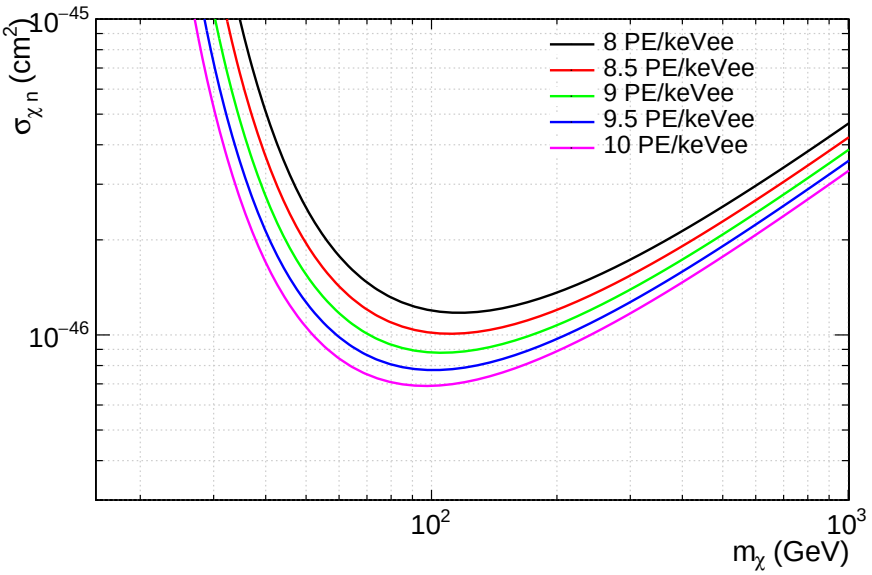


**Figure 5.3:** Zero background sensitivities given various light yields. An increased light yield results in an increase in the peak sensitivity.

excess of events above background at 90% confidence level. Here the PE window was set to 120 to 240 PE. The sensitivity gained from the increase in light yield is removed by the presence of this background.

Finally, the sensitivity when using the full PE window which can be obtained using the $L_{\text{recoil}}$ variable is plotted in red. This uses the 94 PE threshold, where after-pulses are removed, which keeps the $^{39}$Ar event rate below the design constraint of 0.2. Lowering the threshold results in a considerable gain in sensitivity. However, this is only in reference to $^{39}$Ar events. The effect this lower threshold will have on other backgrounds has not yet been ascertained.

Figure 5.4 shows the projected 90% confidence level limit for a 100 GeV WIMP as a function of the threshold PE value. The increased window improved the limit from $7.7 \times 10^{-47}\,\text{cm}^2$ to $5.6 \times 10^{-47}\,\text{cm}^2$, or 27%. The current simulated light yield of 9.3 PE/keV$_{\text{ee}}$ is higher than the 8 PE/keV$_{\text{ee}}$ originally assumed. The light yield with after-pulsing included is higher still, however, this extra light does not correspond to an interaction process in the detector. Figure 5.5 shows sensitivity curves using thresholds from Table 3.1. Here the equivalent sensitivity if you did not remove after-pulses is plotted as a

corresponding dashed line. The trade off can be seen between reducing the light yield and improving the PSD by removing after-pulses. At a given threshold leaving after-pulses in will improve the light yield. However, removing after-pulses allows the threshold to be lowered, substantially improving the sensitivity.

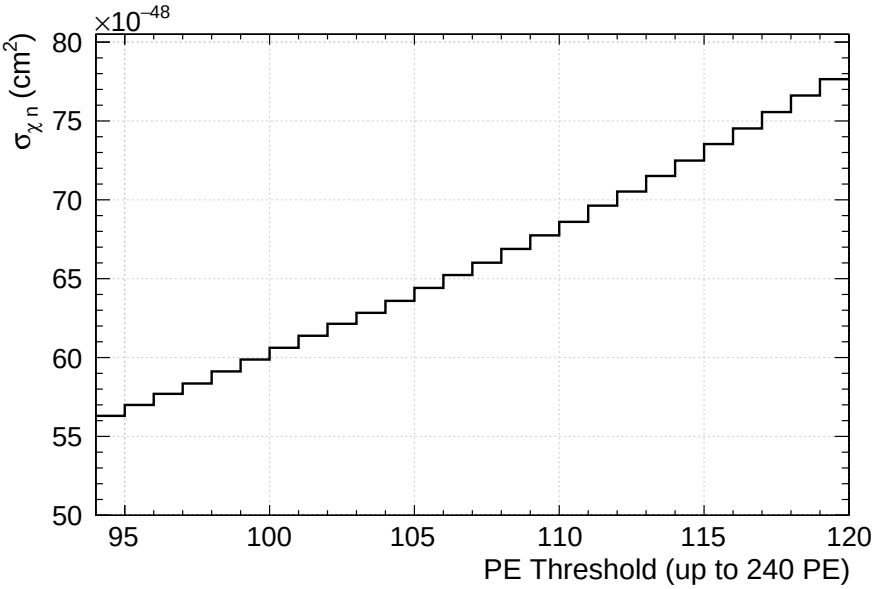


**Figure 5.4:** The projected 90% confidence level limit for a 100 GeV wimp as a function of the threshold PE value.

### 5.1.1 Towards a Likelihood Fit

The basic Poisson limit approach is to define a region of interest in the detector parameter space and perform a counting experiment. As such, the position of events inside the parameter space and the shape of the signal and background distributions is not taken into account. Other approaches, such as the maximum patch and optimum interval method, incorporate dark matter signal information producing more sensitive limits [134][135]. However, these methods are designed only to produce an upper limit, and do not move easily into defining a discovery. A profile likelihood based approach used by the XENON collaboration was shown to produce a more stringent limit than previously published [136]. Motivated by this, a preliminary framework for a full likelihood based analysis of DEAP-3600 is discussed here.

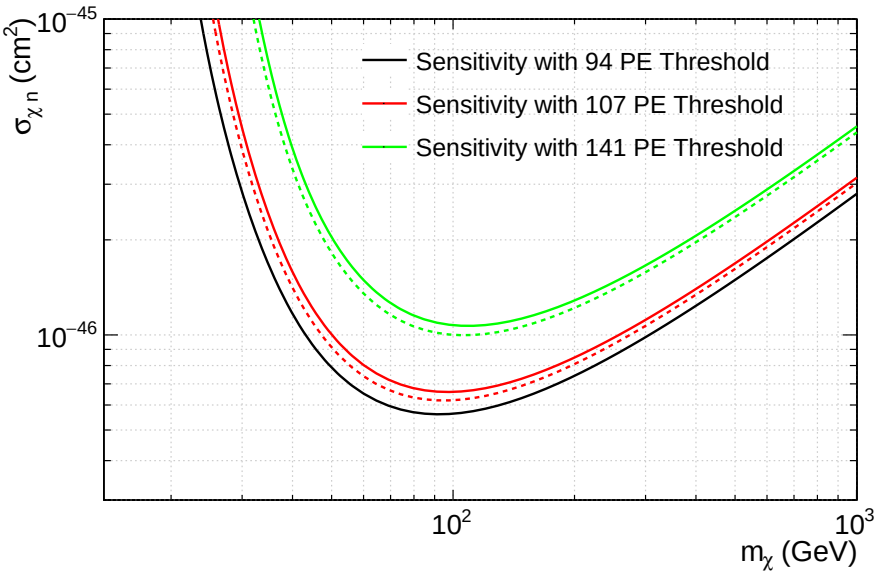


**Figure 5.5:** Sensitivity curves using thresholds from Table 3.1 (solid) with the corresponding sensitivity if after-pulses are included (dashed). Here the trade off can be seen between reducing the light yield and improving the PSD using the after-pulse removal technique. At a given threshold leaving after-pulses in will improve the light yield. However, removing after-pulses allows the threshold to be lowered substantially improving the sensitivity.

### Nuisance Parameters

With the Poisson limit approach it is assumed there is no uncertainty on the background rate. Including systematics in a cut and count search can be achieved via a simple version of the full likelihood described below. Following [137] a profile likelihood ratio test statistic $\lambda(\sigma_{\chi\mathrm{n}}|m_\chi)$ (where $\sigma_{\chi\mathrm{n}}$ is the test cross section for a given mass $m_\chi$) could be built, where

$$\lambda(\sigma_{\chi\mathrm{n}}|m_\chi) = \frac{\mathcal{L}(\sigma_{\chi\mathrm{n}}, \hat{\hat{\theta}})}{\mathcal{L}(\hat{\sigma}_{\chi n}, \hat{\theta})} \tag{5.2}$$

$$= \frac{\mathrm{Poisson}\{N_{\mathrm{obs}}|N^{\mathrm{exp}}(\sigma_{\chi\mathrm{n}}, \hat{\hat{\theta}})\}}{\mathrm{Poisson}\{N_{\mathrm{obs}}|N^{\mathrm{exp}}(\hat{\sigma}_{\chi\mathrm{n}}, \hat{\theta})\}}. \tag{5.3}$$

Here $\theta \to \vec{\theta}$ is the set of nuisance parameters. The numerator is the conditional maximum-likelihood estimator for the nuisance parameters, and the denominator is the maximised unconditional likelihood where both the cross section and nuisance parameters are their respective maximum likelihood estimators. The nuisance parameters are thus "profiled

out". A test statistic for an upper limit can then be defined as

$$q_\sigma = \begin{cases} -2\ln\lambda(\sigma) & \hat{\sigma} \leq \sigma, \\ 0 & \hat{\sigma} > \sigma. \end{cases} \tag{5.4}$$

$q_\sigma$ is set to zero for values $\hat{\sigma} > \sigma$ because when setting an upper limit values greater than the hypothesised cross section would not be considered more incompatible with the data. The p-value for a hypothesised $\sigma$ given an observed $q_\sigma^{\text{obs}}$ is then calculated via

$$p_\sigma = \int_{q_\sigma^{\text{obs}}}^{\infty} f(q_\sigma|\sigma)\mathrm{d}q_\sigma \tag{5.5}$$

where $f(q_\sigma|\sigma)$ is the distribution of test statistics given the hypothesised $\sigma$. For each nuisance parameter a constraint term can then be added to the likelihood. In DEAP-3600 the background model is still being fully characterised, however, some systematics will dominate, such as:

- Energy scale or light yield. This is fundamental to the analysis, as it determines the amount of energy deposited, and the discrimination power of the PSD. Constraining this value will be done in multiple ways. One of which is through the use of $^{39}$Ar by rescaling the expected energy distribution to fit the data. This will be done in conjunction with the external gamma source to constrain the light yield at higher energy. Surface alphas, if appropriately tagged, can also be used as a source of known energy.

- Energy resolution. The energy resolution can also be constrained using the gamma source, $^{39}$Ar, and surface alphas. Since alpha decays are mono energetic they will provide a source with a specific energy in the argon volume itself.

- Quenching factor. Literature values will be used to constrain this term along with possible in situ methods.

- Position resolution. Leakage into the fiducial volume due to mis-reconstruction of events is currently the dominant background in simulation. As mentioned in chapter

4 the uniformly distributed $^{39}$Ar spectrum will give a handle on the position resolution. Each radial bin has some expected rate, deviations from this will indicate a bias and give a handle on the resolution. This will be combined with gamma source data from the circular calibration port. The TPB uniformity will also affect this measurement and will be determined using the optical calibration sources.

- Normalisation of backgrounds. The expected number of backgrounds has a direct result on the sensitivity. This value will be constrained from assays of the various detector components combined with side band studies of the in situ data.

The above will cause a notable change in the value of $N_{\text{exp}}$ and will need to be fully characterised. In the full likelihood approach signal and background distributions will be modelled as functions of these nuisance parameters. Below, the galactic escape velocity is used as a test case.

The nominal run plan for the experiment is that the initial 30 days will be un-blind. Therefore, I will discuss the likelihood analysis development with respect to dark matter sensitivity in this initial time period. With a 30 day, 1000 kg exposure $^{39}$Ar is the dominant background. A likelihood function is built including the WIMP ($PE$, $L_{\text{recoil}}$), and $^{39}$Ar ($PE$, $L_{\text{recoil}}$) PDF with after-pulses removed in reconstruction. Both WIMPs and $^{39}$Ar events are expected to be distributed uniformly throughout the target volume. As such they have the same reconstructed position distribution. A single radial position PDF is included for both distributions and as such is not expected to constrain the fit. Further development of the method to include $\alpha$ backgrounds, for example, will require individual position PDFs. Improved position reconstruction algorithms may also make including a full 3 dimensional PDF viable.

The PDFs were built using Monte-Carlo simulation in RAT. $2.7 \times 10^7$ low energy $^{39}$Ar events were generated over approximately 500 thousand CPU hours. This number is equivalent to $1 \times 10^8$ full spectrum $^{39}$Ar events. The expected number of $^{39}$Ar events in the first 30 days is $9.3 \times 10^9$. Following [136] and [137] the preliminary likelihood is given

by

$$\mathcal{L} = \mathcal{L}_{\mathrm{d}}(\sigma; v_{\mathrm{esc}}; m_{\chi})\mathcal{L}_{\mathrm{v}}(v_{\mathrm{esc}}), \tag{5.6}$$

where $\sigma$ is the hypothesised WIMP-nucleus cross section for a given WIMP mass $m_{\chi}$ and $v_{\mathrm{esc}}$ is the galactic escape velocity. Here $\mathcal{L}_{\mathrm{d}}$ is an unbinned extended likelihood containing signal and background PDFs along with the Poisson term described above.

$$\mathcal{L}_{\mathrm{d}} = \mathrm{Poisson}(N_{\mathrm{obs}}|N^{\mathrm{exp}}) \times \left( \frac{N_{\mathrm{DM}}^{\mathrm{exp}}}{N^{\mathrm{exp}}} f_{\mathrm{DM}}(PE, L_{\mathrm{recoil}}) + \frac{N_{\mathrm{Ar}}^{\mathrm{exp}}}{N^{\mathrm{exp}}} f_{\mathrm{Ar}}(PE, L_{\mathrm{recoil}}) \right) \times f(\vec{R}), \tag{5.7}$$

where $N_{\mathrm{DM}}^{\mathrm{exp}}$ and $N_{\mathrm{Ar}}^{\mathrm{exp}}$ are the expected number of dark matter and $^{39}$Ar events respectively with $N^{\mathrm{exp}} = N_{\mathrm{DM}}^{\mathrm{exp}} + N_{\mathrm{Ar}}^{\mathrm{exp}}$. $f_{\mathrm{DM}}$ and $f_{\mathrm{Ar}}$ are the joint $PE, L_{\mathrm{recoil}}$ PDFs, and $f(\vec{R})$ is the radial position distribution. The $f_{\mathrm{DM}}(PE, L_{\mathrm{recoil}})$ distribution is shown in Figure 5.6. Each PE bin is scaled to the expected number in Figure 5.2. The $L_{\mathrm{recoil}}$ spectra for each PE are then fit with a Gaussian, with which the likelihood was evaluated, above the mean of the histogram falling into the region of interest, an example of which is shown in Figure 5.8 for $^{39}$Ar events at 100 PE. A Gaussian distribution is a good approximation to the high PSD spectrum in this low statistics case. A full functional form will have to be derived for the 3 year limit in lieu of a sufficiently large Monte-Carlo data set. The radial PDF is shown in Figure 5.9, this was fit with a cubic spline before being included in the likelihood.

The galactic escape velocity is constrained by

$$\mathcal{L}_{\mathrm{v}}(v_{\mathrm{esc}}) = f(v_{\mathrm{esc}}|v_{\mathrm{med}}), \tag{5.8}$$

where the probability distribution of the escape velocity $f(v_{\mathrm{esc}}|v_{\mathrm{med}})$ is the same as that used by XENON from [138], shown in Figure 7. This gives asymmetric 90% CL bounds on the escape velocity of $498\,\mathrm{km/s} < \mathrm{v_{esc}} < 608\,\mathrm{km/s}$ with the median value being $v_{\mathrm{med}} = 544\,\mathrm{km/s}$. $v_{\mathrm{esc}}$ is the only nuisance parameter, with $N_{\mathrm{DM}}^{\mathrm{exp}}$ being set by the mass and cross section, and $N_{\mathrm{Ar}}^{\mathrm{exp}}$ assumed to be known [74]. Side band $^{39}$Ar event statistics will be of order $2.5 \times 10^9$ allowing the rate to be measured accurately. For other sources of background there will be uncertainties on the in situ data which will be included in the

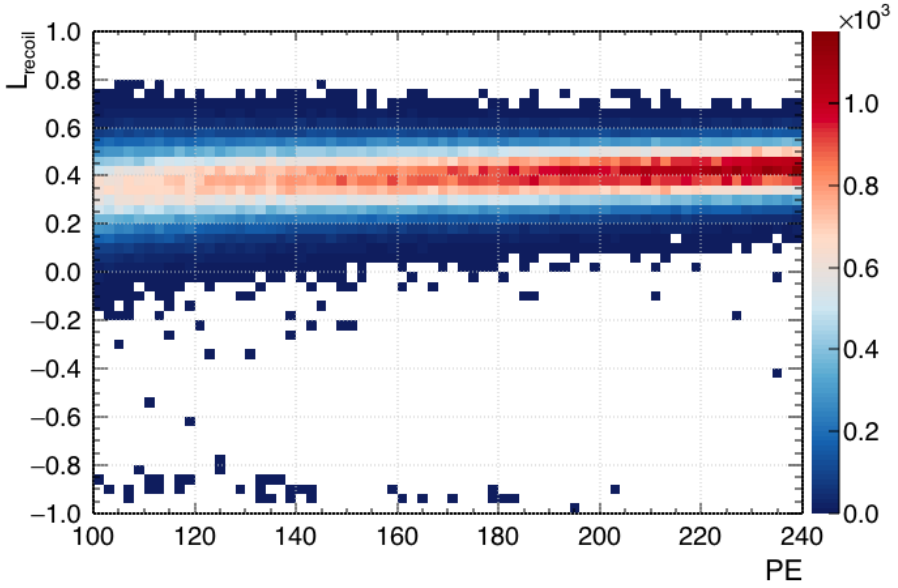


**Figure 5.6:** The $L_{\text{recoil}}$ vs PE distribution for nuclear recoil events. Each PE column is scaled to the expected number in Figure 5.2.

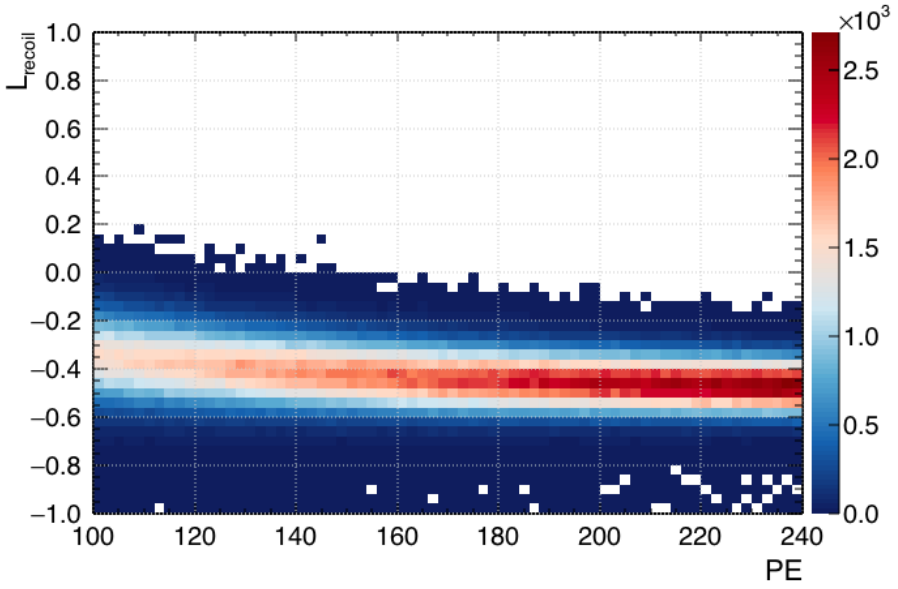


**Figure 5.7:** The $L_{\text{recoil}}$ vs PE distribution for $^{39}$Ar events. Each PE bin is scaled to the expected number of background events in the distribution determined from the Monte-Carlo integral of the fraction of events within the region of interest.

likelihood fit, along with constraints from data outside the region of interest. The profile

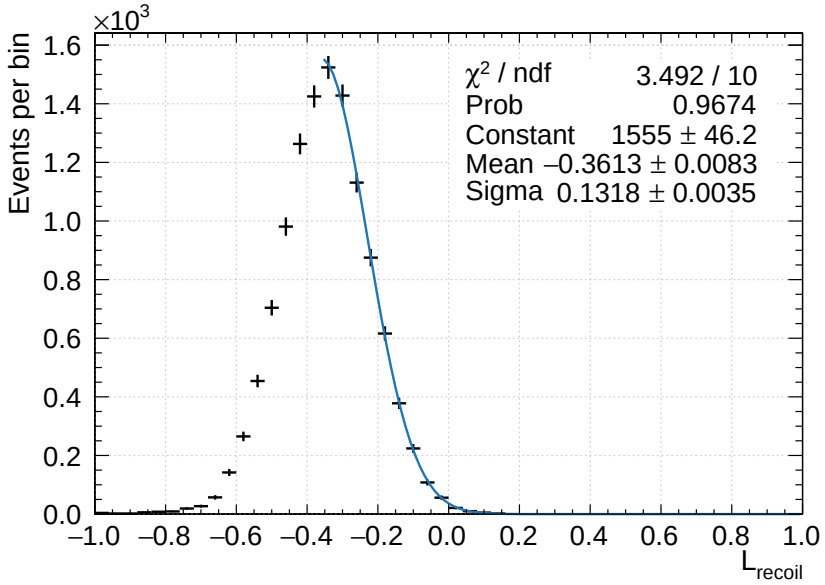


**Figure 5.8:** $L_{\mathrm{recoil}}$ distribution fit with a Gaussian function from the mean of the histogram falling into the region of interest.

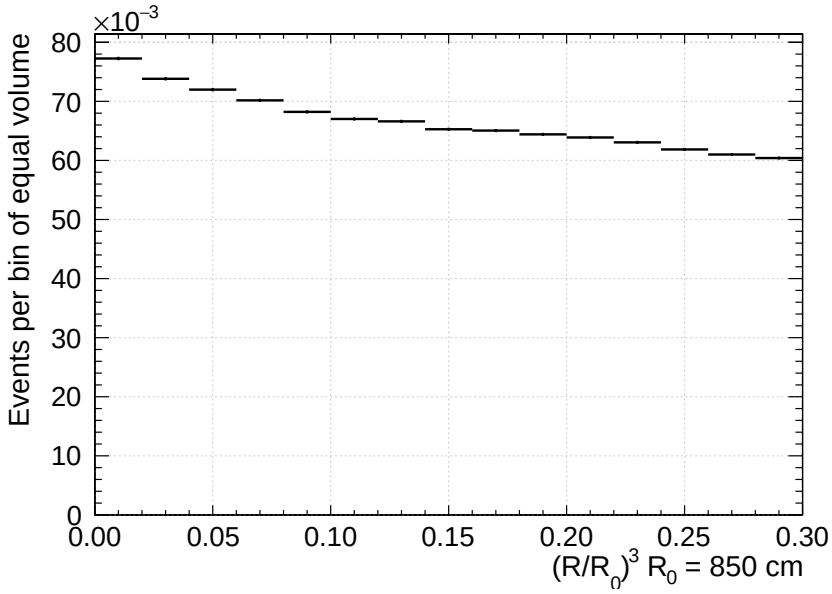


**Figure 5.9:** Radial distribution PDF in bins of equal volume. This histogram was fit with a cubic spline before being included in the likelihood.

likelihood ratio is then given as

$$\lambda(\sigma) = \frac{\mathcal{L}(\sigma; \hat{\hat{v}}_{\mathrm{esc}})}{\mathcal{L}(\hat{\sigma}; \hat{v}_{\mathrm{esc}})}, \tag{5.9}$$

where the numerator is the conditional maximum-likelihood estimator of $v_{\rm esc}$, and the denominator is the maximised unconditional likelihood where both $v_{\rm esc}$, and $\sigma$ are their maximum likelihood estimators. A test statistic for the upper limit is then defined as in Equation 5.4. In testing this method recourse was made to Monte-Carlo simulation to build the distribution $f(q_\sigma|\sigma)$. This distribution asymptotically becomes a chi square distribution for one degree of freedom as the number of observations increases. Approximate distributions can then be built such that Monte-Carlo is not required [137]. The statistical package RooFit [139] was used to build the likelihood function and minimise it using the MIGRAD method. Five WIMP masses were chosen and their corresponding cross sections were scanned through. 500 pseudo-experiments were then performed at each point with the expected number of events Poisson fluctuated and distributed within the region of interest within $100 < PE < 240$, $L_{\rm recoil} > 0.41$ (representing 50 % nuclear recoil acceptance to compare with the nominal case), and $\vec{R} < 55\,{\rm cm}$. $q_{\rm obs}$ was then calculated for 0 observed events. Figure 5.10 shows the 90% confidence level produced using this method. The error band reflects the statistical error on the Monte-Carlo integration. This is plotted together with the Poisson limit assuming no background events. The agreement shows the efficacy of the likelihood approach in this simple starting case, where the 0 background limit is reproduced with $^{39}$Ar included in the calculation. This method will be further developed to include all background PDFs, and systematic uncertainties on detector response and the rates of the backgrounds. The region of interest will also be optimised, initially by maximising the rate of signal/$\sqrt{\rm signal + background}$. This will be used in the simple Poisson likelihood where the rate of events is profiled over. With the full likelihood, cuts could be relaxed. The fiducial volume could be increased, for example, while retaining knowledge of the background distributions. With natural argon a computational limit is reached, however, due to $^{39}$Ar events. The large number of possible $^{39}$Ar events in the data set will make fast likelihood evaluations an impossibility.

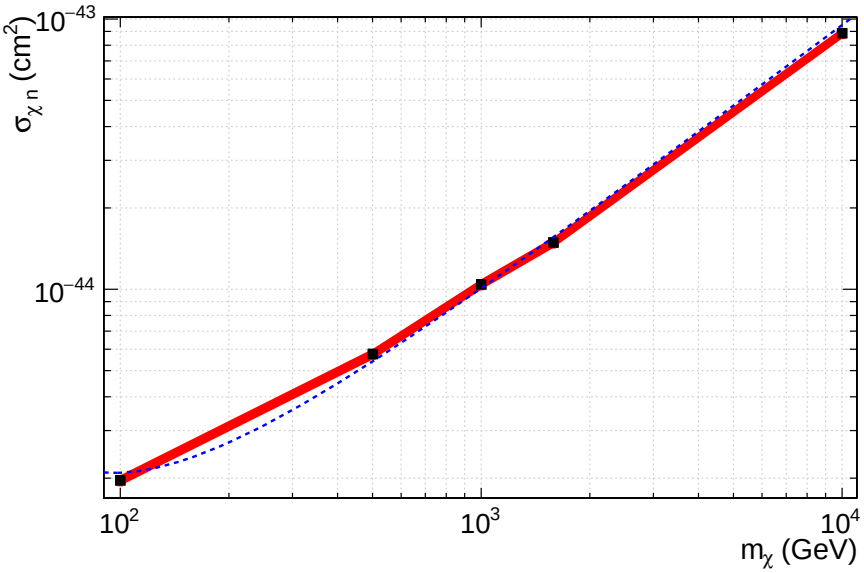


**Figure 5.10:** The 90% confidence limit produced using the profile likelihood based approach. Both WIMPs and $^{39}$Ar events were included distributed around PE, $L_{\text{recoil}}$, and $\vec{R}$. Five mass points were chosen (black squares) and a scan through the corresponding cross-sections was performed. For each point 500 MC pseudo-experiments were performed and the p-value calculated. The error band reflects the statistical error on the Monte-Carlo integration. This is plotted together with the Poisson limit assuming no background events. The agreement shows the efficacy of the likelihood approach in this simple starting case.

## 5.2 Conclusion

The DEAP-3600 detector will begin its first data taking towards the middle of 2016. It was originally projected to produce a leading spin-independent WIMP-nucleon scattering sensitivity of $1.1 \times 10^{-46}\,\text{cm}^2$. It was found that after-pulses, currently simulated at a rate of 7% per PE, pushed the distributions of nuclear and electronic recoils closer together, diminishing discrimination power by a factor of 70. The after-pulse tagging procedure presented in this work combined with the use of improved PSD variables will allow the energy threshold of the detector to be lowered, improving its sensitivity. Removal of after-pulses also prevents low energy events, which will have a broad PSD distribution, from being artificially pushed into the energy region of interest. Keeping to the design specified 50% nuclear recoil acceptance background rate for $^{39}$Ar, the threshold could be lowered from 120 PE to 94 PE. This corresponds to an increase in the sensitivity of the experiment from $7.7 \times 10^{-47}\,\text{cm}^2$ to $5.6 \times 10^{-47}\,\text{cm}^2$, a 27% improvement. A procedure to measure

the after-pulsing rate and distribution was developed using the in situ calibration data. A measurement of PMT 254 was found to match with ex situ measurements and yielded a similar after-pulse charge-time distribution to the ex-situ average. Characterisation of after-pulsing in each of the experiment's 255 inner PMTs will further improve tagging and removal of this PMT effect.

A combined profile likelihood fit is being developed. With calibration data and side band studies, all of the known backgrounds to the experiment will be included and systematics characterised. Improved position reconstruction algorithms will allow for a full three dimensional mapping of the detector, constraining surface and neck backgrounds. The current projected limit for DEAP-3600 with respect to its $^{39}$Ar background rate is $5.6 \times 10^{-47}\,\mathrm{cm}^2$, a 48% improvement on the initial design specifications, 27% of which is due to a lower threshold energy of 40.4 $\mathrm{keV_r}$. This is the sensitivity improvement in the most optimistic case, in which there is no increase in other background sources due to a lowered threshold value and surface alphas from the neck are ignored. Techniques in both hardware and software are being developed to mitigate neck events. In lieu of that, the 90% confidence level sensitivity given 3.6 background events due to alphas in the neck sits at the design specified $1.1 \times 10^{-46}\,\mathrm{cm}^2$ despite the significant improvement in expected light yield.

# References

[1] Planck Collaboration. Planck 2015 results. i. overview of products and scientific results. *Astronomy & Astrophysics*, 2015.

[2] Matts Roos. Dark matter: The evidence from astronomy, astrophysics and cosmology. 2010.

[3] L. Volders. Neutral hydrogen in m33 and m101. *Bulletin of the Astronomical Institutes of the Netherlands*, 1959.

[4] V. C. Rubin et al. Rotation velocities of 16 sa galaxies and a comparison of sa, sb, and sc rotation properties. *The Astrophysical Journal*, 289:81–98, 1985.

[5] V. C. Rubin et al. Rotation of the andromeda nebula from a spectroscopic survey of emission regions. *The Astrophysical Journal*, 159:379, 1970.

[6] K.G Begeman, A. H. Broeils, and R. H. Sanders. Extended rotation curves of spiral galaxies: dark haloes and modified dynamics. *Royal Astronomical Society*, 249:523 – 537, 1991.

[7] S. D. M. White, J. F. Navarro, A. E. Evrard, and C. S. Frenk. The baryon content of galaxy clusters: a challenge to cosmological orthodoxy. *Nature*, 366:429 – 433, 1993.

[8] D. Harvey, R. Massey, T. Kitching, A. Taylor, and E. Tittley. The non-gravitational interactions of dark matter in colliding galaxy clusters. *Science*, 347:1462 – 1465, 2015.

[9] P. A. R. Ade et al. Planck early results. i. the planck mission. *Astronomy & Astrophysics*, 536(A1), 2011.

[10] W. Hu. Lecture notes on cmb theory. *arXiv:0802.3688 [astro-ph]*.

[11] D. Croton. Damn you, little h! (or, real-world applications of the hubble constant using observed and simulated data). *arXiv:1308.4150 [astro-ph.CO]*, 2013.

[12] S. Sarkar. Big bang nucleosynthesis and physics beyond the standard model. *Reports on Progress in Physics*, 59(12), 1996.

[13] P. A. R. Ade et al. Planck 2015 results. xiii. cosmological parameters. *Astronomy & Astrophysics*, 2015.

[14] M. Milgrom. A modification of the newtonian dynamics as a possible alternative to the hidden mass hypothesis. *Astrophysical Journal*, 270:365 – 370, 1983.

[15] G. W. Angus1, B. Famaey, and H. S. Zhao. Can mond take a bullet? analytical comparisons of three versions of mond beyond spherical symmetry. *MNRAS*, 371(1):138–146, 2006.

[16] S. S. McGaugh. A tale of two paradigms: the mutual incommensurability of $\lambda$cdm and mond. *Can. J. Phys.*, 93(2):250–259, 2015.

[17] L. D. Duffy and K. van Bibber. Axions as dark matter particles. *New Journal of Physics*, 11, 2009.

[18] J. E. Kim. Light pseudoscalars, particle physics and cosmology. *Physics Reports*, 150, 1987.

[19] C. A. Baker et al. An improved experimental limit on the electric-dipole moment of the neutron. *Phys. Rev. Lett.*, 97, 2006.

[20] R. D. Peccei and H. R. Quinn. Cp conservation in the presence of pseudoparticles. *Phys. Rev. Lett.*, 38, 1977.

[21] J. Ipser and P. Sikivie. Can galactic halos be made of axions? *Phys. Rev. Lett.*, 50(12), 1983.

[22] Q. Yang. Axions and dark matter. *arXiv:1509.00673 [hep-ph]*, 2015.

[23] L. J. Rosenberg. Dark-matter qcd-axion searches. *Proceedings of the National Academy of Sciences*, 2015.

[24] R. J. Gaitskell. Direct detection of dark matter. *Annu. Rev. Nucl. Part. Sci.*, 54:315–59, 2004.

[25] G. Jungman, M. Kamionkowsi, and K. Griest. Supersymmetric dark matter. *Physics Reports*, 267, 1996.

[26] G. Bertone, editor. *Particle Dark Matter*. Cambridge University Press, 2010.

[27] G. Steigman, B. Dasgupta, and J. F. Beacom. Precise relic wimp abundance and its impact on searches for dark matter annihilation. *Phys. Rev. D*, 86(2), 2012.

[28] R N Mohapatra. Supersymmetry and r-parity: an overview. *Physica Scripta*, 90(8), 2015.

[29] J. D. Lewin and P. F. Smith. Review of mathematics, numerical factors, and corrections for dark matter experiments based on elastic nuclear recoil. *CLRC*, 1996.

[30] F. J. Kerr and D. Lynden-Bell. Review of galactic constants. *Mon. Not. Roy. Astron. Soc.*, 221:1023–1038, 1986.

[31] Fairbairn et al. Quantifying astrophysical uncertainties on dark matter direct detection results. *arXiv:1206.2693*, 2012.

[32] W. Dehnen and J. Binney. Local stellar kinematics from hipparcos data. *Mon. Not. Roy. Astron. Soc.*, 298:387–394, 1998.

[33] G. Gelmini and P. Gondolo. Wimp annual modulation with opposite phase in late-infall halo models. *Phys. Rev. D*, 64, 2001.

[34] R. W. Schnee. Introduction to dark matter experiments. *arXiv:1101.5205 [astro-ph.CO]*.

[35] O. Bienaymé et al. Weighing the local dark matter with rave red clump stars. *Astronomy & Astrophysics*, 571, 2014.

[36] L. Zhang et al. The gravitational potential near the sun from segue k-dwarf kinematics. *The Astrophysical Journal*, 772(2), 2013.

[37] H. Silverwood, S. Sivertsson, P. Steger, J. I. Read, and G. Bertone. A non-parametric method for measuring the local dark matter density. *arXiv:1507.08581 [astro-ph.GA]*, 2015.

[38] M. Pato, F. Iocco, and G. Bertone. Dynamical constraints on the dark matter distribution in the milky way. *Journal of Cosmology and Astroparticle Physics*, 2015, 2015.

[39] J. F. Navarro, C. S. Frenk, and S. D. M. White. The structure of cold dark matter halos. *Astrophysical Journal*, 462:563, 1996.

[40] D. Merritt et al. Empirical models for dark matter halos. i. nonparametric construction of density profiles and comparison with parametric models. *The Astronomical Journal*, 132(6), 2006.

[41] J. Bovy and S. Tremaine. On the local dark matter density. *The Astrophysical Journal*, 756(1), 2012.

[42] J. Engel. Nuclear form factors for the scattering of weakly interacting massive particles. *Phys. Rev. B*, 264(1,2), 1991.

[43] R. H. Helm. Inelastic and elastic scattering of 187-mev electrons from selected even-even nuclei. *Phys. Rev.*, 104(1466), 1956.

[44] G. Duda, A. Kemper, and P. Gondolo. Model-independent form factors for spin-independent neutralino–nucleon scattering from elastic electron scattering data. *Journal of Cosmology and Astroparticle Physics*, 2007, 2007.

[45] T. M. Undagoitia and L. Rauch. Dark matter direct-detection experiments. *Journal of Physics G: Nuclear and Particle Physics*, 43(1), 2015.

[46] M. Klasen, M. Pohl, and G. Sigl. Indirect and direct search for dark matter. *arXiv:1507.03800 [hep-ph]*.

[47] DAMA Collaboratoin. The dama/libra apparatus. *Nuclear Instruments and Methods A*, 592(297), 2008.

[48] C. Savage, G. Gelmini, P. Gondolo, and K. Freese. Compatibility of dama/libra dark matter detection with other searches. *JCAP*, 0904(010), 2009.

[49] J. H. Davis. The past and future of light dark matter direct detection. *Int. J. Mod. Phys*, 30, 2015.

[50] CoGeNT Collaboration. Search for an annual modulation in three years of cogent dark matter detector data. *arXiv:1401.3295*.

[51] J. H. Davis, C. McCabe, and C. Boehm. Quantifying the evidence for dark matter in cogent data. *JCAP*, 1408(014), 2014.

[52] CRESST Collaboration. Results from the 730 kg days of the cresst-ii dark matter search. *Eur. Phys. J. C*, 72(1971), 2012.

[53] M. Kuzniak, M. G. Boulay, and T. Pollman. Surface roughness interpretation of 730 kg days cresst-ii results. *Astroparticle Physics*, 36(1):77–82, 2012.

[54] CDMS Collaboration. Search for weakly interacting massive particles with the first five-tower data from the cryogenic dark matter search at the soudan underground laboratory. *Phys. Rev. Lett.*, 102, 2009.

[55] CDMS-II Collaboration. Dark matter search results from the cdms ii experiment. *Science*, 327(1619), 2010.

[56] SuperCDMS Collaboration. Search for low-mass weakly interacting massive particles with supercdms. *Phys. Rev. Lett.*, 112, 2012.

[57] COUPP Collaboration. First dark matter search results from a 4-kg $cf_3i$ bubble chamber operated in a deep underground site. *Phys. Rev. D*, 86(052001), 2012.

[58] PICO Collaboration. Dark matter search results from the pico-2l $c_3f_8$ bubble chamber. *Phys. Rev. Lett.*, 114(23), 2015.

[59] S. Ahlen et al. The case for a directional dark matter detector and the status of current experimental efforts. *Int. J. Mod. Phys*, 25, 2010.

[60] P. Grothaus, M. Fairbairn, and J. Monroe. Directional dark matter detection beyond the neutrino bound. *Phys. Rev. D*, 90(055018), 2014.

[61] A. Lansiart, A. Seigneur, J. L. Moretti, and J. P. Morucci. Development research on a highly luminous condensed xenon scintillator. *Nuclear Instruments and Methods*, 135:47, 1976.

[62] D. S. Akerib et al. The large undergound xenon (lux) experiment. *arXiv:1211.3788v2 [physics.ins-det]*, 2012.

[63] E. Aprile et al. The xenon100 dark matter experiment. *Astroparticle Physics*, 35(9):573–590, 2012.

[64] D. S. Akerib et al. The large underground xenon (lux) experiment. *Nucl. Inst. & Meth. in Phys. Res. A*, 704:111 – 126, 2013.

[65] E. Aprile et al. First dark matter results from the xenon100 experiment. *Phys. Rev. Lett.*, 105:13 – 24, 2010.

[66] D. S. Akerib et al. First results from the lux dark matter experiment at the sanford underground research facility. *Phys. Rev. Lett.*, 112, 2014.

[67] E. Aprile et al. Dark matter results from 225 live days of xenon100 data. *arXiv:1207.5988 [astro-ph.CO]*, 2012.

[68] K. Abe et. al. Xmass detector. *Nuclear Instruments and Methods A*, 716, 2013.

[69] E. Aprile et al. The xenon1t dark matter search experiment. *Springer Proc. Phys.*, 148:93–96, 2013.

[70] LZ Collaboration. Lux-zeplin (lz) conceptual design report. *LBNL-190005, FERMILAB-TM-2621-AE-E-PPD*, 2015.

[71] M.O. McLinden E.W. Lemmon and D.G. Friend. "thermophysical properties of fluid systems". *NIST Chemical Webbook, NIST Standard Reference Database Number 69*.

[72] J.A. Nikkel, R. Hasty, W.H. Lippincott, and D.N. McKinsey. Scintillation of liquid neon from electronic and nuclear recoils. *Astroparticle Physics*, 29(3):161 – 166, 2008.

[73] B. Singh and J. A. Cameron. Nuclear data sheets for a = 39. *Nuclear Data Sheets*, 107:225–354, 2006.

[74] P. Benetti et al. Measurement of the specific activity of 39ar in natural argon. *Nuclear Instruments and Methods in Physics Research Section A: Accelerators, Spectrometers, Detectors and Associated Equipment*, 574(1):83 – 88, 2007.

[75] H.O. Back et al. Depleted argon from underground sources. *Proceedings of the 2nd International Conference on Technology and Instrumentation in Particle Physics*, 2012.

[76] E. Aprile, A. E. Bolotnikov, A. I. Bolozdynya, and T. Doke. *Noble Gas Detectors*. Wiley-vch, 2006.

[77] R. Mulliken. Potential curves of diatomic rare-gas molecules and their ions, with particular reference to xe2*. *Journal of Chemical Physics*, 52(10), 1970.

[78] S. Kubota, M. Hishida, and J. Raun. Evidence for a triplet state of the self-trapped exciton states in liquid argon, krypton and xenon. *J. Phys. C*, 11:2645, 1978.

[79] Akira Hitachi, Tan Takahashi, Nobutaka Funayama, Kimiaki Masuda, Jun Kikuchi, and Tadayoshi Doke. Effect of ionization density on the time dependence of luminescence from liquid argon and xenon. *Phys. Rev. B*, 27(9):5279–5285, 1983.

[80] T. Suemoto and H. Kanzaki. Time-resolved absorption spectroscopy of self-trapped excitons in condensed ne, ar, and kr. *J. Phys. Soc. Jpn*, 46:1554–1562, 1979.

[81] V. Chepel and H. Araújo. Liquid noble gas detectors for low energy particle physics. *Journal of Instrumentation*, 8, 2013.

[82] D. N. McKinsey et al. Radioactive decay of the metastable $he_2$ molecule in liquid helium. *Phys. Rev. A*, 59:200–204, 1999.

[83] A. Morozov, T. Heindl, R. Krücken, A. Ulrich, and J. Wieser. Conversion efficiencies of electron beam energy to vacuum ultraviolet light for ne, ar, kr, and xe excited with continuous electron beams. *Journal of Applied Physics*, 103(10):103301–103301–8, 2008.

[84] N. Thonnard and G. S. Hurst. Time-dependent study of vacuum-ultraviolet emission in argon. *Phys. Rev. A*, 5(3):1110 – 1121, 1972.

[85] T. Doke, K. Masuda, and E. Shibamura. Estimation of absolute photon yields in liquid argon and xenon for relativistic electrons. *Nuclear Instruments and Methods A*, 291:617 – 620, 1990.

[86] T. Doke et al. Absolute scintillation yields in liquid argon and xenon for various particles. *Japanese Journal of Applied Physics*, 41(3A):1538 – 1545, 2002.

[87] S. Kubota et al. Dynamical behaviour of free electrons in the recombination process in liquid argon, krypton, and xenon. *Phys. Rev. B*, 20(3486-3496), 1979.

[88] T. Alexander et al. Observation of the dependence of scintillation from nuclear recoils in liquid argon on drift field. *Phys. Rev. D*, 88, 2013.

[89] W.H. Lippincott et al. Scintillation time dependence and pulse shape discrimination in liquid argon. *Phys. Rev. C*, 78(3), 2008.

[90] P. Agnes et al. First results from the darkside-50 dark matter experiment at laboratori nazionali del gran sasso. *Phys. Rev. B*, 743:456 – 466, 2015.

[91] M.G. Boulay et al. Measurement of the scintillation time spectra and pulse-shape discrimination of low-energy and nuclear recoils in liquid argon with deap-1. *arXiv:0904.2930*, 2009.

[92] D. Gastler et al. Measurement of scintillation efficiency for nuclear recoils in liquid argon. *Phys. Rev. C*, 85, 2012.

[93] A. Gedanken et al. Electronic energy transfer phenomena in rare gases. *Journal of Chemical Physics*, 57(8):3456 – 3469, 1972.

[94] K. Mavrokoridis et al. Argon purification studies and a novel liquid argon re-circulation system. *Journal of Instrumentation*, 6, 2011.

[95] DEAP-3600 Collaboration. The deap-3600 dark matter experiment. *in preparation.*

[96] Hamamatsu Corporation. R5912 photomultiplier tube datasheet. *TPMH1235E01.*

[97] Hamamatsu Corporation. Hamamatsu r5912-hqe datasheet. 2012.

[98] Hamamatsu. *Photomultiplier Tubes - Basics and Applications 3a*, 2007.

[99] Radia - http://www.esrf.eu/accelerators/groups/insertiondevices/software/radia.

[100] P DeVore, D Escontrias, T Koblesky, CJ Lin, DW Liu, KB Luk, J Ngan, JC Peng, C Polly, J Roloff, et al. Light-weight flexible magnetic shields for large-aperture photomultiplier tubes. *Nuclear Instruments and Methods A*, 737:222 – 228, 2014.

[101] M. Bodmer et al. Design of an active magnetic field compensation system for mini-clean. *Nuclear Instruments and Methods A*, 697:99 – 106, 2013.

[102] M. Bodmer, N. Phan, M. Gold, D. Loomba, J.A.J. Matthews, and K. Rielage. Measurement of optical attenuation in acrylic light guides for a dark matter detector. *Journal of Instrumentation*, 9, 2014.

[103] V.M. Gehman, S.R. Seibert, K. Rielage, A. Hime, Y. Sun, D.-M. Mei, J. Maassen, and D. Moore. Fluorescence efficiency and visible re-emission spectrum of

tetraphenyl butadiene films at extreme ultraviolet wavelengths. *Nuclear Instruments and Methods in Physics*, 654(1):116–121, October 2011.

[104] B. Broerman. Master's thesis, title tpd. Master's thesis, Queen's University, 2015.

[105] SNOLAB. *SNOLAB User's Handbook*, 2 edition, June 2006.

[106] *Neutron News, Vol. 3, No. 3, 1992, pp. 29-37.*

[107] B. Cai, M. Boulay, M. Kuzniak, and P. Skensved. Neutron backgrounds in deap-3600. Technical report, Queen's Univesity, 2011.

[108] R. Heaton et al. Neutron production from thick-target ($\alpha$,n) reactions. *Nuclear Instruments and Methods A*, 276, 1989.

[109] C. Nantais. Radiopurity measurement of acrylic for the deap-3600 dark matter experiment. Master's thesis, Queen's University, 2014.

[110] B. Cai, E. Devoie, C. Jillings, and M. Kuzniak. Deap-3600 av surface backgrounds from radon exposure. Technical report, Queen's Univesity, 2014.

[111] B. Beltran, J. Bueno, A. Hallin, and C. Mielnichuk. Background events from the deap-3600 neck components and tpb: a short note. Technical report, DEAP-3600, 2014.

[112] A. Hime. The miniclean dark matter experiment. In *Particles and fields. Proceedings, Meeting of the Division of the American Physical Society, DPF 2011, Providence, USA, August 9-13, 2011*, 2011.

[113] DEAP-3600 Collaboration. Deap-3600 dark matter search. *Nuclear Physics B Proceedings Supplement 00*, pages 1–7, 2015.

[114] T. Caldwell. Simulation of noble liquid detectors using rat,. *presented at AARM Meeting, Fermilab March 19-22*, 2014.

[115] S. Agostinelli et al. Geant4 - a simulation toolkit. *Nuclear Instruments and Methods A*, 506:250–303, 2003.

[116] R. Brun and F. Rademakers. Root - an object oriented data analysis framework. *Nucl. Inst. & Meth. in Phys. Res. A*, 389:81–86, 1997.

[117] T. Bolton. The braidwood reactor antineutrino experiment. *Nuclear Physics B*, 149(166-169), 2005.

[118] A. C. Sinnock and B. L. Smith. Refractive indices of the condensed inert gases. *Phys. Rev.*, 181(3), 1969.

[119] T Caldwell, S Seibert, and S Jaditz. Characterization of the r5912-02 mod photomultiplier tube at cryogenic temperatures. *Journal of Instrumentation*, 8(09):C09004, 2013.

[120] J. R. Prescott. A statistical model for photomultiplier single-electron statistics. *Nuclear Instruments and Methods*, 39:173–179, 1966.

[121] F. Kaether and C. Langbrandtner. Transit time and charge correlations of single photoelectron events in r7081 photomultiplier tubes. *Journal of Instrumentation*, 7, 2012.

[122] B.K. Lubsandorzhiev, P.G. Pokhil, R.V. Vasiljev, and A.G. Wright. Studies of prepulses and late pulses in the 8 electron tubes series of photomultipliers. *Nuclear Instruments and Methods A*, 2000.

[123] M. Akashi-Ronquest et al. Improving photoelectron counting and particle identification in scintillation detectors with bayesian techniques. *Astroparticle Physics*, 65(0):40–54, 5 2015.

[124] M. Ishida et al. Attenuation length measurements of scintillation light in liquid rare gases and their mixtures using an improved reflection suppresser. *Nucl. Inst. & Meth. in Phys. Res. A*, 516:462–474, 2004.

[125] G. M. Seidel, R.E. Lanou, and W. Yao. Rayleigh scattering in rare-gas liquids. *Nucl. Inst. & Meth. in Phys. Res. A*, 489(189-194), 2002.

[126] S.R. Seibert. Shellfit: Self-tuning position & energy reconstruction. Technical report, University of Pennsylvania, 2008.

[127] Plp-10 375 nm picosecond light pulser https://www.hamamatsu.com/jp/en/product/category/1001/5003/plp-10-038/index.html, September 2015.

[128] Plp-10 405 nm picosecond light pulser https://www.hamamatsu.com/jp/en/product/category/1001/5003/plp-10-040/index.html, September 2015.

[129] Plp-10 445 nm picosecond light pulser https://www.hamamatsu.com/jp/en/product/category/1001/5003/plp-10-044/index.html, September 2015.

[130] B. Moffat. *The Optical Calibration of the Sudbury Neutrino Observatory.* PhD thesis, Queen's University, 2001.

[131] K. J. Ma et al. Time and amplitude of afterpulse measured with a large size photomultiplier tube. *Nuclear Instruments and Methods A*, 629:93–100, 2011.

[132] K. Lung et al. Characterization of the hamamatsu r11410-10 3-inch photomultiplier tube for liquid xenon dark matter direct detection experiments. *Nuclear Instruments and Methods A*, 696:32039, 2012.

[133] J. Billard, F. Mayet, and D. Santos. Exclusion limits from data of directional dark matter detectors. *Phys. Rev.*, D82, 2010.

[134] S. Henderson and J. Monroe. The maximum patch method for directional dark matter detection. *arXiv:0801.1624v2*, 2008.

[135] S. Yellin. Finding an upper limit in the presence of an unknown background. *Phys. Rev. D*, 2002.

[136] XENON100 Collaboration. Likelihood approach to the first dark matter results from xenon100. *Phys. Rev. D*, 84, 2011.

[137] G. Cowan et al. Asymptotic formulae for likelihood-based tests of new physics. *Eur.Phys.J.C*, 71, 2011.

[138] Martin C. Smith et al. The rave survey: Constraining the local galactic escape speed. *Mon.Not.Roy.Astron.Soc.*, 379, 2007.

[139] https://root.cern.ch/roofit. Roofit — root a data analysis framework. 2015.